UNIVERSITÀ DEGLI STUDI DI MILANO
FACOLTÀ DI SCIENZE MATEMATICHE, FISICHE E NATURALI
DOTTORATO DI RICERCA IN
FISICA, ASTROFISICA E FISICA APPLICATA

UNDERSTANDING AND PREDICTING ION HEAT TRANSPORT IN TOKAMAKS

Settore Scientifico disciplinare FIS/03

Coordinatore: Prof. Marco Bersanelli
Tutore: Prof. Roberto Pozzoli
Co-tutore: Dr. Paola Mantica

Tesi di Dottorato di:
Benedetta Baiocchi
Ciclo XXIV

Anno Accademico 2010-2011

Contents

Summary

One of the most attractive options to satisfy the continuously growing world energy demand is thermonuclear fusion. This has the advantages of being CO2-free, having unlimited fuel availability, no radioactive waste, no risk of nuclear proliferation or hazard in case of accidents. The high temperature plasmas required to produce fusion reactions can be confined in suitable magnetic configurations, amongst which the most widely used is the tokamak. The recent decision to build the international tokamak ITER (International Thermonuclear Experimental Reactor) has significantly boosted the scientific and technological work for achieving controlled thermonuclear fusion. Amongst the physical problems still open, understanding and controlling heat transport is of primary importance for the optimization of the operational scenarios of ITER. Given the complexity of plasma transport processes, despite the significant progress made in the last two decades, a full theoretical understanding of the experimental observations and validated numerical models for the simulation of a complete tokamak discharge are not yet available. Work in this field is therefore actively ongoing, with a view to increasing integration between theoretical developments, experimental results and numerical predictions. This is the context in which the present thesis work takes place.

It has long been known that the high measured levels of heat transport in tokamaks, well above those due to collisions, are due to turbulent phenomena, in particular the so-called drift waves, driven by density and temperature gradients in presence of the quasi-neutrality constraint. This thesis is focused on the transport of ion heat, which is carried by ion temperature (T_i) and electrostatic potential fluctuations in suitable phase relation to yield an ion heat flux from centre to edge. These modes are known as ion temperature gradient (ITG) modes because they are destabilized when a threshold value of the inverse ion temperature gradient length ($1/L_{Ti}=|\nabla T_i/T_i|$) is exceeded. Above threshold, the ion heat flux is a strongly increasing function of $1/L_{Ti}$, which prevents the T_i profiles from departing significantly from threshold, a property known as profile stiffness. The main target of ion heat transport studies is to find ways to suppress or mitigate ITG modes, namely by increasing the threshold or reducing the stiffness level, in order to be able to achieve high core T_i values without having to rely on too high edge T_i values, which would raise plasma-wall interaction issues.

On the JET tokamak, which is equipped with high resolution ion diagnostics (Active Charge Exchange Spectroscopy) and flexible and localized Ion Cyclotron Resonance Heating (ICRH), sophisticated ion heat transport experiments have recently indicated that a strong reduction of ion stiffness takes place in presence of low magnetic shear and high toroidal rotation. This mechanism has been proposed as the key ingredient to explain the

improved core ion confinement observed in Hybrid scenarios or Advanced Tokamak (AT) scenarios with Internal Transport Barriers, two regimes that are considered for ITER operations beyond the standard inductive H-mode regime.

This thesis work starts from the above mentioned JET results and from the already developed theoretical models and existing numerical codes, and includes four main items of work, with the purpose of integrating experimental analysis and theory-based numerical modelling of JET experiments, in order to reach predictive capabilities for the future tokamak FAST, a device proposed by the Italian Fusion Association as a possible ITER satellite. First, new experiments have been carried out in JET and analyzed in detail, in order to assess if the cause for ion stiffness reduction is the rotation value or the rotational shear. Second, a numerical study has been carried out in JET and ITER plasmas to quantify the impact of ion threshold and stiffness on global confinement and fusion power compared to the effect of edge T_i value. This work has the aim of evaluating if threshold and particularly stiffness are indeed two useful control tools for scenario performance optimization. Third, a prediction work for the foreseen scenarios of FAST has been carried out, using a mixture of first-principle models and experiment driven considerations. Fourth, linear gyro-kinetic simulations have been carried out to check the validity of simplified threshold formulae used in simulations in the high toroidal field (B_T) and high density FAST plasmas. In the following paragraphs the main results obtained for each of these four items are summarized and some conclusions presented.

The JET experiments carried out to decouple the impact of rotation value and rotational shear on ion stiffness were based on the use of enhanced toroidal field ripple to lower the rotation value whilst preserving the rotation gradient to a large extent. These data were also compared with already existing data with Neutral Beam Injection (NBI) in the opposite direction to the plasma current, which yields high rotation values mainly due to edge rotation, with low core rotation gradients. The data analysis has given as result that it is the rotational shear and not the rotation value the key factor for ion stiffness mitigation. From the analysis of discharges with hollow rotation profiles, it was also found out that the sign of the rotation gradient does not matter for stiffness mitigation. These results give the indication for ITER that the necessary condition for reducing the ion stiffness and access improved core confinement regimes is to induce some rotational shear, which may be easier than achieving high absolute values of rotation.

Series of scans of ion stiffness and threshold and T_i pedestal height have been made in chosen JET and ITER plasmas using the Critical Gradient Model (CGM) in the 1.5D JETTO transport code. CGM is a semi-empirical transport model in which the threshold and stiffness level are assigned as explicit coefficients in the heat diffusivity expression. The variation of global confinement has been found quantitatively significant for changes of the ion stiffness (up to 30%), and comparable with the ones due to changes of ion

threshold and T_i pedestal height, when they are varied in an experimentally realistic range. In ITER, the calculated fusion power, which is what really matters for a fusion device, is as much affected by variations of ion stiffness as by changes of ion threshold and T_i pedestal height. This work gives the indication that all the three investigated parameters influence comparably the core performances in present and future machines. In particular the quantitative level of ion stiffness, which is a parameter not much considered until now, and assumed or predicted very high in most existing models, can be a useful knob to act upon in order to optimize the scenario performance and must be taken into account for an accurate predictive modelling of future machines.

The results obtained in the two previous steps have led to the conviction that predictive modelling of future devices cannot neglect including toroidal rotation profiles and their effects on transport, which is not common practice in tokamak simulation work. Developing such approach for the FAST simulations is also useful in view of ITER, in which the plasma rotation is expected to be much slower than presently operating devices, thereby raising questions on the validity of extrapolations that do not take into account the differences in rotation. Being a rather new type of exercise, the numerical tools available are not yet adequate. Models of momentum transport including the recently discovered inward convection and residual stress terms, which lead to intrinsic rotation in absence of external torque sources, are still being developed. In addition, the newly discovered effect of rotation and magnetic shear on ion stiffness is not contained in routinely available models. To avoid missing such important effects, a mixture of first principle models, when adequate, and empirical models tuned on the recent experimental results has been used. Both H-modes and fully non-inductive AT scenarios have been simulated, predicting profiles of current, ion and electron temperature, density and toroidal rotation (the poloidal rotation is assumed neoclassical). Various heating options have been explored, i.e. ICRH, ECRH, Lower Hybrid and Negative NBI. The latter provides a source of torque in addition to the intrinsic rotation, which is anyway expected rather sizeable, since inward momentum convection is predicted significant and edge rotation is also large if extrapolated from observations in the high magnetic field H-mode plasmas of the C-Mod tokamak. The simulations have provided a set of FAST scenarios in which fast particle and burning plasma studies can be performed, reaching values of thermal and fast particle energy contents well in line with the needs for exciting meso-scale fluctuations with the same characteristics of those expected in reactor relevant conditions.

The gyro-kinetic code GKW (Gyro-kinetics at Warwick) has been used in linear mode to calculate the ITG growth rates as a function of $1/L_{Ti}$ for typical FAST plasmas and extrapolate to the ITG threshold value at zero growth rate. This work was done to assess the validity in the FAST range of parameters of the simplified analytical formulae for the ITG threshold used for the FAST simulations. GKW was run both with adiabatic and kinetic electrons. Very good agreement was found between the analytical threshold approximation and the GKW simulations with adiabatic electrons, whilst the threshold

with kinetic electrons is slightly lower. The discrepancy is anyway small enough to justify the use of the threshold analytic approximation for FAST simulations, taking into account the other sources of uncertainty linked to various other modelling approximations and to empirical extrapolations from experimental data of existing machines.

Chapter 1

Introduction

The continuous growth of the energy global demand is one of the most important unsolved issues of our civilization. Today's energy consumption relies mainly on fossil fuels. However their availability is limited and they have the bad effect of producing CO2 and dusts thus polluting the environment and impacting on climate. Nuclear fission is CO2-free, but uranium availability is also limited and the long debated problems of radioactive waste, proliferations and risk of runaway are major disadvantages. Renewable energies need to be used at best, however it is unlikely that they can satisfy the world energy demand. The best alternative is nuclear fusion, which is CO2-free, intrinsically safe, does not produce radioactive waste, has no risk of proliferation and has unlimited fuel supplies. This motivates the present worldwide effort to achieve controlled thermonuclear fusion power production.

1.1 Thermonuclear fusion

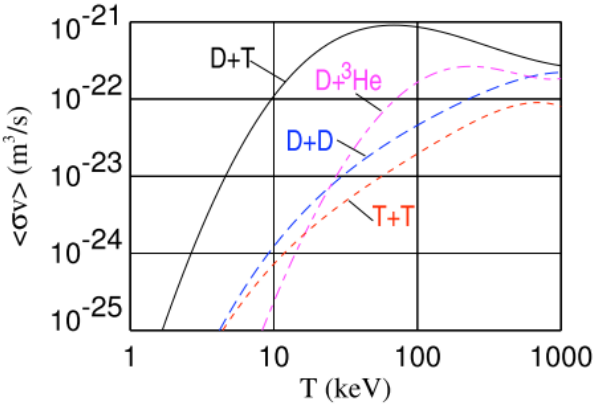

Fig. 1.1. Reaction rate as a function of the temperature for several fusion reactions.

Thermonuclear fusion reactions are the processes that naturally feed the stars, which are mainly formed by high temperature plasmas, confined by the enormous gravity force and in which all the particles are characterized by thermal agitation motions. Under these conditions fusion reactions between light nuclei take place. The sum of the rest masses of the reaction products turns out to be less than the sum of rest masses of the reagents, so an energy proportional to mass difference is released in accordance with the mass-energy equivalence principle. For example in the sun, that has an internal temperature of 10-15

millions of degrees, a fusion reaction chain that converts hydrogen nuclei into helium nuclei occurs. It is responsible for large part of the energy that comes to us as heat and light. It is a very slow process, and this is the reason why the sun has been shining for billions of years.

The fusion reactions that take place in the stars have too long characteristic times and release too low power density to be used as mechanism for producing energy on Earth. It is then necessary to consider the fusion reaction between different kinds of light nuclei. An important parameter that influences the choice is the reaction rate. In figure 1.1 it is shown as a function of temperature for different reactions. It reaches the maximum value for the fusion reaction between two hydrogen isotopes, deuterium (D) and tritium (T). This reaction rate starts to be relevant at temperature of about 10 keV or more (where 1 eV corresponds to about 10^4 degrees). The D-T reaction gives as products one alpha particle and one neutron:

$$D + T \rightarrow \alpha(3.5\text{MeV}) + n(14.1\text{ MeV}) \quad (1.1)$$

As element of comparison the reactivity of the nuclear reactions in the stars is 3 10^{-25} times lower than the reactivity of the D+T reaction.

To obtain the controlled thermonuclear fusion with a high positive energy balance in laboratory a D-T plasma has to be produced and heated up to very high temperature values (100 millions of degrees, more than six times the internal temperature of the sun). In order that the fusion reaction released energy is able at least to compensate the losses and the energy used to produce the plasma it is also necessary to maintain the plasma confined in a limited space for sufficient time and at high enough density. The Lawson criterion [1] identifies the product of the density and the energy confinement time as a critical parameter for a thermonuclear reactor. When the heating of the plasma by the products of fusion reactions is sufficient to maintain the temperature of the plasma against all losses without external power input the condition of ignition is reached. It corresponds to fulfill a requirement that involves three characteristic plasma parameters: temperature, density and energy confinement time. Considering negligible the losses caused by the bremsstrahlung radiation, it can be expressed in the following form for the "triple product" of the plasma variables:

$$n_e T \tau_E \geq \frac{12}{\mathcal{E}_\alpha} \frac{T^2}{\langle \sigma v \rangle} \quad (1.2)$$

where n_e is the electron density (expressed in m^{-3}), T is the temperature (expressed in keV) and τ_e is the energy confinement time of the plasma (expressed in s). $\mathcal{E}_\alpha$ (expressed in keV) is the energy of the α particles produced by the fusion reactions. The neutrons in fact escape the plasma and do not contribute to heating it. $<\sigma v>$ is the reaction rate (expressed in m^3/s). σ is the fusion cross section, v the relative velocity of the reagents and $<>$ denotes an average over the Maxwellian velocity distribution at the temperature T. For a D-T plasma in the temperature range of 10-20 keV the reaction rate can be written as

$$< \sigma v >= 1.1\, 10^{-24}\, T^2 \quad m^3/s, \quad (1.3)$$

where the temperature is expressed in keV. Using $\mathcal{E}_\alpha$=3.5 MeV the ignition condition becomes

$$n_e T\tau_E \geq 10^{21}\,\mathrm{keV\,s/m^3}. \quad (1.4)$$

The precise value of the constant in the formula (1.4) depends on the density and temperature profiles and if peak or average values are considered. The condition (1.4) holds for flat profiles.

In the stars the plasma tendency to diffuse away is balanced by the gravitational force due to their huge mass. The gravitational confinement is not feasible on Earth, then two alternative approaches are followed. The inertial confinement uses the inertia (mass) of the plasma particles. The confinement time is in fact determined by the time taken by the particles to go through the plasma volume where reactions occur. Little spheres formed by a high density (10^{25} m^{-3}) D-T blend are carried to fusion conditions by uniformly bombarding them through laser-produced x rays or high energy particles beams. The condition on the triple product for inertial confinement is fulfilled by reaching very high plasma densities (up to 10^3 times the solids density), however for short confinement times (of the order of ns).

The second method is magnetic confinement: it uses the electric charge of the particles, that, in presence of a magnetic field, are characterized by a motion bound to the magnetic field lines. In this approach several different configurations of magnetic fields have been developed in order to confine low density plasmas (10^{20} m^{-3}) for confinement times in the order of 1 sec. Magnetic field lines enveloped helicoidally on nested toroidal surfaces are demonstrated to confine charged particles. This magnetic field structure characterizes the most widely used thermonuclear fusion device, the so-called tokamak. In figure 1.2 the triple product values that have been achieved in tokamak machines during the years are shown.

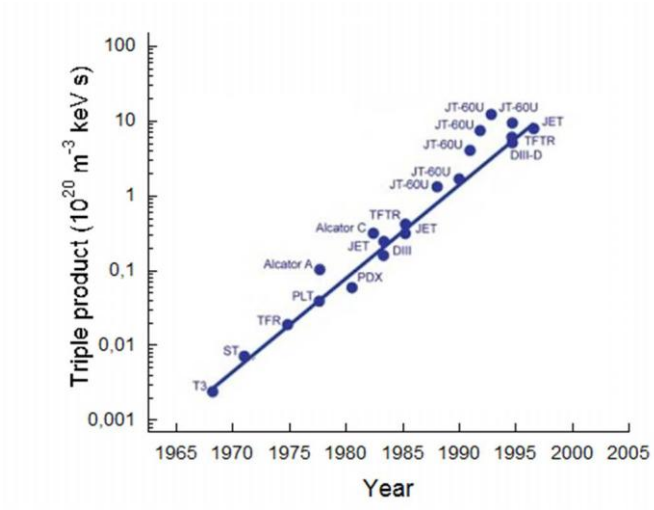

Fig. 1.2. Triple product values reached in several tokamak machines during the years [2].

1.2 Tokamaks

The tokamak device was developed in Russia in the 1950-60s and owes its name to the Russian acronym "TOroidalnaya KAmera MAgnitnymi Katushkami" standing for toroidal chamber with magnetic coils.

As shown in figure 1.3, the tokamak device is characterized by an axi-symmetric configuration with the toroidal magnetic field B_ϕ produced by external coils and the poloidal magnetic field B_θ generated by the toroidal current I_P which flows in the plasma and provides at the same time a source of heating and the magnetic confinement through the $\mathbf{J}x\mathbf{B}$ radial force. This current is induced by the magnetic flux variation in the central part of the torus produced by the primary circuit of a transformer of which the plasma ring is the secondary circuit. The pulse length is limited by the capacity of the primary circuit to induce the plasma current I_P that generates the poloidal field. Inductive current drive is the simplest way to drive the plasma current, but inherently limits the tokamak to pulsed operation, since the current in central solenoid cannot keep increasing indefinitely. The use of additional non-inductive methods of current drive can extend the pulse length, and in some cases enable the tokamak to achieve a steady state.

In order to obtain the equilibrium of the plasma ring a small vertical magnetic field B_V must be produced. It gives rise to a radial force toward the internal part of the torus and then hinders the plasma ring tendency to expand.

The presence of a toroidal and a poloidal component of the magnetic field leads to helical magnetic field lines that generate nested magnetic surfaces. On a magnetic surface the field lines wind around the torus, with the normalized pitch given by

$$q = \frac{rB_\phi}{RB_\theta} \tag{1.5}$$

where r is the distance to the plasma centre in the poloidal plane and R is the major radius of the torus. It indicates the number of toroidal turns followed by the magnetic field line when completing one poloidal turn. Its derivative with respect to the minor radius is known as the magnetic shear $s = \frac{r}{q}\frac{dq}{dr}$. Small magnetic field perturbations, resonant with rational values of q, lead to changes in the topology of the magnetic field, giving rise to a mix of good surfaces, chains of magnetic islands and regions of chaotic field. In general configurations with high values of q tend to be more stable. Because of this connection with the plasma stability, q is often called "safety factor".

The most restrictive stability condition (Kruskal-Shafranov [3]) gives a requirement for q which can be written in terms of the values that q achieves at the plasma edge (r=a, where a is the minor radius):

$$q(a) = \frac{B_\phi a}{B_\theta(a)R_0} > q_c, \tag{1.6}$$

where q_c is a constant between 2 and 3 and R_0 is the major radius. In a tokamak this condition is very important because it limits the values that the plasma current can reach.

The poloidal field evaluated in r=a can be expressed as a function of the plasma current as $B_\theta(a)=\mu_0 I_P/2\pi a$ and the condition (1.6) becomes

$$I_P < I_M \tag{1.7}$$

where I_M is proportional to B_ϕ. This limitation prevents the achievement of the fusion relevant temperatures if the only heating mechanism is the Ohmic one. In fact the resistivity of the plasma is a decreasing function of the temperature, and the Ohmic power is proportional to the product between resistivity and current. If the current has a maximum which doesn't depend on the temperature, for hotter plasmas the maximum ohmic power which can be dissipated in the plasma is lower because it scales with the resistivity, which decreases with growing temperature. For this reason a tokamak needs external heating methods in order to heat sufficiently the plasma. They are the injection of high energy neutral beams in the plasma (NBI heating), that are ionized by charge exchange and transfer their energy and momentum via collisions, or the injection of electromagnetic waves (RF heating), that are absorbed by the plasma through wave-particle resonance mechanisms.

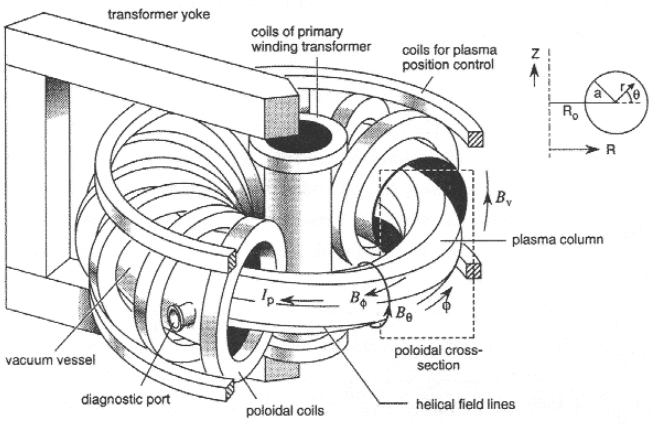

Fig. 1.3. Schematic picture of a tokamak.

1.3 Transport in Tokamaks

The ignition condition not only demands high temperature values but also imposes the condition of a good energy confinement time. One of the main problems in nuclear fusion research is that the experimental values for the energy confinement time are unexpectedly low if compared with the theoretical expectations. Several types of processes that force the plasma particles and energy to move in the radial direction, transversally to the magnetic field lines, and that cause particle and energy losses have been proposed by theory.

1.3.1 Classical transport

The classical theory [4] describes the transport phenomena in plasmas as due to Coulomb collisions of the particles. It holds in cylindrical geometries, where the magnetic field is uniform and time-independent. In the limits of validity of the two fluids treatment of the plasma the moment equations are the following:

$$\frac{\partial n_\alpha}{\partial t} + \nabla \cdot (n_\alpha \mathbf{V}_\alpha) = 0; \tag{1.8}$$

$$n_\alpha m_\alpha \left[\frac{\partial \mathbf{V}_\alpha}{\partial t} + \mathbf{V}_\alpha \cdot \nabla \mathbf{V}_\alpha\right] = -\nabla(n_\alpha T_\alpha) - \nabla \cdot \boldsymbol{\Pi}_\alpha + q_\alpha n_\alpha \left(\mathbf{E} + \frac{1}{c}\mathbf{V}_\alpha \times \mathbf{B}\right) + \mathbf{R}_\alpha; \tag{1.9}$$

$$\frac{3}{2} n_\alpha \left[\frac{\partial T_\alpha}{\partial t} + \mathbf{V}_\alpha \cdot \nabla T_\alpha\right] = -\nabla \cdot \mathbf{q}_\alpha - n_\alpha T_\alpha \nabla \cdot \mathbf{V}_\alpha - \boldsymbol{\Pi}_\alpha : (\nabla \mathbf{V}_\alpha) + Q_\alpha, \tag{1.10}$$

where n_α is the density, $\mathbf{V}_\alpha$ the velocity, p_α the pressure, q_α the charge, T_α the temperature of the species α of the plasma. **E** and **B** are the electric and magnetic fields. $\mathbf{q}_\alpha$ is the heat flux, $\mathbf{R}_\alpha$ is the collisional term in the momentum equation (1.9). Q_α is the heat generated in the α particles gas by collisions with particles of different species. Finally $\boldsymbol{\Pi}_\alpha$ is the stress tensor of the species α.

The system of equations (formed by the transport equations together with the Maxwell equations) is not closed, and, in order to give a complete description, it is necessary to express the quantities $\boldsymbol{\Pi}_\alpha$, $\mathbf{q}_\alpha$, $\mathbf{R}_\alpha$ and Q_α as functions of the physical plasma parameters n_α, T_α and $\mathbf{V}_\alpha$.

The transport theory based on Coulomb collisions provides a closure for moment equations. It describes the behavior of a plasma close to equilibrium, predicting the plasma response to the so-called thermodynamic forces, which characterize small departures from equilibrium. Assuming these forces to be sufficiently weak the plasma responds through a corresponding set of flows Γ_i that are related to the thermodynamic forces A_j by the following relation

$$\Gamma_i = -\sum_j L_{ij} A_j, \tag{1.11}$$

where the quantities L_{ij} are called transport coefficients. The entire set L_{ij} is called the transport matrix. Following the transport closure the moments $\boldsymbol{\Pi}_\alpha$, $\mathbf{q}_\alpha$, $\mathbf{R}_\alpha$ and Q_α are identified as fluxes, and transport equations in which the forces A_i are expressed in terms of the variables n_α, T_α and $\mathbf{V}_\alpha$ are derived. These relations are obtained by resorting to kinetic methods (for example using the Chapman-Enskog theory [5]) or through phenomenological estimates.

In the direction perpendicular to the magnetic field a heuristic estimate of the classical particle diffusion can be given by the random walk model. Without collisions a particle would move around a magnetic field line describing circular orbits characterized by the Larmor radius $\rho_L = m_\alpha v_\perp / (q_\alpha B)$, where $v_\perp$ is the component of the particle velocity perpendicular to the magnetic field. However it collides with other particles, and collision and gyration interact to produce a random walk of the guiding center across the magnetic field: the particle jumps to a neighboring magnetic field line with a step length equal to

the Larmor radius and a step frequency given by the collisional rate ν. Like particles collisions do not lead to net particle diffusion, so electron and ion diffusion rates are both determined by electron-ion collisions (ν is then the electron-ion collision rate). Furthermore the velocity distribution function of the plasma particles is assumed close to local thermodynamic equilibrium. The transversal diffusion coefficient is then $D_c \sim \rho_{Le}^2 \nu$, both for ions and electrons. Different collisional rates characterize ions and electrons and in particular electrons diffuse faster than ions. The formed charge imbalance gives rise to an electric field which tends to decelerate electrons and accelerate ions, leading to equal diffusion fluxes of the particles species. We have then an ambipolar diffusion, and the electrons, that are the component with the smallest diffusion coefficient, determine the resulting flux.

The heat and momentum diffusivities can be predicted by the random walk model too. The electron thermal diffusivity is found comparable to the particle diffusion coefficient $\chi_{ec} \sim D_c$, while the ion thermal diffusivity and the momentum diffusivity are larger by the square root of the mass ratio $\chi_{ic} = \chi_{Mc} \sim (m_i/m_e)^{1/2}\chi_{ec}$. However the classical description is far from explaining the transport processes in tokamaks. It neglects the impact of the toroidal geometry proper to these devices, that provides curve magnetic field lines, causing a transport enhancement.

1.3.2 Neo-classical transport

The theory that describes the transport as driven purely by Coulomb collision but taking into account the toroidal effects is called neo-classical [6]. In a torus particles are subject to magnetic field inhomogeneity and curvature drifts that cause the particles with a low collision frequency to become trapped in the so-called "banana" orbits. Particles with a sufficiently large ratio between the velocities perpendicular and parallel to the magnetic field bounce between the points of high magnetic field.

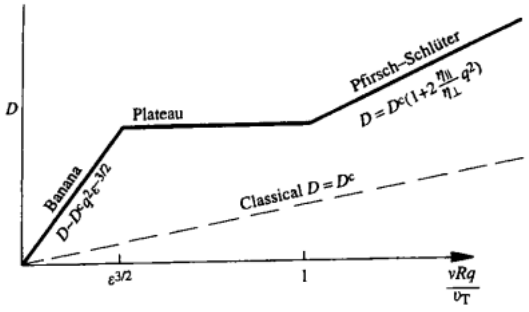

Fig. 1.4. Diffusion coefficient as a function of the normalized collision frequency [7].

According to the collisionality level three regimes are determined, as shown in fig. 1.4. The banana regime is characterized by low collisionality. The transport that arises from the small population of trapped particles dominates on the transport resulting from the majority of the passing particles. The diffusion coefficient increases starting from zero.

The plateau regime is characterized by a diffusion coefficient almost independent on the collisionality. In the Pfirsch-Schluter regime, that takes place for higher collision rates, the diffusion coefficient again increases with the collisionality.

The transport increase can be explained using the random walk model. Because of the drifts due to the toroidal geometry, trapped particles drift off the flux surfaces with a radial excursion larger than the Larmor radius, increasing the collisional step size. With respect to the classical diffusion coefficients and for large aspect ratio approximation ($\varepsilon := r/R << 1$) the neoclassical ones are given by:

$$D_{ncb} = D_c q^2 \varepsilon^{-3/2} \tag{1.12}$$

for the banana regime, where q is the safety factor,

$$D_{ncPS} = D_c(1 + 2\eta_{\parallel}/\eta_{\perp} q^2) \tag{1.13}$$

for the Pfirsch-Schluter regime, where $\eta_{||}$ and $\eta_{\perp}$ are the resistivities respectively parallel and perpendicular to the magnetic field and

$$D_{ncp} = D_c q \frac{v_{the}}{R\nu} \tag{1.14}$$

for the plateau regime, where v_{the} is the electron thermal velocity. Similar estimates for the electron (χ_e) and ion (χ_i) heat diffusivities give $\chi_{enc} \sim \chi_{inc}(m_e/m_i)^{1/2} \sim D_{nc}$.

The neoclassical diffusion coefficient reaches values 10-100 times larger than the classical one. According to neo-classical theory for parameters typical of a tokamak plasma (T_e,T_i ~ 1 keV, B ~ 1 T, $n_e \sim 5\ 10^{19}$ m^{-3}) the diffusion coefficients are equal to

$$D_{nc} \sim \chi_{enc} \sim \chi_{inc} \sqrt{\frac{m_e}{m_i}} \sim 0.01\ m^2/s \tag{1.15}$$

The momentum diffusivity, of which the toroidal component is considered, does not show a neoclassical enhancement in the collisional regime. In the banana regime it can be estimated as $\chi_\phi \sim 0.1\rho_{Li}^2 q^2 \nu$.

Using the classical transport matrix representation (1.11) the neo-classical transport theory describes the transport in terms of the fluxes of the plasma parameters (particles, heat, momentum, charge) and their thermodynamic forces (gradient of density, temperature, velocity and electrostatic field), both averaged over a magnetic surface. The problem is then reduced to 1 dimension, and the fluxes depend only on the radial coordinate. In (1.16) the transport coefficients in form of a matrix of proportionality between fluxes and forces are presented.

$$\begin{pmatrix} \Gamma \\ q_e/n \\ q_i/n \\ \Pi_\phi/Rnm_i \\ j_{\parallel} \end{pmatrix} = \begin{pmatrix} D & L_{12} & L_{13} & L_{14} & W \\ L_{21} & \chi_e & L_{23} & L_{24} & L_{25} \\ L_{31} & L_{32} & \chi_i & L_{34} & L_{35} \\ L_{41} & L_{42} & L_{43} & \chi_\phi & L_{45} \\ B & L_{52} & L_{53} & L_{54} & \sigma \end{pmatrix} \begin{pmatrix} -\nabla n \\ -\nabla T_e \\ -\nabla T_i \\ -\nabla \Omega \\ -E_{\parallel} \end{pmatrix} \tag{1.16}$$

The diagonal elements of the matrix describe the diffusion processes: D is the particle diffusion coefficient (quasi-neutrality is assumed), χ_e and χ_i the electron and ion heat diffusion coefficients, χ_ϕ the toroidal momentum diffusion coefficient and σ is the

electrical conductivity. Ω is the toroidal rotation of the plasma and $j_{||}$ the current density parallel to the magnetic field. The off-diagonal components W and B are neo-classical phenomena that have a significant impact for the plasma dynamics, and have been confirmed experimentally.

W defines the Ware-pinch effect [8], an inward particle flux due to the effect of the toroidal electric field on the orbit of trapped particles. The electric field breaks the symmetry about the plasma mid-plane of the impact that the gradient and the curvature of the magnetic field have on the trapped particles, and this leads to a not null inward radial displacement per bounce period of the trapped particles.

B determines the bootstrap current [9], an electric current parallel to the magnetic field, driven by the radial pressure gradient through the pressure anisotropy it generates in an inhomogeneous magnetic field. The bootstrap current is carried by the passing particles and it is generated through collisional coupling of trapped and passing particles. This current can be thought of as an advantage, because it is automatically generated confining a high-pressure plasma and then it can, in principle, allow for a steady state tokamak reactor in which only a small fraction of the plasma current is driven through external means.

The other off-diagonal terms are difficult to access by experimental studies, however the neo-classical theory give expressions for all of them.

Experimentally the transport level cannot be lower than the neo-classical one, then the neo-classical prediction is the maximum attainable confinement of particles and energy.

1.3.3 Anomalous transport

Parallel transport is well described by the neo-classical theory: the experimental observations agree with the estimates for σ and B. However experiments don't confirm the estimates for cross-field diffusivities. In particular the ion heat diffusion coefficient exceeds neo-classical predictions up to one order of magnitude, and the electron diffusion coefficient by up to one or two orders of magnitude. Also the toroidal momentum diffusivity reaches values much larger than the neoclassical ones. Experiments give

$$\chi_i \sim \chi_e \sim \chi_\phi \sim (3-5)D \sim 1\ m^2/s \tag{1.17}$$

The most plausible explanation of the huge difference between the neo-classical estimates and the experimental results seems to be given by the collective nature of the plasma. The particles organize themselves as more or less coherent structures giving rise to collective modes, some of which may become unstable and lead to turbulent motions of the plasma. These turbulent processes influence significantly the mechanism of the transport. In many cases the turbulent contribution dominates the classical and neo-classical ones, and the transport is called anomalous.

The collective modes can be divided in two classes: the magneto-hydrodynamics (MHD) modes, that are characterized by macroscopic dimensions, comparable to the plasma

ones, and can be described by one fluid approach, and the drift waves, small scale phenomena in which electrons and ions must be described taking into account their disparate dynamics. MHD modes have to be maintained stable, because they cause macroscopic losses of plasma confinement. The plasma drift micro-instabilities don't lead to catastrophic events, as plasma disruptions, however they can give rise to enhanced particle and heat transport.

To understand these mechanisms of increased transport and to control them in order to reduce the anomalous transport is one of the aims of the present research studies. Some methods of turbulence quenching have been found, and improved confinement operational scenarios have been developed.

1.3.3.1 Transport and plasma scenarios

The most common operation modes at present are the L-mode scenario [10], the H-mode scenario [11], the hybrid scenario [12-14] and the steady state scenario [15].

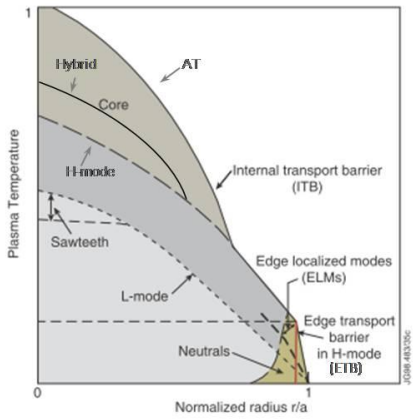

Fig. 1.5. Schematic view showing regions with different transport characteristics in different plasma scenarios. Adapted from ref. [16].

The different tokamak scenarios can be described starting from their transport properties. The figure 1.5 gives a schematic view of the plasma regions with different transport characteristics for the considered plasma scenarios.

Since in tokamaks the transport behaviour varies significantly across the plasma, the plasma volume can be subdivided in five regions with different transport characteristics.

In the edge the scrape-off-layer region (SOL) includes plasma outside the separatrix, the last closed magnetic surface. Fast longitudinal transport and atomic processes dominate this zone.

In the narrow region just inside the separatrix an edge transport barrier (ETB) can develop. It is a localized reduction of transport which give rise to very steep temperature and pressure profiles (the so-called temperature and pressure edge pedestals) in the region where it forms. It is absent in the L-mode, that is characterized by a relatively low energy confinement time. The ETB is present in the H-mode scenario. It is a higher

confinement mode which takes place as transition from the L-mode when the additional input power increases. The H-mode is a robust scenario, because it has been found in a large number of fusion machines with very different conditions. However a large fraction of the plasma current is driven inductively, so very long steady-state operation wouldn't be possible to achieve. For this reason and other drawbacks the H-mode scenario doesn't seem a feasible scenario in view of a fusion reactor machine. Like the H-mode the presence of an ETB characterizes the other operational regimes. The existence of an ETB implies a significantly reduced level of plasma micro-turbulence, and then strong pressure gradient (a pressure pedestal) and large bootstrap currents, that lead to repetitive MHD instabilities, the so-called edge localized modes (ELMs).

Another narrow region links the edge to the core region. Here the transport is dominated by ELMs, collisional turbulence and cold neutrals.

Deeper inside, the core region of the plasma is positioned: it is a wide zone, as far as possible free of any strong MHD instabilities. The drift type micro-turbulence dominates the transport in this region. Hybrids, that are characterized by a low fraction of inductive current, present improved confinement, due to a reduced transport. Two of the main ingredients that seem to cause it are the presence of toroidal rotation and a core q profile flatter than the H-mode one. Steady state scenarios, that are characterized by total non-inductive current, present an internal transport barrier (ITB), that causes a large improvement of the confinement and the developing of a large bootstrap current that helps non inductive operations. Several parameters are thought to play a role in the formation and dynamics of the ITB: a flat or reversed q profile, low order rational q surfaces, sheared plasma flow, the Shafranov shift of adjacent magnetic flux surfaces (a displacement of the magnetic axis and flux surfaces due to pressure and current density profiles with respect to the magnetic axis in the vacuum field) and thermal ion dilution in presence of a large fast population.

Finally the central region of the plasma is characterized by transport dominated by the MHD events called sawteeth if the core q profile reaches values higher than 1. They can trigger other dangerous instabilities as the neo-classical tearing modes (NTM), which lead to significant reduction in confinement and limit plasma performance. The condition $q>1$, for sawteeth development, is not fulfilled in the hybrid and steady state scenarios, so these regimes are regulated by reduced micro-turbulence and neo-classical transport also in the central region of the plasma.

1.3.3.2 Description of core anomalous transport

The core region of the plasma is dominated by the anomalous transport driven by micro-instabilities. In order to describe the modes that are responsible for the micro-turbulence a first classification can be done. In the electrostatic turbulence description transport is due to fluctuating electric fields, assuming non perturbed magnetic surfaces. The electric field generates a fluctuating radial velocity (**E**x**B**), which, if in unstable phase relation with fluctuations in density or pressure, carries particle and heat fluxes. The magnetic

turbulence picture focuses on fluctuations in the magnetic fields that can break the axial symmetry and destroy the set of the nested flux surfaces. It is remarked that both electric and magnetic components exist for any physical fluctuation. This classification is however useful because of the complexity of the anomalous transport problem, for which a comprehensive theory has not yet been developed.

Drift wave turbulence in tokamak plasmas is in fact a highly complex non-linear system, which involves multiple-scale turbulence modes and non-linear phenomena. Among the non-linear mechanisms, the zonal flows [17] are recognized to be an intrinsic and important constituent of the drift wave turbulence, having a central role in its self-regulation mechanism. Zonal flows are coherent structures due to low frequency, predominantly poloidally symmetric potential perturbations characterized by small radial scale. They are driven exclusively by non-linear energy transfer from drift waves, then they cannot be sustained in the absence of turbulence. Their generation leads to reduce the transport level and intensity caused by the primary drift wave turbulence, so zonal flows act to regulate and partially suppress drift wave turbulence and transport.

Turbulent transport models can in general predict a complicated relation between the different transport channels. The relations between fluxes and driving plasma quantities can be expressed as

$$\begin{pmatrix} \Gamma \\ q_e/n \\ q_i/n \\ \Pi_\phi/Rnm_i \end{pmatrix} = \begin{pmatrix} D & M_{12} & M_{13} & M_{14} \\ M_{21} & \chi_e & M_{23} & M_{24} \\ M_{31} & M_{32} & \chi_i & M_{34} \\ M_{41} & M_{42} & M_{43} & \chi_\phi \end{pmatrix} \begin{pmatrix} -\nabla n \\ -\nabla T_e \\ -\nabla T_i \\ -\nabla \Omega \end{pmatrix} + \begin{pmatrix} V_p & N_{12} & N_{13} & N_{14} \\ N_{21} & V_e & N_{23} & N_{24} \\ N_{31} & N_{32} & V_i & N_{34} \\ N_{41} & N_{42} & N_{43} & V_\phi \end{pmatrix} \begin{pmatrix} n \\ T_e \\ T_i \\ \Omega \end{pmatrix} \qquad (1.18)$$

This general representation includes a diffusion part (the first term on the right of (1.18)) in which diagonal and off-diagonal terms of proportionality between fluxes and gradients of plasma variables are included. Due to turbulence, they reach values much higher than the ones predicted by neo-classical theory. The convective part with diagonal (i.e. convective velocities) and off-diagonal terms is also included as second term in (1.18). Diagonal and off-diagonal coefficients of the matrixes are determined by different theoretical treatments based on the description of physical phenomena that are believed to be at the origin of the anomalous transport processes.

Several approaches have been developed in order to obtain an estimate of the diffusion coefficients. The mixing length estimate (it will be explained in the next Chapter) gives

$$D \sim \left(\frac{\gamma_L}{k_\perp^2}\right)_{k_{\perp max}}, \qquad (1.19)$$

where γ_L is the linear growth rate of the instability and $k_\perp$ is a characteristic perpendicular wave number of the turbulence. Equation (1.19) can be interpreted as balancing the diffusion due to the linear growth rate against the turbulent diffusion at saturation.

Using the random walk estimate for the diffusion coefficient of a test element of fluid we can express it as

$$D \sim \frac{L_c^2}{\tau_c}, \qquad (1.20)$$

where τ_c is the inverse correlation time and L_c is the correlation length. The turbulence is analyzed statistically, and an experimental estimate can be given measuring the statistically averaged correlation time and length through fluctuation diagnostics. The scaling of the turbulent transport can be determined starting from the expression (1.20). When turbulent fluctuations are caused by drift waves characterized by low frequency and spatial scale of the order of the ion or electron gyro-radius the transport coefficient is described by the gyro-Bohm scaling, as theoretically expected

$$D_{gB} \sim \frac{\varrho_{Li,e}}{a}\frac{T_{i,e}}{eB}, \tag{1.21}$$

where ρ_L is the Larmor radius. a, the minor radius, gives the typical macroscopic scale length of the plasma. If the turbulent fluctuations are characterized by a macroscopic scale, comparable with the size of the plasma, the scaling is of the Bohm type

$$D_B \sim \frac{T_{i,e}}{eB}. \tag{1.22}$$

Experiments have been performed and both behaviors have been found.

Experimentally the simplest method to determine diffusivity is the so-called particle/power balance analysis carried out in the plasma in quasi-steady state conditions. The two fluid equations (1.8)-(1.10) can be generally expressed by

$$\frac{\partial g}{\partial t} + \nabla \cdot \mathbf{F} = S \tag{1.23}$$

Where S is the source term, necessarily not null in order to have a steady state, g is the density of particles, momentum or ion or electron thermal energy, **F** is the corresponding flux. In the steady state an accurate calculation of the sources integrated over the volume inside a magnetic surface provides the flux across this surface. On the other hand a detailed measurement of the physical parameters profiles yields the values of the local gradients. Then the particle/power balance transport coefficients can be deduced by dividing the flux and the correspondent gradient, as reported in equations (1.17)-(1.19). For the ion heat case the relation is the following

$$\chi_i^{pb}(\varrho) = -\frac{q_i(\varrho)}{n(\varrho)\nabla T_i(\varrho)}. \tag{1.24}$$

Quantities depend on the radius, in fact this relation is assumed to hold locally. In addition, it yields an effective diffusivity in which off-diagonal and convective fluxes are embedded. This method is widely applied as starting point to any transport analysis. For a series of reasons (among which the existence of non negligible off-diagonals terms of the diffusion coefficients matrix, a possible non linear relation between fluxes and gradients, a possible non-local character of the transport) this picture of the transport results to be too simple and inadequate in certain cases.

A different approach for experimental studies has been developed and widely used. The perturbative transport analysis [18] consist in producing a small, well localized perturbation of plasma parameters gradients in a stationary plasma, and to follow the evolution in space and time of the effect of this perturbation. For example, for the case of the ion heat transport, the incremental ion heat transport coefficient, χ_{iinc} is given by

$$\chi_i^{inc}(\varrho) = -\frac{\partial q_i(\varrho)}{n(\varrho)\,\partial \nabla T_i(\varrho)}. \tag{1.25}$$

The difference between the χ_{iinc} and χ_{ipb} and its dependence on the perturbation frequency, that is shown in figure 1.6, allows to distinguish diffusive from convective or off-diagonals transport coefficients and to investigate non-linearities.

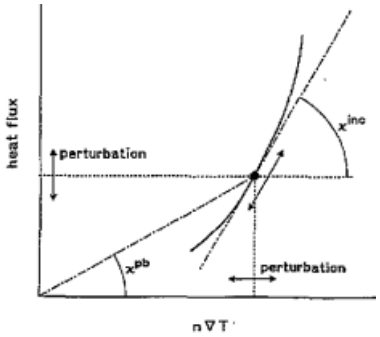

Fig. 1.6. Schematic illustration of the difference between χ_{pb} and χ_{inc} in the general case in which the relation between flux and conjugate gradient is non linear and with off-diagonals terms [18]. In general dynamic experiments yield transport coefficients that differ from those estimated , essentially because they measure the changes in the fluxes induced by variations of gradients rather than the total net flux and gradient.

Computational models of turbulent transport produce estimates of diffusion coefficients starting from the fundamental equations that describe the plasma and computing the turbulent fluctuations and consequent transport. Several transport models have been developed. The more complete approach is at the level of the kinetic description given by Vlasov or the Fokker-Planck equation, where functions of position velocity phase-space variables and time evolve. Averaging over the gyro-motion gives the gyro-kinetic description, in which finite gyro-radius effects are retained nonperturbatively. Drift-kinetic models ignore or treat perturbatively finite gyro-radius effects. In fluid models fluid variables, that are functions of position and time, are evolved. Gyro-fluid models, a special class of fluid models derived from gyro-kinetic equations, take into account finite gyro-radius effects non perturbatively.

Heat transport

Understanding heat transport in the core is very relevant for predicting the performances of a fusion device. Ion thermal transport influences the values that central ion temperatures and then the fusion power can achieve. The heat transport of electrons is equally relevant, because electrons are directly coupled to the power carried by α particles in a fusion reactor.

In the plasma core the heat transport is mainly anomalous. It is driven by micro-instabilities given by the inhomogeneity of the plasma, in particular by the existence of density and temperature gradients. The modes can be classified according to the specific non-uniformity in the plasma that drives them. Several categories have been found: modes due to ion temperature gradients, to electron temperature gradients, to density gradient and to pressure gradient. This last family of modes gives rise to fluid like instabilities, such as the current diffusive ballooning, drift resistive ballooning and neo-classical tearing modes. In low β plasmas (where β is the ratio between the kinetic and the magnetic pressure, $\beta=2\mu_0 p/B^2$) theory predicts that most of the heat transport in the core is carried by the electrostatic micro-instabilities driven by temperature and density gradients [19,20].

The modes driven by ion temperature gradient (ITG) are drift waves, characterized by the longest wavelength among temperature gradient driven modes [21-24]. They are believed to be the main responsible for the ion heat transport. However they have a non-negligible influence also on the electrons, as shown in figure 1.7, where a summary of drift waves characteristic scales, mechanisms and impact on transport is presented.

Electron temperature gradients can drive two different modes: electron temperature gradient (ETG) and trapped electron (TEM) modes. ETG have the shortest wavelength and can produce only electron heat flux. The typical spatial scale of TEM is intermediate between ITG and ETG. Trapped electron modes cause electron turbulent heat flux but can have effects also on the ion heat transport.

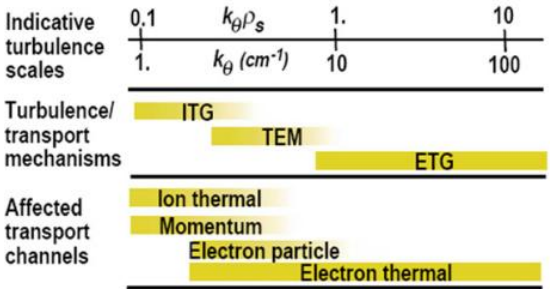

Fig. 1.7. Scheme of drift waves turbulence scales, transport mechanisms and affected transport channels [25].

Due to the very short wavelength ETG modes give only a small direct transport. However they can excite modes with longer wavelength through mode coupling. Normally ITG and TEM modes are considered in the heat transport analysis, while the effect of ETG is regarded as a residual transport level.

The theory predicts that temperature gradient modes become unstable when the relevant relative temperature gradient exceeds a critical value (a threshold value):

$$\frac{\nabla T_{i,e}}{T_{i,e}} > \left(\frac{\nabla T_{i,e}}{T_{i,e}}\right)_{cr} \tag{1.26}$$

Temperature gradient thresholds are functions of different plasma parameters. A typical stability diagram is presented in figure 1.8 for the case of $T_i=T_e$. For some values of temperature and density gradients more than one mode can be unstable. Treating ion and electron modes separately is an oversimplification, however these are experimental situations in which one branch is dominant.

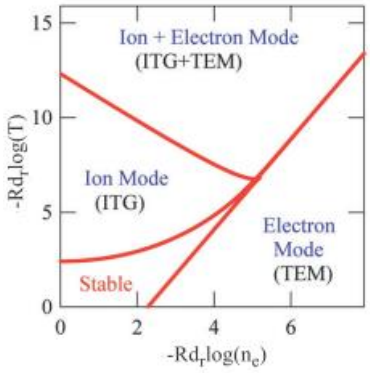

Fig. 1.8. Stability diagram of ITG/TEM modes. Ion and electron temperatures reach equal values [20].

For temperature gradients above the threshold values the induced heat transport becomes turbulent and grows strongly with increasing temperature gradient. As a consequence the T profiles peaking cannot be raised significantly above the threshold values: this property is called stiffness of T profiles. In particular we refer to a high level of stiffness when the heat flux growth implies a minimum variation of the relative temperature gradient, which keeps very close to the threshold value. On the contrary, if the increase of the heat flux leads to a significant growth of the relative temperature gradient, this trend is identified with a low level of stiffness.

The above described behaviour has been verified experimentally for electrons [26,27]: electron threshold and electron stiffness factor have been measured in perturbative experiments, and comparison with theory and parametric studies were widely carried out. Electron thresholds are found to be consistent with theory predictions of TEM, and electron stiffness levels are found to be of similar magnitude for different devices, with a trend to increase from lower values for plasmas with pure electron heating to higher values in the case of ion heating.

Recent experiments have led to the first comparison of theoretical predictions for threshold and stiffness also for ions [28-30]. Heat flux scans and modulation experiments have allowed to study separately the ion threshold and ion stiffness values and their parametric dependences. Ion threshold behavior follows theoretical expectations and is quantitatively in agreement with linear gyro-kinetic predictions. Non-linear gyro-kinetic simulations predict a generally high stiffness level for ions, and then ion temperature gradients near the threshold value. However, under some physical conditions, reduced ion stiffness, and ion temperature gradients higher than the threshold, has been experimentally found.

Particle transport

Particle and impurity transport studies are very important for a future reactor because they control the transport of the fuel into the core region and the fusion reactions ash away from it. However investigating and understanding particle and impurity transport is very challenging because of several conditions peculiar to their dynamics, as the existence of two kinds of dominant particle sources (in the centre and in the edge of the plasma) and the non-negligible presence of the convection in addition to diffusion.

Impurities transport is generally anomalous, faster than predicted by neo-classical theory. Transport of particles (ions and electrons) has been found mainly anomalous too. The scope of studying particle transport is mainly linked to achieve high densities in the core plasma, in order to obtain in a future reactor a large amount of fusion power, because it scales with the square of the density. High densities are reachable only with a centrally peaked density profile. In fact it allows to have peripheral density values below the Greenwald limit [31], an empirical density limit for the plasma edge above which a disruption can happen and cause the termination of the confined plasma. However, if the density profile is peaked, the central density can achieve higher values. In stationary conditions a moderately peaked electron density has been regularly found in tokamaks at low collisionality.

In steady state the particle flux can be expressed by

$$\Gamma = -D\nabla n + nV, \tag{1.27}$$

where Γ is the outer flux, D is the particle diffusion coefficient and V is the convective velocity. The two dominant particle sources that can contribute to the balance are the central fuelling due to neutral beam injection (NBI) and the edge fuelling by gas puffing, recycling and pellet injection.

The existence of an inward convection has been introduced to explain the sustainment of density gradients, and then a peaked density profile, that is observed also in absence of a central particle source. As described in paragraph 1.3.2 of this thesis, neo-classical transport theory predicts a particle pinch driven by the induced toroidal electric field, that causes an inward flow of trapped particles (Ware pinch). This neoclassical mechanism of pinch has been identified in some experiments [32], however in most conditions it has been found insufficient to justify the observed density gradients, because it gives a too small effect in order to predict the actual plasma diffusivity. This last quantity has been found to reach values of the order of the electron heat diffusivity [18], and then largely above the neoclassical predictions. The presence of a predominant anomalous component has been supposed.

Experimental and theoretical studies [33] have been carried out in order to understand the mechanisms at the basis of this enhanced particle transport and of peaked density profiles. From ITG/TEM quasi-linear theory the particle flux is given by

$$\Gamma = -D\nabla n - D_T n \frac{\nabla T_e}{T_e} + nV, \tag{1.28}$$

where the first term is the diagonal diffusion, the second is the off-diagonal so-called thermodiffusion and is proportional to the electron temperature gradient. Finally the third contribute is a pure convective term. The role of these mechanisms on the particle transport has been widely confirmed experimentally, also through perturbative investigations.

Momentum transport

Momentum transport studies are of interest because of the significant role of the plasma rotation in improving plasma confinement. Sheared rotation in fact leads to the quenching of turbulence, with consequent transport reduction and improvement of plasma performances, as it will be explained in Chapter 2 of this thesis. In addition the toroidal rotation improves the stability of dangerous MHD waves, as resistive wall modes and neo-classical tearing modes.

Theoretical studies about the anomalous transport driven by ITG predict very similar toroidal momentum diffusivity and ion heat diffusivity. The so-called Prandtl number, defined as the ratio between these two diffusivities, is then expected to be equal to 1 ($Pr:=\chi_\phi/\chi_i=1$) [21]. This was confirmed by early experiments in which a large external torque was applied to the plasma [34], and conclusions were that without external core momentum input the plasma rotation would be negligible.

When the existence of a finite rotation without any external torque (the so-called intrinsic rotation [35]) was discovered this picture didn't work anymore. In addition in several experiments the effective Prandtl number is found to reach values significantly smaller than 1 [36-38], so the existence of a momentum pinch has been supposed. A momentum pinch together with a residual stress (that is a flux component which doesn't depend on velocity and its gradient) are predicted by the theory [39]. The residual stress is directly observed experimentally and it is found to be dominantly located at the plasma edge, in agreement with theory predictions. The momentum flux in the core is then given to a good approximation by two terms, one diffusive and the other convective. The effective momentum diffusivity can be expressed as

$$\chi_{\phi eff} = \chi_\phi \left(1 + \frac{R v_{pinch}}{\chi_\phi} \frac{L_{v\phi}}{R}\right) \tag{1.29}$$

where χ_ϕ is the actual momentum diffusivity, v_{pinch} is the momentum pinch velocity and

$$L_{v\phi} = -\frac{1}{v_\phi}\frac{dv_\phi}{dr} \tag{1.30}$$

The ratio Rv_{pinch}/χ_ϕ is defined as pinch number.

Through perturbative experiments [40,41], that allow to separate the diffusive and the convective contributions, the presence of a significant inward momentum pinch has been found. The actual Prandtl number can reach values near 1, consistently with theoretical predictions, while the effective Prandtl number, given by the effective momentum

diffusivity, achieves low values, consistently with steady-state experimental results. Values of the Prandtl number and the pinch number, and their parametric dependences are in good qualitative and quantitative agreement with theory predictions [39].

While experimental values of the χ_ϕ are found significantly higher than the neo-classical ones and then the anomalous component of the toroidal momentum transport is predominant, the transport behaviour of the poloidal rotation can in general be well described by the neo-classical theory.

1.4 Thesis motivation and contents

As described in the previous paragraphs, understanding the mechanisms at the basis of the transport of particles, momentum, electron and ion heat is a very challenging target, to which a large effort in the fusion research is dedicated. Theoretical studies aim at identifying and describing processes that give origin to anomalous turbulent transport. Experimental studies are carried out in order to investigate the values of the heat, momentum and particle diffusion coefficients, and their dependence of physical parameters, with a particular attention to experimental scenarios characterized by reduced turbulent transport. It is extremely important that a strong link is maintained between theory and experiment: on one hand theory provides ideas and predictions which then need to be validated by properly designed experiments, on the other hand unexpected experimental findings trigger new developments in theoretical research.

The ultimate scope is the understanding of transport mechanisms in order to be able to predict and improve the performance of fusion machines. This thesis aims at contributing to these efforts for what concerns ion heat transport in the plasma core. It includes both experimental and modelling work.

Whilst for electrons a wide theoretical and experimental investigation has been carried out during past years, the ion heat transport has been early addressed by extensive theoretical treatment, however a correspondent experimental work has been prevented by the lack of well resolved ion temperature diagnostics, so that through theory validation could not be carried out.

Recently detailed experimental studies on ion heat transport have become feasible, allowing to explore the values that the ion heat diffusion coefficient reaches and its dependences on the plasma physical parameters, and then to verify and quantify the critical behavior of the ion heat turbulent transport that has been theoretically predicted and only partially observed through experiments until now.

One of the aims of the present studies about the turbulent ion heat transport in the plasma core is to assess how the parameters ion stiffness and ion threshold, that characterize the instability of the ITG modes and then turbulent ion heat transport, depend on plasma physical and geometrical quantities, and what impact threshold and stiffness variations have on the global scale, that is on the plasma confinement and on the tokamak performances. In particular in this thesis the role that plasma toroidal rotation has on the ion stiffness is experimentally investigated, starting from the recent

experimental results obtained in the JET tokamak [27]. Such findings are then evaluated in the light of their impact on plasma scenarios, both in present machines and in ITER, a tokamak presently under construction, which has the aim of proving the scientific and technological feasibility of a full-scale fusion power reactor. Finally they are used to make advanced modelling of FAST, a future tokamak proposed for construction by the Italian fusion community. For such predictive work both new empirical models tight to experimental results and first principle fluid and gyro-fluid models have been used. In addition, linear gyro-kinetic theory has been applied in support to the simplified threshold predictions used for the FAST simulations.

A short theoretical description of ITG/TE instabilities, of their numerical modelling and of their experimental studies, and the description of the relevance of the toroidal rotation in the transport dynamics are presented in Chapter 2.

In Chapter 3 the data analysis of experimental studies about the separation of the role of the toroidal rotation and the rotation gradient in mitigating the ion stiffness level in the plasma core are reported, and results are presented.

Chapter 4 describes the simulation work to investigate the impact of stiffness on plasma performances, including a series of scans of ion stiffness, ion threshold, temperature pedestal height and injected power. We already know they have an influence on the global scale, but it is very important to give a quantitative estimate of the effect that these parameters have separately on the machine performance, also in order to indicate possible action criteria for the scenario improvement of present (JET) and future fusion machines (ITER).

Chapter 5 describes the predictive modelling work of the scenarios for the FAST machine, proposed as ITER satellite. It has been carried out taking into account the role that the plasma toroidal rotation has in the different analyzed scenarios, exploring the limits of the present transport models and combining theory based and empiric simulations with a strong link with experimental results obtained in several machines.

Estimates for ion threshold values for FAST machine, carried out through the gyrokinetic code GKW simulations, are reported in the Chapter 6.

Finally the results are summarized and implications on transport research are discussed (Chapter 7).

Chapter 2

Ion thermal transport in Tokamaks

In the plasma a large variety of waves can develop and propagate in response to a perturbation of a stationary state. As described in Chapter 1, the spatial inhomogeneities of the plasma temperature and density drive the drift modes, a family of waves that have a very relevant role in the mechanisms at the basis of the anomalous transport. In this Chapter we introduce the description of these modes through the fluid derivation of the drift velocities that characterize the plasma and the illustration of the ordering which defines the drift model. The drift waves are one of the main families of physical processes that the drift model takes into account. After the introductive paragraph 2.1.1 about the drift model, in paragraph 2.1.2 a theoretical fluid derivation of the dispersion relation and the instability analysis of the simplest drift mode is presented. Transport coefficients are estimated through a quasi-linear approach together with a mixing length rule in paragraph 2.1.3. We then report the derivation of the dispersion relation and the estimate of the relative transport coefficients for two particular drift modes. They are reactive modes, that is they do not need dissipative processes to become unstable. The dynamics of ion temperature gradient modes (ITG), that are supposed to be the main responsible of the ion heat transport in the plasma, is described in paragraph 2.1.4, where trapped electron modes (TE) are also presented, because the coexistence of the two modes is theoretically predicted and experimentally and numerically found. We proceed with the theoretical treatment in paragraph 2.1.5 reporting the role that the plasma rotation has on the instabilities at the basis on the ion heat transport, and in particular the **E**x**B** flow shear, a significant recognized mechanism of transport reduction, is described. In the theoretical description of ITG and TE modes the so-called Weiland model [42-44] is followed. However a large number of transport models have been exploited in order to characterize ITG and TE modes, some theory based, other empirical or semi-empirical. The models used in the simulations that have been carried out in this thesis work are presented in paragraph 2.2, pointing out the different approaches at the basis of everyone. Paragraph 2.3 reports experimental results about the anomalous heat transport for electrons and ions. Finally the experimentally observed role of the plasma rotation on the ion heat transport is described. Recent JET experimental results about the role of the toroidal rotation in mitigating the ion stiffness are presented in paragraph 2.3.3. These are the starting points of this thesis work.

2.1 Drift modes

In order to characterize the modes that are generated in inhomogeneous plasmas, the plasma fluid approach can be used. However it is known that the fluid description has to be provided by a closure of the equations system, that otherwise has more unknowns than equations, as described in paragraph 1.3.1 of this thesis.

If a magnetic field is present in the plasma, in the direction perpendicular to the magnetic field, the Lorentz force confines the particle motion. The ratio between the particle gyro-radius and the macroscopic scale size of the system is then a small parameter which can be exploited as basis of an asymptotic closure of the fluid equations. Parallel to the magnetic field a kinetic treatment is generally required. However we can restrict our analysis to the particular conditions that are fulfilled by the drift modes and that allow a fluid closure in the parallel direction too.

Drift modes that develop in the tokamak plasma are low frequency waves ($\omega << \omega_{ci}$, where $\omega_{ci},=eB/m_ic$ is the ion cyclotron frequency of the plasma) for which the inequality $\omega >> k_{||}v_{thi}$ holds. The cold plasma approximation is then done for ions, that seem to be stationary for fast enough processes as the drift waves. In addition $\omega << k_{||}v_{the}$. The wave evolution appears slow with respect to electrons, which respond "adiabatically", remaining close to the Maxwell-Boltzmann equilibrium.

2.1.1 The drift model

The fluid motion equation for the species α can be expressed as

$$\frac{\partial \mathbf{V}_\alpha}{\partial t} + (\mathbf{V}_\alpha \cdot \nabla)\mathbf{V}_\alpha = \frac{q_\alpha}{m_\alpha}(\mathbf{E} + \mathbf{V}_\alpha \times \mathbf{B}) - \frac{1}{n_\alpha m_\alpha}(\nabla p_\alpha + \nabla \cdot \mathbf{\Pi}_\alpha) + \mathbf{g}_\alpha, \tag{2.1}$$

where $p_\alpha=n_\alpha T_\alpha$ is the isotropic pressure, $\mathbf{V}_\alpha$ is the fluid velocity, q_α is the charge, m_α is the mass, $\mathbf{\Pi}_\alpha$ is the anisotropic pressure tensor of the fluid and external forces are represented by the term $\mathbf{g}_\alpha$. $\mathbf{E}$ is the electric field, $\mathbf{B}$ is the magnetic field. In the electrostatic limit in which $\mathbf{B}=B_0\hat{\mathbf{b}}$, taking the vector product of (2.1) with $\hat{\mathbf{b}}$ we obtain

$$\left[\frac{\partial}{\partial t} + (\mathbf{V}_\alpha \cdot \nabla)\right]\hat{\mathbf{b}} \times \mathbf{V}_\alpha = \frac{q_\alpha}{m_\alpha}\{\hat{\mathbf{b}} \times \mathbf{E} + B_0[\mathbf{V}_\alpha(\hat{\mathbf{b}} \cdot \hat{\mathbf{b}}) - \hat{\mathbf{b}}(\hat{\mathbf{b}} \cdot \mathbf{V}_\alpha)]\} + \\ -\frac{1}{n_\alpha m_\alpha}\hat{\mathbf{b}} \times (\nabla p_\alpha + \nabla \cdot \mathbf{\Pi}_\alpha) + \hat{\mathbf{b}} \times \mathbf{g}_\alpha. \tag{2.2}$$

The perpendicular component of the velocity of the considered fluid is then given by

$$\boldsymbol{V}_{\alpha\perp} = \frac{1}{B_0}\mathbf{E} \times \hat{\mathbf{b}} + \frac{q_\alpha}{m_\alpha B_0}\left[\frac{\partial}{\partial t} + (\boldsymbol{V}_\alpha \cdot \nabla)\right](\hat{\mathbf{b}} \times \boldsymbol{V}_\alpha) + \\ + \frac{1}{n_\alpha m_\alpha B_0}\hat{\mathbf{b}} \times (\nabla p_\alpha + \nabla \cdot \mathbf{\Pi}_\alpha) - \frac{m_\alpha}{q_\alpha B_0}\hat{\mathbf{b}} \times \mathbf{g}_\alpha. \tag{2.3}$$

If $\omega << \omega_{c\alpha}$, the second term on the right of (2.3) is smaller than the first one. Then we can substitute $\mathbf{V}_\alpha$ in the second term with the first one. Then we have

$$\mathbf{V}_{\alpha\perp} = \mathbf{V}_E + \mathbf{V}_{\alpha p} + \mathbf{V}_{\alpha *} + \mathbf{V}_{\alpha \pi} + \mathbf{V}_{\alpha g}, \tag{2.4}$$

where

$$\mathbf{V}_{\mathrm{E}} = \frac{1}{\mathrm{B}}\left(\mathbf{E} \times \hat{\mathbf{b}}\right) \tag{2.5}$$

is the **E**x**B** drift given by the electric field **E**. It has the same magnitude and direction for electrons and ions. A correction of the electric drift velocity is the polarization drift velocity, caused by the dependence of the electric field on time

$$\mathbf{V}_{\alpha \mathrm{p}} = \frac{1}{\mathrm{B}\Omega_{\alpha}} \frac{\mathrm{d}\mathbf{E}_{\perp}}{\mathrm{dt}} \tag{2.6}$$

The diamagnetic drift is due to the presence of a density or a temperature gradient in the plasma. It is a collective plasma motion resulting directly from the gyro-motion of the particles. It has the following form

$$\mathbf{V}_{\alpha *} = \frac{1}{\mathrm{q}_{\alpha}\mathrm{n}_{\alpha}\mathrm{B}_0} \hat{\mathbf{b}} \times \nabla(\mathrm{n}_{\alpha}\mathrm{T}_{\alpha}). \tag{2.7}$$

The drift due to the anisotropic pressure tensor is given by

$$\mathbf{V}_{\alpha \pi} = \frac{1}{\mathrm{q}_{\alpha}\mathrm{n}_{\alpha}\mathrm{B}_0} \hat{\mathbf{b}} \times (\nabla \cdot \boldsymbol{\Pi}_{\alpha}). \tag{2.8}$$

Finally

$$\mathbf{V}_{\alpha \mathrm{g}} = \frac{\mathrm{m}_{\alpha}}{\mathrm{q}_{\alpha}\mathrm{B}_0} \hat{\mathbf{b}} \times \mathbf{g}_{\alpha} \tag{2.9}$$

is the drift due to external forces. The drifts derived are fluid drifts. They can differ from actual particle drifts. The diamagnetic drift is a fluid drift and not a particle drift. The other drifts except $\mathbf{V}_{\alpha\pi}$ are the same for the fluid and particle description. Drifts due to the perpendicular magnetic field gradient and the curvature of the magnetic field lines are instead particle drifts but not fluid drifts. They can be written as

$$\mathbf{V}_{\alpha \mathrm{d}} = \frac{1}{\mathrm{q}_{\alpha}\mathrm{B}}\left[\mathrm{m}_{\alpha}\mathrm{v}_{\parallel}^2 \hat{\mathbf{b}} \times \left(\hat{\mathbf{b}} \cdot \nabla\right)\hat{\mathbf{b}} + \mu \hat{\mathbf{b}} \times \nabla \mathrm{B}\right], \tag{2.10}$$

where μ is the magnetic moment ($\mu = mv_{\perp}^2/2B$), which is a constant of the particle motion.

The drift model takes into account physical processes as the drift modes. In the limit of a magnetized plasma the Larmor radius ρ_L (where $\rho_{L\alpha} = m_{\alpha}v_{th}/q_{\alpha}B$) is much lower than the macroscopic scale size of the system L. Then $\delta = \rho_L/L$ is a small parameter. As we can see from the expression for the fluid velocities (2.5-2.10) the electric drift is the only velocity that does not depend on δ. The hypothesis at the basis of the so-called drift ordering [45] is to consider the electric drift of the order of δv_{th}, where v_{th} is the thermal velocity:

$$\frac{\mathrm{E}}{\mathrm{B}} \sim \delta \mathrm{v}_{\mathrm{th}}. \tag{2.11}$$

Relation (2.11) characterizes the electric field in the drift ordering, and differences it from the ideal MHD ordering, for which $E/B \sim v_{th}$, and in the MHD case the electric drift dominates on all the other drifts for a magnetized plasma. The drift ordering considerates moderate electric fields: electric forces are comparable to the pressure gradient. The electric drift is assumed to vanish like other particle and fluid drifts as $\delta \to 0$. Finite-δ effects (the so-called finite Larmor radius (FLR) effects) are usually retained to describe the dynamics across field lines. It is consistent to assume that time evolution is relatively

slow, otherwise the induced electric field from Faraday's law could contradict the relations (2.11). Characterizing the ideal MHD ordering by the transit frequency ω_t, the frequency proper to the drift ordering is

$$\omega \sim \delta\omega_t \sim \delta^2\omega_c \tag{2.12}$$

Because of the disparity between Larmor radii of different plasma species, FLR effects for electrons are usually neglected with respect to the ones for ions. As a result the drift model must account separately for different plasma species, and the two-fluid theory is used. In this description modes characterized by $k\rho_L<<1$ are considered.

2.1.2 Analytical description of drift modes in slab geometry

The drift modes, that depend on inhomogeneities of the plasma, can be described through the drift model. A simplified analytical description of the drift modes is given. A slab geometry of the plasma is assumed: the coordinates x, y, z correspond respectively to the radial, poloidal and toroidal coordinates of a tokamak device. As shown in figure 2.1, the magnetic field is parallel to z, a density gradient is present in the negative direction of the x axis. The temperature is assumed uniform. The existence of a density perturbation is assumed: it varies sinusoidally in the directions y and z, and it is constant along x. The electrostatic case $\mathbf{E}= -\nabla\phi$ is considered. In addition, perpendicularly to the magnetic field, the restriction of a perturbed wave length much smaller than the characteristic length of variation of the non-perturbed density is done. However the perturbed wave length is much larger than the Debye length. The frequency of drift waves is assumed to fulfill the following relation:

$$k_{\parallel}v_{th,i} \ll \omega \ll k_{\parallel}v_{th,e} \tag{2.13}$$

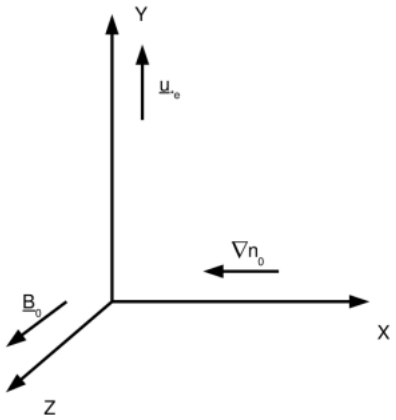

Fig. 2.1. Slab geometry for a drift wave.

Assuming the existence of electrons and one species of ions, every fluid is governed by the continuity equation

$$\frac{\partial n_{e,i}}{\partial t} + \nabla \cdot \left(n_{e,i}\mathbf{V}_{e,i}\right) = 0, \tag{2.14}$$

by the motion equation

$$n_{e,i}m_{e,i}\left[\frac{\partial \mathbf{V}_{e,i}}{\partial t} + \left(\mathbf{V}_{e,i}\cdot\nabla\right)\mathbf{V}_{e,i}\right] = n_{e,i}q_{e,i}\left(\mathbf{E} + \mathbf{V}_{e,i}\times\mathbf{B}\right) - \nabla p_{e,i} - \nabla\boldsymbol{\Pi}_{e,i} + \mathbf{R}_{e,i} \tag{2.15}$$

and by the Poisson equation that couples the two fluids dynamics (e is the elementary charge)

$$\Delta\phi = \frac{e}{\varepsilon_0}(n_e - n_i) \tag{2.16}$$

In the equations (2.14)-(2.16) $\mathbf{V}_{e,i}$ are the velocities of the fluid macroscopic elements, $q_{e,i}$ are the electric charges, $m_{e,i}$ the masses, $n_{e,i}$ the densities, $p_{e,i}$ the pressures, $\boldsymbol{\Pi}_{e,i}$ the stress tensors, $\mathbf{R}_{e,i}$ the collisional momentum referred to the electrons and ions respectively. For low frequency modes it is possible to replace Eq. (2.16) by the often used quasi-neutrality condition, $n_e=n_i$.

Taking into account the electronic fluid, the motion equation parallel to the magnetic field is the following (we do not take into account the stress tensor term and the collisional term because of neglecting electron inertia):

$$\frac{\partial V_{\|e}}{\partial t} + \left(\mathbf{V}_{e,i}\cdot\nabla\right)V_{\|e} = \frac{e}{m_e}\frac{\partial\phi}{\partial z} - \frac{1}{n_e m_e}\frac{\partial p_e}{\partial z} \tag{2.17}$$

For low frequency processes the electrons inertia terms on the left of the equation (2.17) can be neglected. In addition, electrons are isothermal ($\partial p_e/\partial z = T_e\,\partial n_e/\partial z$), and then

$$e\frac{\partial\phi}{\partial z} - \frac{T_e}{n_e}\frac{\partial n_e}{\partial z} = 0 \tag{2.18}$$

or in the integrated form

$$\frac{n_e}{n_0} = e^{\frac{e\phi}{T_e}} \tag{2.19}$$

where n_0, the equilibrium value of n_e is introduced. The equation (2.19) is the Boltzmann distribution, a good approximation if $k_{||}$ is not too small (it must be $\omega/k_{||}\sim 0$: it is according to the condition which ensures the fluid description validity). Writing $n_e=n_0+\delta n_e$ and expanding the exponential term for $e\delta\phi/T_e<<1$ we find

$$\frac{\delta n_e}{n_0} = \frac{e\delta\phi}{T_e}. \tag{2.20}$$

This result is in agreement with the estimate of the electron density perturbation that allows to substitute the equation (2.16) to the first order of the perturbation with the quasi-neutrality condition $\delta n_e=\delta n_i$. Electrons are characterized by a fast motion with respect to the variation of the electrostatic potential created by the disequilibrium of the electric charges, that tends to set a Boltzmann electron density distribution: it is the so-called electron "adiabatic response".

Ions do not view a quasi-static potential and their behavior is very different with respect to electrons. Assuming a very low ion temperature, such that $\omega >> k_{||}v_{thi}$, and then fulfilling the condition for using the fluid description also for ions, the equation (2.14) is rewritten as

$$\frac{\partial n_i}{\partial t} + \nabla \cdot (n_i \mathbf{V}_i) = 0 \tag{2.21}$$

where $\mathbf{V}_i = \mathbf{V}_{||i} + \mathbf{V}_{\perp i}$ and $\mathbf{V}_{\perp i} = \mathbf{V}_E + \mathbf{V}_{pi} + \mathbf{V}_{*i}$. We neglect the anisotropic stress tensor drift and the external forces drift. The component parallel to the magnetic field of the ion motion equation gives

$$V_{\parallel i} = \frac{k_\parallel}{\omega} \frac{e\phi}{m_i} \tag{2.22}$$

where the ion pressure term is neglected.

Assuming $k_x=0$ and since $\nabla\cdot\mathbf{V}_E=0$, $\nabla\cdot(n\mathbf{V}_{*i})=0$ and $\nabla\cdot(n\mathbf{V}_{pi})=n\nabla\cdot\mathbf{V}_{pi}$ (this last equality is caused by assuming $k_y >> d\ln n_0/dx$) the linearized equation (2.21) is

$$\frac{\delta n_i}{n_0} = \left(\frac{\omega_{*e}}{\omega} - \frac{k_y^2 T_e}{m_i \Omega_{ci}^2} + \frac{T_e}{m_i} \frac{k_\parallel^2}{\omega^2} \right) \frac{e\delta\phi}{T_e} \tag{2.23}$$

where $\omega_{*e}=k_y V_{*e}$ is the diamagnetic frequency. Combining the equation (2.23) with the (2.20) and using the quasi-neutrality condition the dispersion relation is obtained

$$\omega^2 \left(1 + k_y^2 \varrho_s^2\right) - \omega\omega_{*e} - k_\parallel^2 c_s^2 = 0 \tag{2.24}$$

where ρ_s is the ion Larmor radius at the electron temperature and $c_s=(T_e/m_i)^{1/2}$. The term $k_y^2\rho_s^2$ comes from the ion polarization drift and represents the influence of the ion inertia. It is one of the finite Larmor radius (FLR) effects. The dispersion relation is shown in figure 2.2.

For high $k_{||}$ the drift wave behaves as an ion acoustic wave, as shown in figure 2.2. If the ion inertia is negligible ($k_y\rho_s << 1$) the parallel ion motion can be omitted if $k_{||}c_s << \omega_{*e}$ in the dispersion relation, which reaches the form

$$\frac{\omega}{k_y} = V_{*e}. \tag{2.25}$$

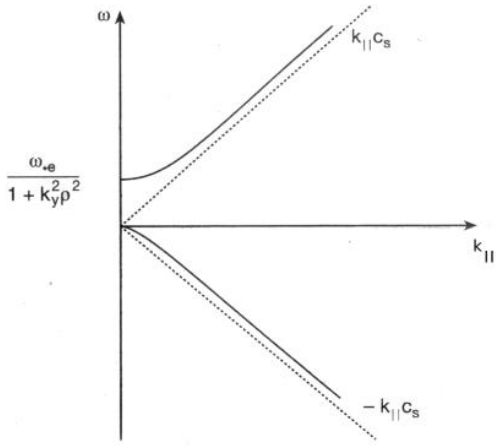

Fig. 2.2. Dispersion relation for drift waves ($T_i=0$) [42].

The propagation velocity of the density perturbation is the electron diamagnetic drift velocity. This is the most simple form of a drift wave. In order to illustrate the

mechanism at the basis of the drift modes and their instability, the density and the potential perturbations are represented in figure 2.3. They are in phase, as equation (2.20) shows, so the variation of the potential correspond to the density fluctuation. The fluctuating potential gives rise to an electric field **E**. It creates a plasma flow **E**x**B**, where **B** is the background magnetic field. The flow velocity $\mathbf{V}_E$ is directed such that it leads to oscillations of the perturbation, which remains stable and propagates in the y direction.

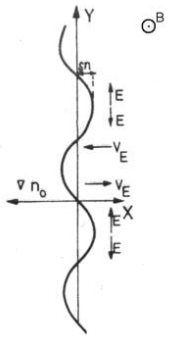

Fig. 2.3. The **E**x**B** drift generated by the potential ϕ causes a density variation because of the non-perturbed density gradient. The perturbation moves then parallel to the y positive direction, with a phase velocity that in the simplest case corresponds to the electron diamagnetic drift velocity V_{*e} [42].

When a phase difference exists between the density and the potential perturbations the equation (2.20) has to be modified and becomes

$$\frac{\delta n_e}{n_0} = \frac{e\delta\phi}{T_e}(1 - i\tilde{s}) \tag{2.26}$$

In the simplest case it gives rise to drift modes characterized by

$$\omega \approx k_y V_{*e}(1 + i\tilde{s}) \tag{2.27}$$

assuming $\tilde{s}$<<1. Since the perturbation is a time function of the form $e^{-i\omega t}$, the case $\tilde{s}$>0, for which the potential is delayed with respect to the density perturbation, corresponds to instability. The phase lag between potential and density perturbations can be given by several dissipative mechanisms, as electron-ion collisions, Landau damping, electron inertia.

This mechanism is always present for different kinds of drift waves in different regimes of plasma collisionality and for different geometries.

2.1.3 Transport coefficients: quasi-linear treatment and mixing length estimate

The instability of drift modes seems to be one of the main mechanisms at the basis of the anomalous transport that characterizes the plasma perpendicularly to the magnetic field in tokamaks. It is then important to obtain an expression for the fluxes of the transported quantities and then for the transport coefficients deriving them from the equations that

describe drift mode evolution and instability. Analytical methods use the quasi-linear approach, which is here described for the case of the particle flux.

The continuity equation is taken into account

$$\frac{\partial n_\alpha}{\partial t} + \nabla \cdot (n_\alpha \mathbf{V}_\alpha) = 0 \tag{2.28}$$

Where α indicates the species of the considered particles (ions and electrons). Densities and velocities are supposed to be given by the sum of the non-perturbed part and the perturbation.

$$n_\alpha = n_{\alpha 0} + \delta n_\alpha \tag{2.29}$$

$$\mathbf{V}_\alpha = \mathbf{V}_{\alpha 0} + \delta \mathbf{V}_\alpha \tag{2.30}$$

Where both terms on the right depend on the spatial and temporal coordinates. The non-perturbed quantity can be defined as $g_0 = \langle g \rangle$, and then $\langle \delta g \rangle = 0$. The symbol $\langle\rangle$ indicates the average over the period and the spatial variation of the perturbations.

Averaging the continuity equation (2.28), in which the densities and the velocities have been substituted by the ones of (2.29) and (2.30), we obtain

$$\frac{\partial n_{\alpha 0}}{\partial t} + \nabla \cdot (n_{\alpha 0} \mathbf{V}_{\alpha 0}) + \nabla \cdot (< \delta n_\alpha \delta \mathbf{V}_\alpha >) = 0. \tag{2.31}$$

This equation shows that the density evolution is influenced by a term that depends on the average of the product between the density and the velocity perturbations. This average is called quasi-linear flux:

$$\Gamma_{n\alpha} = < \delta n_\alpha \delta \mathbf{V}_\alpha >. \tag{2.32}$$

In fact subtracting the equation (2.31) from the continuity equation we have

$$\frac{\partial \delta n_\alpha}{\partial t} + \nabla \cdot (n_{\alpha 0} \delta \mathbf{V}_\alpha) + \nabla \cdot (\delta n_\alpha \mathbf{V}_{\alpha 0}) + \nabla \cdot (\delta n_\alpha \delta \mathbf{V}_\alpha) - \nabla \cdot (< \delta n_\alpha \delta \mathbf{V}_\alpha >) = 0. \tag{2.33}$$

Keeping only the first order terms in the perturbation we find the linearized equation, that does not include the last two terms. If the last term is considered the approach so-called quasi-linear is used. The expression (2.32) is then the quasi-linear particle flux. Applying the same method to the motion and energy equations, the momentum and heat quasi-linear fluxes are obtained

$$\Gamma_{(\mathbf{V}_\alpha)_j \alpha} = < (\delta \mathbf{V}_\alpha)_j \delta \mathbf{V}_\alpha >, \tag{2.34}$$

$$\Gamma_{T_\alpha \alpha} = < \delta T_\alpha \delta \mathbf{V}_\alpha >, \tag{2.35}$$

where j indicates the component of the considered velocity. The plasma inhomogeneity is assumed to be along the x axis, then the perturbations can be expressed in the form of harmonic waves, with a superimposed slow space variation of the amplitude due to the inhomogeneity

$$\delta a = \frac{1}{2}\left(a(x) e^{-i\omega t + i\mathbf{k}\cdot\mathbf{x}} + cc\right), \tag{2.36}$$

where cc means complex conjugate. The mean on the period and on the spatial length of the fluctuations for two perturbed quantities δa and δb is given by

$$< \delta a \delta b >= \frac{1}{2}(\sum_k a_k(x) b_k{}^*(x) + cc), \tag{2.37}$$

where the two perturbations are decomposed in Fourier series. The quasi-linear flux of particles in the x direction is then

$$\Gamma_{n\alpha x} = \sum_k \delta n_{\alpha k} \delta \mathbf{V}_{\alpha k}{}^* + cc. \tag{2.38}$$

In order to obtain the quasi-linear flux perpendicular to the magnetic field the transverse velocity perturbation is expressed as a function of the perturbed potential. For low frequency ($\omega << \omega_{ci}$) the dominant term of the perpendicular perturbed velocity is the electric drift one, given by

$$\delta \mathbf{V}_{\alpha\perp} \simeq -c\frac{\nabla\delta\phi\times\mathbf{B}}{B^2} = -ic\frac{k_y}{B}\delta\phi\hat{\mathbf{x}} \tag{2.39}$$

The perturbation of the velocity does not depend on the considered particle species. In Fourier components it becomes

$$\delta \mathbf{V}_\perp = \sum_k \delta \mathbf{V}_{\alpha k}(x) e^{-i\omega t + i\mathbf{k}\cdot\mathbf{x}} \simeq \sum_k \left(-ic\frac{k_y}{B}\delta\phi_k\hat{\mathbf{x}}\right) e^{-i\omega t + i\mathbf{k}\cdot\mathbf{x}} \tag{2.40}$$

In the case of the simplest drift wave instability the expression for the electron density perturbation is given by the (2.26). Substituting its expression and the expression for the velocity perturbation (2.40) in the (2.38), we obtain

$$\Gamma_{nx} = 2n_0 \frac{T_e}{eB} \sum_k \left|\frac{e\delta\phi_k}{T_e}\right|^2 k_y \tilde{s}_k, \tag{2.41}$$

where $\tilde{s}_k$ is the Fourier component of $\tilde{s}$, the coefficient of the imaginary part that makes the electron density perturbation deviate from the Boltzmann distribution. Then there is transport when density perturbation and potential perturbation are not in phase. For adiabatic electrons we do not have net electron transport. Following the Fick's law, which links the flux to its conjugate gradient through the diffusion coefficient (Γ=-D∇n), the diffusion coefficient is the following

$$D_e = -2\frac{T_e}{eB}\frac{n_0}{dn_0/dx}\sum_k \left|\frac{e\delta\phi_k}{T_e}\right|^2 k_y \tilde{s}_k \tag{2.42}$$

From equation (2.23), the ion density perturbation has the following form

$$\frac{\delta n_i}{n_0} = \frac{\omega_{*e}}{\omega_k}\frac{e\delta\phi}{T_e}, \tag{2.43}$$

if we neglect the terms of the ion parallel velocity and the ion polarization velocity, assuming $\omega_k >> k_{||}c_s$ and $k_\perp{}^2\rho_s{}^2 << 1$. Expressing $\omega_k=\omega_r+i\gamma_k$ the quasi-linear flux is then

$$\Gamma_{nx} = 2n_0 \frac{T_e}{eB} \sum_k \left|\frac{e\delta\phi_k}{T_e}\right|^2 \frac{k_y\gamma_k}{\omega_r{}^2+\gamma_k{}^2}\omega_{*e} \tag{2.44}$$

and the diffusion coefficient

$$D_i = 2\frac{T_e}{eB}\sum_k \left|\frac{e\delta\phi_k}{T_e}\right|^2 k_y \varrho \frac{c_s k_y \gamma_k}{\omega_r{}^2+\gamma_k{}^2} \tag{2.45}$$

In order to determine the level of the fluctuations an estimate of the saturation has been given through the mixing length rule. The instability saturates when the dominant non-

linear contribution (given by the convective **E**x**B** drift) becomes comparable with the term of the linear growth, that in the continuity equation can be shown to be

$$\frac{\partial \delta n}{\partial t} \sim \delta V_{Ex} \frac{\partial \delta n}{\partial x}. \tag{2.46}$$

Replacing the perturbed velocity with (2.38), and expressing the radial gradient as an effective characteristic inverse length k_x, that is assumed to be rough equally to k_y when the instability saturates (isotropic turbulence) we obtain

$$\frac{e\delta\phi_k}{T_e} \sim \frac{1}{k_x \varrho_s} \frac{\gamma_k}{k_y c_s}, \tag{2.47}$$

and then, assuming that the transport is determined by the fastest growing mode,

$$D_i = \frac{\gamma^3/{k_x}^2}{{\omega_r}^2+\gamma^2} \lesssim \frac{\gamma}{{k_x}^2} \tag{2.48}$$

The same method can be applied to the momentum flux and to the heat flux, giving

$$\chi_{i,e} = \frac{\gamma^3/{k_x}^2}{\left(\omega_r - 5/3\omega_{di,e}\right)^2+\gamma^2}, \tag{2.49}$$

$$\chi_\phi = \frac{\gamma^3/{k_x}^2}{{\omega_r}^2+\gamma^2} \tag{2.50}$$

The estimates (2.48), (2.49) and (2.50) are quite general expressions, however they are obtained through several simplifications and do not include off-diagonals elements, that can have a very significant role in carrying anomalous transport, as it is described in Chapter 1 of this thesis.

2.1.4 Reactive drift modes

In the above described treatment the drift modes generated only by the spatial inhomogeneity have been considered. They need a dissipative mechanism in order to be destabilized. Other drift modes do not require the existence of dissipative effects in order to become unstable. They are called reactive drift modes, and their instabilities are supposed to be a significant source of anomalous transport.

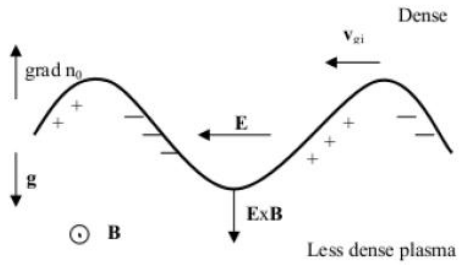

Fig. 2.4. Interchange instability mechanism.

The process responsible of the reactive drift modes is the interchange mode, which tends to exchange flux tubes of different pressure, causing then convective transport. It takes place in the presence of curved magnetic field lines. As described in the paragraph 2.1.1,

the magnetic field lines curvature leads to a particle drift motion. It is formally equal to that due to the centrifugal force $mv_{||}^2/2$ which acts on the particle in a magnetic field characterized by right field lines and it is directed perpendicularly to the magnetic field in the outgoing direction of the curvature radius. Reactive drift modes are unstable when the centrifugal force is in the opposite direction with respect to the pressure gradient. In this case the curvature is called unfavorable.

A similar fluid instability is the Rayleigh-Taylor one, that causes the fluids mixing when a light fluid supports a heavier fluid. In this case the density gradient plays the role of the pressure gradient and the centrifugal force is substituted by the gravity.

However in the plasma the physical process which leads to instability is more complex. The difference between the electron and ion curvature drifts together with the presence of a density perturbation lead to a charge separation that gives rise to an electric field perpendicular to the pressure gradient and to the magnetic field.

When the pressure gradient and the curvature force have opposite directions this electric field causes a **E**x**B** drift, which increases the perturbation, as shown in figure 2.4.

The interchange instability can take place for the drift modes mainly in two cases. The first one is due to the magnetic field lines curvature and the inhomogeneity of the magnetic field. They, together with the existence of an ion gradient of temperature can give rise to an interchange mode corresponding to a plasma compressibility (ITG modes) and then a charge separation.

The second case takes place when trapped electrons are present, because of the inhomogeneity of the magnetic field along the magnetic field lines. It restricts the parallel motion of the trapped electrons, that are not characterized by a Boltzmann distribution and, behaving similarly to the ions, are subjected to an interchange instability in the presence of an electron temperature gradient (TE modes).

2.1.4.1 ITG modes

The ion temperature gradient (ITG) modes take place in a plasma characterized by curved magnetic field lines and an ion temperature gradient. The instability of these modes grows on the low field side of the tokamak, where the curvature region is unfavorable and ∇B and ∇T_i are parallel. The curvature and the non-uniformity of the magnetic field lead to the drift velocity V_{di} (see eq. (2.10)), which is proportional to the ion temperature and is substantially oriented in the poloidal direction.

T_i is generally constant on a magnetic surface, unless a perturbation occurs for some reason. If T_i is perturbed the magnetic drift causes compressions of the ion density in the poloidal direction where T_i passes from higher to lower values (and the same happens for the drift, that is then characterized by a negative gradient) and rarefactions in the regions where the magnetic drift gradient is positive. Neglecting the presence of trapped electrons for simplicity, electrons are assumed adiabatic because of their fast dynamics, and then fulfill the Boltzmann distribution (2.13). The poloidal perturbation of the density is then

associated to a perturbed potential which causes a radial electrostatic drift. It carries plasma from the lower B side to the cold spot and from the higher B region to the warm spot. If the background ∇T_i is parallel to ∇B, the plasma coming from the lower B region is also colder, and it goes into the already cold spot. Then the perturbation grows and the instability develops.

In figure 2.5 a schematic description of the ITG instability mechanism is shown. This description offers insight, however the chain of cause and effect can be misleading. It is necessary to consider all the processes simultaneously to maintain persistent quasi-neutrality.

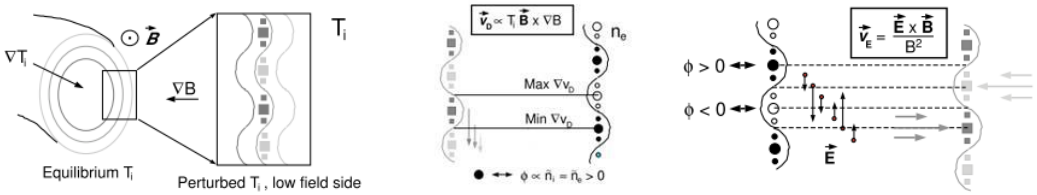

a) b) c)

Fig. 2.5. ITG instability mechanism. a) T_i perturbation on the low field side in presence of ∇B and magnetic field lines curvature. b) T_i dependent poloidal magnetic drift that causes compression/rarefaction of n_i. For the quasi-neutrality and the electrons adiabaticity assumption a perturbed electric potential is associated to the density perturbation c) The electric field caused by the existence of a potential gradient lead to a **E**x**B** drift. It gives rise to the instability if ∇B and ∇T_i are parallel [46].

In order to give an expression for the dispersion relation of the ITG modes and for the growth rate of the instability, the equations for the density, the continuity equation, and the ion energy equation of the two fluid approach has to been taken into account. We follow this scheme in order to obtain the dispersion relation for ITG modes:

- we assume harmonic perturbations of ion temperature, density and potential;
- we introduce the perturbation in the ion continuity equation, then we linearize it and we express their terms as functions of the perturbed quantities;
- we introduce the perturbation in the ion energy equation, then we linearize it and we express their terms as functions of the perturbed quantities;
- we assume the adiabaticity of electrons and the validity of the quasi-neutrality condition;
- substituting the various expressions for the perturbed quantities taken from the equations above written we obtain the dispersion relation.

We start considering the continuity equation. For ions we have

$$\frac{\partial n_i}{\partial t} + \nabla \cdot (n_i \mathbf{V}_E) + \nabla \cdot (n_i \mathbf{V}_{*i}) + \nabla \cdot (n_i \mathbf{V}_{pi}) + \nabla \cdot (n_i \mathbf{V}_{\pi i}) + \nabla \cdot (n_i \mathbf{V}_{||i}) = 0, \qquad (2.51)$$

where the drift velocities have been described in the paragraph 2.1 of this thesis. Parallel ion motion is neglected. This is reasonable because the fully toroidal ITG mode has the largest linear growth rate for $k^2\rho_s^2 \sim 0.1$, allowing to neglect the parallel ion motion ($\omega > k_{||} c_s$, where c_s is the sound velocity).

We introduce in the continuity equation a harmonic perturbation $\tilde{n}_i = n_i - n_{i0}$, where $\tilde{n}_i = \delta n_i e^{i(\mathbf{k}\cdot\mathbf{x}-\omega t)}$. ω, the frequency, is in general complex: $\omega = \omega_r + i\gamma$. In this formulation instability occurs for $\gamma > 0$. Linearizing the continuity equation we obtain

$$\frac{\partial \tilde{n}_i}{\partial t} + n_{i0}\nabla\cdot\tilde{\mathbf{V}}_{\text{drift}} + \nabla n_{i0}\cdot\tilde{\mathbf{V}}_{\text{drift}} + \tilde{n}_i\nabla\cdot\mathbf{V}_{\text{drift}} + \nabla\tilde{n}_i\cdot\mathbf{V}_{\text{drift}} = 0. \quad (2.52)$$

Assuming a zero background electric field the unperturbed electric drift velocities are null. For the other drift velocities the following expression can be derived:

$$-i\omega\tilde{n}_i = -\nabla n_{i0}\tilde{\mathbf{V}}_E - n_{i0}\nabla\cdot\tilde{\mathbf{V}}_E + \left\{-\nabla\cdot\left[n_i\left(\mathbf{V}_{pi} + \mathbf{V}_{\pi i}\right)\right] - \nabla\cdot\left(n_i\mathbf{V}_{*i}\right)\right\}_{\text{first order}}, \quad (2.53)$$

In order to find an expression for the second and the fourth terms of the right part of (2.53) we use the following relations that link the fluid drifts with the ∇B and curvature drifts (where here the curvature and ∇B drifts are the same as the relative kinetic drifts [42], however the quantities that characterize them are averaged over a Maxwellian distribution). In the limit of low β and then for electrostatic modes they are

$$\nabla\cdot\left(n_\alpha\mathbf{V}_{*\alpha}\right) = \frac{1}{T_\alpha}\mathbf{V}_{d\alpha}\cdot\nabla\tilde{p}_\alpha, \quad (2.54)$$

$$\nabla\cdot\tilde{\mathbf{V}}_E = \frac{2}{eB_0}\frac{q_\alpha}{T_\alpha}\mathbf{V}_{d\alpha}\cdot\nabla\tilde{\phi}. \quad (2.55)$$

For the third term of (2.53), the one with the polarization and the stress tensor drifts, the following expression can be derived [42]

$$\nabla\cdot\left[n_i\left(\mathbf{V}_{pi} + \mathbf{V}_{\pi i}\right)\right] = \nabla\cdot\left[\frac{n_i}{\Omega_{ci}}\frac{\partial}{\partial t}\left(\hat{\mathbf{b}}\times\mathbf{V}_i\right)\right] \approx -in_i k^2\varrho_s^2\frac{e\tilde{\phi}}{T_e}\left(\omega - \omega_{*i}(1+\eta_i)\right), \quad (2.56)$$

where $\eta_i = \frac{L_n}{L_{Ti}}$, $L_n = -\left(\frac{1}{n}\frac{dn}{dr}\right)^{-1}$, $L_{Ti} = -\left(\frac{1}{T_i}\frac{dT_i}{dr}\right)^{-1}$ and $\omega_{di} = \frac{k_\perp T_i \nabla n_i}{q_i n_i B}$ is the ion diamagnetic frequency.

The convective diamagnetic contribution to $\nabla\cdot(n\mathbf{V}_{pi})$ are exactly cancelled by the stress tensor contribution $\nabla\cdot(n\mathbf{V}_{\pi i})$. Making all the derivative of the perturbed quantities explicit and substituting (2.54), (2.55) and (2.56) in the (2.53) we obtain

$$-i\omega\delta n_i = -i\omega_{*e}n_i\frac{e\delta\phi}{T_e} - i\omega_{de}n_e\frac{e\delta\phi}{T_e} + in_i k^2\varrho_s^2\frac{e\delta\phi}{T_e}\left(\omega - \omega_{*i}(1+\eta_i)\right) + -i\omega_{di}\left(\delta n_i + n_i\frac{\delta T_i}{T_i}\right), \quad (2.57)$$

where $\omega_{d\alpha} = \frac{2k_\perp T_\alpha \nabla B}{q_\alpha B}$ is the curvature and ∇B frequency.

In order to find an expression for the perturbation of the ion temperature T_i we take into account the energy equation for ions, that, neglecting the collisional term and the stress tensor (because they are higher order in ρ_{Li}/L [43]), has the following form

$$\frac{3}{2}n_i\left(\frac{\partial}{\partial t} + \mathbf{V}_i\cdot\nabla\right)T_i + n_i T_i\nabla\cdot\mathbf{V}_i = -\nabla\cdot\mathbf{q}_{*i}. \quad (2.58)$$

The system of equations is not closed, and different transport models provide to close it with different methods. Following the Weiland treatment the ion heat flux $\mathbf{q}_i$ is given by the diamagnetic expression

$$\mathbf{q}_{*i} = \frac{5}{2}\frac{p_i}{m_i\Omega_{ci}}\left(\hat{\mathbf{b}} \times \nabla T_i\right). \tag{2.59}$$

It holds for the background electric field equal to zero and assuming $m_i\mathbf{V}_{*i}^2 << T_i$. This truncation closes the equations system. Assuming $\nabla T_i \perp \hat{\boldsymbol{b}}$ the ion diamagnetic heat flux can be expressed as

$$\nabla \cdot \mathbf{q}_{*i} = -\frac{5}{2} n_i \mathbf{V}_{*i} \cdot \nabla T_i + \frac{5}{2} n_i \mathbf{V}_{di} \cdot \nabla T_i \tag{2.60}$$

Neglecting the $k^2\rho_s^2$ terms, using the ion continuity equation and the relation $\mathbf{V}_{*i}\cdot\nabla(n_iT_i)=0$ we obtain

$$-\frac{5}{2} n_i \mathbf{V}_{di} \cdot \nabla T_i = \frac{3}{2} n_i \frac{\partial T_i}{\partial t} + \frac{3}{2}\mathbf{V}_E \cdot \left(n_i \nabla T_i - \frac{2}{3} T_i \nabla n_i\right) - T_i \frac{\partial n_i}{\partial t} \tag{2.61}$$

Taking into account a T_i perturbation of the same form as the ion density one and linearizing the equation (2.61), the relative ion temperature perturbation is given by

$$\frac{\delta T_i}{T_i} = \frac{\omega}{\omega - \frac{5}{3}\omega_{di}}\left[\frac{2}{3}\frac{\delta n_i}{n_i} + \frac{\omega_{*e}}{\omega}\left(\eta_i - \frac{2}{3}\right)\frac{e\delta\phi}{T_e}\right]. \tag{2.62}$$

Putting this expression into the equation for the ion density perturbation (2.57) we obtain a relation between the ion density perturbation and the potential perturbation.

Assuming adiabatic electrons, and then with an electron density perturbation given by the equation (2.20) and for the quasi-neutrality we obtain the following dispersion relation

$$\omega(1-\epsilon_n) - \left(\frac{7}{3} - \eta_i - \frac{5}{3}\epsilon_n\right)\omega_{di} - k^2\varrho_s^2\left(\omega - \omega_{*i}(1+\eta_i)\right)\left(\frac{\omega}{\omega_{*e}} + \frac{5}{3}\frac{T_i}{T_e}\epsilon_n\right) = \frac{N_i}{\omega_{*e}} \tag{2.63}$$

with $N_i = \omega^2 - \frac{10}{3}\omega\omega_{di} + \frac{5}{3}\omega_{di}^2$ and $\epsilon_n = \frac{2L_n}{L_B}$, with $L_n = -\left(\frac{1}{B}\frac{dB}{dr}\right)^{-1}$

Then

$$\omega_r = \frac{1}{2}\omega_{*e}\left[1 - \epsilon_n\left(1 + \frac{10}{3}\frac{T_i}{T_e}\right) - k^2\varrho_s^2\left(1 + \frac{1+\eta_i}{T_e}T_i - \epsilon_n - \frac{5}{3}\frac{T_i}{T_e}\epsilon_n\right)\right], \tag{2.64}$$

$$\gamma = \sqrt{\epsilon_n \frac{T_i}{T_e}}\frac{1}{1+k^2\varrho_s^2}\omega_{*e}\sqrt{\eta_i - \eta_{icr}}, \tag{2.65}$$

where η_{icr} is expressed by

$$\eta_{icr} = \frac{1}{2}\left(\frac{4}{3} - \frac{T_e}{T_i}\right) + \frac{1}{4}\epsilon_n\left(\frac{T_e}{T_i} + \frac{40}{9}\frac{T_i}{T_e}\right) + \frac{1}{4\epsilon_n}\frac{T_e}{T_i} +$$
$$-\frac{1}{2\epsilon_n}k^2\varrho_s^2\left[\frac{5}{3} - \frac{1}{4}\frac{T_e}{T_i} + \frac{1}{4\epsilon_n}\frac{T_e}{T_i} - \left(\frac{10}{3} + \frac{1}{4}\frac{T_e}{T_i} - \frac{10}{9}\frac{T_i}{T_e}\right)\epsilon_n + \left(\frac{5}{3} + \frac{1}{4}\frac{T_e}{T_i} - \frac{10}{9}\frac{T_i}{T_e}\right)\epsilon_n{}^2\right].$$

η_{icr} is the threshold term for the ITG modes. It is evident that for high η_i a reactive instability takes place. The value of the ratio between the inhomogeneity characteristic length of the ion density and of the ion temperature has a very relevant role. Assuming that the characteristic variation length of the magnetic field $L_B \sim R$ (where R is the major radius of the tokamak), we can express the instability in terms of the temperature gradient

length: $\gamma \propto \omega_{*e}\epsilon_n\sqrt{R/L_{Ti} - R/L_{Ticr}}$. The instability can grow, and then the anomalous transport takes place, when the inverse ion temperature gradient length $1/L_{Ti}$ exceeds a certain critical value $1/L_{Ticr}$.

Starting from the quasi-linear analysis and the mixing length estimate described in the paragraph 2.1.3 it is possible to derive the transport coefficients for ITG modes. Because of the adiabaticity of the electrons the particle diffusion coefficient is null. The ion heat diffusion coefficient is given by

$$\chi_i = \frac{1}{\eta_i}\left[\eta_i - \frac{2}{3} - \frac{10}{9}\frac{T_i}{T_e}\epsilon_n\right]\frac{\gamma^3/{k_x}^2}{(\omega_r - 5/3\omega_{di})^2+\gamma^2}, \tag{2.66}$$

where for γ the expression (2.65) yields. The threshold behavior of ITG modes is evident. The existence of the stiffness can be ascribed to a strong dependence on γ (to the power of 3) of χ_i together with a relevant coefficient that multiplies the threshold condition. For low changes in the ion temperature gradient the ion heat diffusivity and then the ion heat flux can vary significantly.

Several analytical expressions for the ITG ion threshold have been obtained, depending on different simplifications and assumptions. Here the F. Romanelli's formulation for the linear threshold is reported [47]

$$\eta_{icr} = \frac{4}{3}\left(1 + \frac{T_i}{T_e}\right)\left(1 + 2\frac{s}{q}\right)\frac{L_n}{R}. \tag{2.67}$$

In this formula q is the safety factor and s is the magnetic shear ($s=(r/q)dq/dr$). It is valid for the short wavelength limit ($k_\theta\rho_i \sim (L_{Ti}/R)^{1/4}$) and for flat enough density profiles ($L_n/R<2(1+T_i/T_e)$). It has been obtained starting from the dispersion relation coming from a gyro-kinetic treatment taking into account parallel ion dynamics, magnetic drift resonance and finite Larmor radius corrections. The resulting differential equation has been approximated neglecting one between the effects of parallel dynamics and curvature depending on the limit in which the physical parameters as the density gradient and s/q have been taken. Numerical solutions of the obtained simplified equations have shown that the ion threshold can be fitted with the expression (2.67). In this treatment electrons are considered adiabatic. It is used in the simulation work of this thesis.

2.1.4.2 TE modes

The trapped electron (TE) modes are caused by the existence of a spatial gradient of electron temperature. They take place when a part of the electron population is trapped, and then is not free to flow along the magnetic field lines. They have their parallel velocity reversed by magnetic mirror force before they can complete a full poloidal orbit. Trapped on the low field side of a flux surface, they describe the so-called "banana" orbits with a bounce frequency $\omega_{Be} = v_\parallel\sqrt{\varepsilon/2}/qR_{axis}$ (ε is the inverse aspect ratio, q is the safety factor and R_{axis} is the major radius at the axis position). Parallel to the magnetic field lines the motion of the trapped electrons is null if averaged over the bounce cycle.

For a drift wave with $\omega << \omega_{Be}$ (as it often happens because usually $\omega_{Be} \sim k_{||} v_{the}$) their parallel motion can be neglected and their dynamic is similar to the ion one. Then TE modes exist analogous to the ITG modes, mainly driven by an electron temperature gradient. In TE modes trapped electrons provide the role that ions have for ITG modes, and passing electrons provide the parallel dynamics.

The electron density perturbation can be expressed as

$$\frac{\delta n_e}{n_0} = f_t \frac{\delta n_{et}}{n_{et}} + (1 - f_t) \frac{\delta n_{ep}}{n_{ep}} \tag{2.68}$$

Where f_t is the fraction of trapped electrons, δn_{ep} is the passing electrons density perturbation, which follows the Boltzmann distribution (2.20), and δn_{et} is the trapped electrons density perturbation. Assuming quasi-neutrality and using for the ion density perturbation the expressions (2.57) and (2.62) we obtain the following ITG/TE dispersion relation

$$\frac{\omega_{*e}}{N_i}\left[\omega(1-\epsilon_n) - \left(\frac{7}{3} - \eta_i - \frac{5}{3}\epsilon_n\right)\omega_{di} - k^2\varrho_s^2\left(\omega - \omega_{*i}(1+\eta_i)\right)\left(\frac{\omega}{\omega_{*e}} + \frac{5}{3}\frac{T_i}{T_e}\epsilon_n\right)\right] =$$

$$= f_t \frac{\omega_{*e}}{N_e}\left[\omega(1-\epsilon_n) - \left(\frac{7}{3} - \eta_e - \frac{5}{3}\epsilon_n\right)\omega_{de}\right] + 1 - f_t, \tag{2.69}$$

where we have used for the density perturbation of trapped electrons the expression equivalent to the ion one and for passing electrons the expression coming from the Boltzmann distribution (2.20). We have supposed inertialess electrons and then we have neglected the finite Larmor radius effects for electrons. The resonant denominators N_i and N_e play a similar role. Near the resonances, the modes due to the ions and trapped electrons decouple. This happens for $R/L_n < 2$ and a good approximation of the dispersion relation can be obtained neglecting the part with the larger N_j. For $N_i >> N_e$ we obtain the trapped electron branch of the dispersion relation

$$\omega^2 + \omega\omega_{*e}\left[\frac{f_t}{1-f_t}\left(1 - \frac{2L_n}{R}\right) - \frac{20}{3}\frac{L_n}{R}\right] = -\frac{5}{3}\omega_{de}^2 - \frac{f_t}{1-f_t}\left(\eta_e - \frac{7}{3} + \frac{10}{3}\frac{L_n}{R}\right)\omega_{de}\,\omega_{*e}\,, \tag{2.70}$$

that gives the following expression for the real frequency

$$\omega_r = -\frac{1}{2}\omega_{*e}\left[\frac{f_t}{1-f_t}(1-\epsilon_n) - \frac{10}{3}\epsilon_n\right], \tag{2.71}$$

and for the growth rate

$$\gamma = \sqrt{\omega_{de}\,\omega_{*e}}\sqrt{\eta_e - \eta_{ecr}}\quad, \tag{2.72}$$

with threshold

$$\eta_{ecr} = \frac{10}{9}\frac{(1-f_t)}{f_t}\epsilon_n + \frac{2}{3} + \frac{f_t}{4(1-f_t)}\epsilon_n\left[1 - \frac{1}{4}\epsilon_n\right]^2. \tag{2.73}$$

For the TE modes the maximum growth rate is found for $k_\perp^2\rho_e^2 \sim 0.1$.

TE modes are characterized by a non null particle coefficient. Applying the quasi-linear analysis and the mixing length rule, it is given by

$$D = -\frac{\gamma^3/{k_x}^2}{{\omega_{*e}}^2} f_t \Delta_n, \tag{2.74}$$

with $\Delta_n = \frac{1}{N}\left[|\hat{\omega}|^2(1-\epsilon_n) + \hat{\omega}_r\epsilon_n\left(\frac{14}{3} - 2\eta_e - \frac{10}{3}\epsilon_n\right) - \frac{4}{3}{\epsilon_n}^2\left(-\frac{11}{3} + 2\eta_e + \frac{7}{3}\epsilon_n\right)\right]$,

where $N = \left[\hat{\omega}_r^2 - \hat{\gamma}^2 - \frac{10}{3}\hat{\omega}_r\epsilon_n + \frac{5}{3}{\epsilon_n}^2\right]^2 + 4\hat{\gamma}^2\left(\hat{\omega}_r - \frac{5}{3}\epsilon_n\right)^2$.

The quantities $\hat{\omega}_r$ and $\hat{\gamma}$ are normalized to the magnetic drift frequency of the electrons ω_{*e}.

From the ITG/TE dispersion relation the following ion heat coefficient is obtained

$$\chi_i = \frac{1}{\eta_i}\left[\eta_i - \frac{2}{3} - (1-f_t)\frac{10}{9}\frac{T_i}{T_e}\epsilon_n - \frac{2}{3}f_t\Delta_i\right]\frac{\gamma^3/{k_x}^2}{(\omega_r - 5/3\omega_{di})^2+\gamma^2}, \quad (2.75)$$

with

$$\Delta_i = \frac{1}{N}\left\{|\hat{\omega}|^2\left[|\hat{\omega}|^2(\epsilon_n - 1) + \hat{\omega}_r\epsilon_n\left(\frac{14}{3} - 2\eta_e - \frac{10}{3}\epsilon_n\right) + \frac{5}{3}{\epsilon_n}^2\left(-\frac{11}{3} + 2\eta_e + \frac{7}{3}\epsilon_n\right) + \right.\right.$$
$$\left.\left. - \frac{5}{3}\frac{T_i}{T_e}{\epsilon_n}^2\left(1 + \eta_e - \frac{5}{3}\epsilon_n\right)\right] + \frac{50}{9}\frac{T_i}{T_e}{\epsilon_n}^3\hat{\omega}_r(\epsilon_n - 1) - \frac{25}{9}\frac{T_i}{T_e}{\epsilon_n}^4\left(\frac{7}{3} - \eta_e - \frac{5}{3}\epsilon_n\right)\right\},$$

and the electron heat coefficient is

$$\chi_e = f_t\frac{1}{\eta_e}\left[\eta_e - \frac{2}{3} - \frac{2}{3}\Delta_e\right]\frac{\gamma^3/{k_x}^2}{(\omega_r - 5/3\omega_{di})^2+\gamma^2}, \quad (2.76)$$

with

$$\Delta_e = \frac{1}{N}\left\{|\hat{\omega}|^2\left[|\hat{\omega}|^2(\epsilon_n - 1) + \hat{\omega}_r\epsilon_n\left(\frac{14}{3} - 2\eta_e - \frac{10}{3}\epsilon_n\right) + \frac{10}{3}{\epsilon_n}^2\left(-\frac{8}{3} + 3\eta_e + \right.\right.\right.$$
$$\left.\left.\left. + \frac{2}{3}\epsilon_n\right)\right] + \frac{50}{9}\frac{T_i}{T_e}{\epsilon_n}^3\hat{\omega}_r(\epsilon_n - 1) + \frac{25}{9}\frac{T_i}{T_e}{\epsilon_n}^4\left(\frac{7}{3} - \eta_e - \frac{5}{3}\epsilon_n\right)\right\}.$$

2.1.5 Importance of the plasma rotation

Plasma rotation plays a significant role in improving the confinement of plasmas in tokamaks. The shear of the **E**x**B** velocity has a beneficial effect on energy confinement. It causes the reduction and sometimes the quenching of the turbulence and associated anomalous transport. This mechanism is experimentally and theoretically known and is related to the generation and the sustainment of reduced transport phenomena, as external and internal transport barriers and then to the improved confinement scenarios. Experimental studies have shown that often in tokamaks the development of a strong radial variation of the radial electric field E_r yields confinement improvement. It is observed near the internal and external transport barriers and also in improved confinement regimes. The link between the existence of an E_r gradient and the reduction of the anomalous transport can be described theoretically. The basic theoretical description of the **E**x**B** flow shear stabilization relies either on non linear decorrelation of turbulence [48] or linear stabilization of unstable modes [49]. Here it is illustrated by a simplified theoretical picture which is based on the dimensional scaling analysis [50,7].

In the plasma isotropic turbulent eddies, that are present in the plane perpendicular to magnetic field lines, are characterized by a size $L=1/k_{\perp 0}$ in the absence of a velocity shear. A radially varying E_r generates a sheared **E**x**B** velocity. When a general sheared

velocity $V(x)=S_v x$ is present in the plane (x,y) perpendicular to the magnetic field, after a time t the eddies become distorted, reaching ellipsoidal forms with major axis $L_l=L(1+S_v^2t^2)^{1/2}$. Since the area of the eddies is conserved, the minor axis is reduced by the same factor, and so the perpendicular wave number becomes $k_{\perp eff}= k_{\perp 0}(1+S_v^2t^2)^{1/2}$. A schematic view of the process is shown in figure 2.6. The time t is determined by the duration of the process. If t is larger than the correlation time, the eddy is only slightly distorted and there is essentially no effect on the turbulent dynamics. It t is less than the correlation time the differential flow stretches the eddy in a fraction of the correlation time. So the correlation time τ_c is shortened and becomes equal to t. It can be expressed as $t=\tau_c:=1/(D_0 k_{\perp eff}^2)$, where then $k_{\perp eff}= k_{\perp 0}(1+S_v^2\,\tau_c^2)^{1/2}$ and D_0 is the turbulent diffusion coefficient in the absence of velocity shear. In the limit of strong velocity shear ($S_v\tau_c >>1$) from the definition of τ_c and the expression of $k_{\perp eff}$ we can write $\tau_c \sim (D_0 k_{\perp 0}^2)^{-1/3} S_v^{-2/3}$. From the theory of mixing length an estimate of the density fluctuation amplitude δn can be given with respect to δn_0, the density fluctuation amplitude without velocity shear:

$$< \delta n^2 > k_{\perp eff}^2 \sim < \delta {n_0}^2 > k_{\perp 0}^2 , \tag{2.77}$$

and then

$$\frac{<\delta n^2>}{<\delta {n_0}^2>} \sim \frac{1}{1+S_v^2\tau_c^2}. \tag{2.78}$$

That means a significant reduction if $S_v\tau_c >1$. In cylindrical geometry the **E**x**B** velocity is equal to E_r/B and the condition $S_v\tau_c >1$ can be written as

$$\omega_E > \frac{1}{k_{\perp 0}^2 D_0}, \tag{2.79}$$

where $\omega_E=rd(E_r/rB)/dr$ is the **E**x**B** shearing frequency. D_0 can be given by its simple expression coming from the mixing length estimate (see eq. (2.46)) $D_0 \sim \gamma_L/k_\perp^2$, where γ_L is the linear growth rate of the dominant turbulence mode, then

$$\omega_E > \gamma_L. \tag{2.80}$$

In tokamak geometry the ω_E shearing rate is usually calculated according to the so-called Hahm-Burrel formula [51]

$$\omega_E = \left|\frac{(RB_\theta)^2}{B}\frac{\partial}{\partial \Psi}\left(\frac{E_r}{RB_\theta}\right)\right|, \tag{2.81}$$

where Ψ is the poloidal flux and R the major radius. The expression (2.80) is the simplest hypothesis for linear stabilization. However comparison with detailed calculations of several linear instabilities considered important in limiting the confinement of fusion plasmas indicates that it is not generally valid. Strong flow shear often stabilizes collective modes driven by gradients of pressure or other equilibrium quantities, but weak flow shear can be destabilizing for some collective modes. Hence there is no universal criterion for stabilization and the ideal of a collective linear mode in the presence of a flow shear is not generally realized in plasmas.

Several numerical studies show that the effect of flow shear on fluctuations involves some combination of the physics of linear stabilization and non linear decorrelation.

Even the generation of the **E**x**B** flow shear is not a simple phenomenon. It is linked to the radial component of the electric field, that can be expressed by the radial force balance equation

$$E_r = \frac{1}{Zen_i}\frac{\partial(n_i T_i)}{\partial r} - v_\theta B_\phi + v_\phi B_\theta, \tag{2.82}$$

where v_θ and v_ϕ are the poloidal and the toroidal velocities, B_θ and B_ϕ the toroidal and poloidal magnetic fields, n_i the ion density, Z the ion charge number, e the elementary charge. The eq. (2.82) indicates that there is a connection between the radial component of the electric field and the radial heat and particle transport through $\nabla(n_i T_i)$, the toroidal rotation through v_ϕ and the poloidal flow through v_θ. It is then evident the multiplicity of dependences and feedback loops of the **E**x**B** flow shear mechanism.

Despite these numerous complications, several simulation studies about ion gradient temperature (ITG) turbulence are based on the so-called Waltz rule [52], for which the **E**x**B** flow shear is taken into account considering as growth rate $\gamma_{net}=\gamma-\alpha_E\omega_E$, where γ is the growth rate calculated in absence of the **E**x**B** flow shear and ω_E is the **E**x**B** shearing rate. α_E is an adjustable coefficient. The Waltz criterion has been found a reasonable predictor for the quenching of ITG turbulence by flow shear [53], by increasing the ion threshold values with respect to those at zero **E**x**B** flow shear.

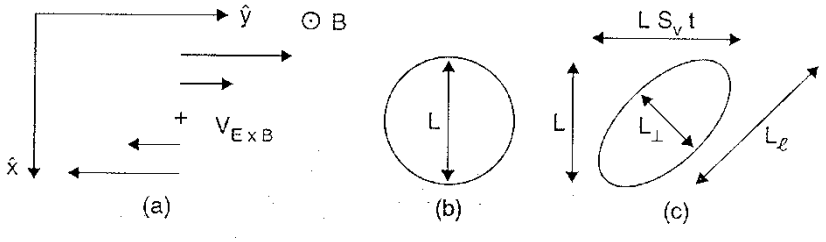

Fig. 2.6. (a) Representation of the velocity shear in the plane perpendicular to the magnetic field. (b) Circular eddy. (c) Distorted eddy in presence of the velocity shear [54].

2.1.6 Summary

In paragraph 2.1 the Weiland theoretical description of the drift modes has been reported. The drift ordering has been defined and the simplest drift wave, which is driven by spatial inhomogeneity, has been treated analytically, deriving the dispersion relation and making the stability analysis. This indicates the presence of a difference of phase between potential and density perturbations as necessary condition for the instability of the mode. From these results the analytical expression for the coefficients of the transport of particles, heat and momentum have been obtained through a quasi-linear approach and the mixing length rule.

The analyzed drift mode requires a dissipative mechanism to be destabilized. The reactive drift modes are wave that can become unstable without needing dissipative effects. They develop an interchange instability, and two significant examples are the ITG and TE

modes. ITG modes instability is due to the magnetic field lines curvature and the inhomogeneity of the magnetic field together with the existence of an ion gradient of temperature. In presence of an electron gradient of temperature the effect of the magnetic field inhomogeneity along the magnetic field lines on the trapped electrons causes the instability of TE modes ITG and TE modes, that are thought to be the main responsible for the ion heat transport in the core of tokamak plasmas, have then been analyzed, deriving their dispersion relation and the relative transport coefficients through the same approaches used for the simplest drift wave. For ITG modes the particle transport coefficient is null. The heat transport coefficient presents a threshold in the inverse of the characteristic length of the T_i variation, and the existence of the stiffness can be ascribed to the expression of the coefficient. For TE modes trapped electrons give a not null particle transport coefficient. TE modes exhibit a threshold in the inverse of the characteristic length of the T_e variation for the heat transport coefficient.

Among the plasma parameters that influence the drift modes instability, the plasma rotation has an important role, that has been described through a simplified theoretical model based on dimensional scaling analysis. The so-called **E**x**B** sheared velocity reduces the turbulence and the subsequent transport, improving the plasma confinement. Actually the mechanism at the basis is complex, involving linear stabilization and non-linear decorrelation. However numerical simulations have been found to well reproduce the impact of this phenomena on ITG turbulence through an empirical rule that consists in increasing the ion threshold.

2.2 Transport models

The theoretical treatment of the drift modes described above follows the principles of the so-called Weiland model. However several transport models have been developed in order to describe and give predictions about the anomalous transport caused by ITG and TE modes instabilities. The line of research that deals with the investigation and prediction of heat transport makes use of transport models, carrying out the profile modelling in order to interpret existing experimental data and to give predictions about the performances of next fusion devices. The so-called first principle transport models are theory based. They can be based on fluid equations, on gyro-fluid equations or on gyro-kinetic equations. In this thesis work the Weiland model, based on fluid equations, and the GLF23 model, based on gyro-fluid equations, are used. Both codes calculate transport coefficients through the quasi-linear approach together with the mixing length rule. The gyro-kinetic models will be treated extensively in Chapter 6 of this thesis. Semi-empirically based models have been also developed. Two of them have been employed for the transport studies of this thesis: the Bohm-gyroBohm model and the critical gradient model (CGM).

2.2.1 Weiland model

The Weiland model [44] is a fluid model based on the ITG and TE coupling. Passing electrons are assumed to be adiabatic. Trapped electrons dynamics is considered equal to the ion dynamics. Quasi-neutrality is supposed to hold also at the first order in the perturbations.

The fluid equations are retained up to the second moment, and the closure is given by the third moment by considering the heat flux as given by its diamagnetic component, as described in paragraph 2.1.2 of this thesis.

The fluid system is reduced to a 0D dispersion relation by assuming a fixed poloidal wave-vector $k_y^2\rho_s^2 \sim 0.1$, for which the maximum growth rate is found. Also the radial wave vector is fixed, $k_x \simeq k_y$. The Weiland model provides then the linear growth rate of the instabilities. Through the quasi-linear approach and the mixing length rule described in paragraph 2.1.3 of this thesis, the estimates for the particle, momentum and heat fluxes and for the conjugate transport coefficients are carried out, however taking into account all the off-diagonals and the convective terms.

In the complete treatment electromagnetic effects, parallel ion motion, finite Larmor radius effects in the lower order expansion, effects of impurity dilution and **E**x**B** flow shear stabilization are included.

2.2.2 GLF23 model

The gyro-Landau fluid (GLF) model [55,56] is based on modified fluid equations. The gyro-fluid equations are considered as starting point, and dissipative terms, like collisions and Landau damping are taken into account by adding terms in the energy and the momentum equations with arbitrary constants. These parameters are chosen in such a way that the model best fits the predictions given by linear gyro-kinetic simulations. In addition the overall level of transport is adjusted using one constant in order to match the results of non linear gyro-fluid and gyro-kinetic simulations. This matching procedure does not involve experimental results, using only theoretical results.

The model consists of eight equations for the ion density, the parallel and perpendicular ion pressure, the density and pressure for trapped electrons, the density for passing electrons, the parallel component of the vector potential and the quasi-neutrality equation.

The GLF23 model describes the transport driven by ITG modes, collisionless and dissipative TE modes, ETG modes (treated on the basis of their symmetry with respect to the ITG modes), ideal MHD ballooning modes and resistive inertial ballooning modes.

As in the Weiland model, a dispersion relation theoretic approach combined with a quasi-linear theory and a mixing length rule is used. A 0D dispersion relation is obtained using a wave vector representation perpendicular to the magnetic field, with radial and poloidal wave vectors taken to be equal. The quasi-linear fluxes of particles, heat, toroidal and

poloidal momentum are obtained starting with ten different values of poloidal wave numbers and summing over all the unstable modes. The saturation is calculated for each mode individually, and follows the mixing length rule that depends on the radial mode damping γ_d and on the growth rate γ. The Waltz rule [52] is used in order to take into account the effect of the **E**x**B** flow shear. A simplified estimate for the heat transport coefficient is the following

$$\chi = \frac{3}{2}\frac{\gamma}{k_x^{\,2}}\frac{\gamma\gamma_d}{\omega_r^{\,2}+\gamma^2}\,. \tag{2.83}$$

2.2.3 Bohm-gyroBohm model

The Bohm-gyroBohm model [57] is a semi-empirical model proposed and validated against a wide range of JET discharges. In addition, it has been tested against several discharges from different tokamak machines (DIII-D, TFTR, JT-60, ASDEX-U, START). The approach followed to devise this model is based on dimensional analysis. The diffusion coefficient of the heat transport can be written as

$$\chi = \chi_0 F(x_1, x_2, \dots)\,, \tag{2.84}$$

where χ_0 has the correct physical dimensions and usually the Bohm expression T_e/eB is used for it. F depends on properly chosen dimensionless plasma parameters, amongst which the normalized gyro-radius ρ^*. The scaling of F with ρ^* is linked to the scale length of the turbulence underlying anomalous transport, that is a microscopic quantity of the order of the gyro-radius if F is proportional to ρ^*. In this case the diffusivity depends only on the local plasma parameters and the transport properties are said to have a gyro-Bohm beaviour. If F does not depend on ρ^* the scale length of the plasma turbulence is proportional to the plasma minor radius and transport properties are said to be Bohm-like. Experimental results about ρ^*-scaling suggest that the plasma behavior cannot be described using a single scaling with the normalized gyro-radius.

The Bohm-gyro-Bohm model features a heat diffusivity given by the sum of a Bohm and a gyro-Bohm terms, a particle diffusivity given by a combination between the ion and the electron heat diffusivities and a momentum diffusivity assumed to be equal to the ion heat diffusivity. The expression for the ion and electron heat diffusivity is the following

$$\chi_{e,i} = \chi_{Be,i} + \chi_{gBe,i}\,, \tag{2.85}$$

where χ_B, the Bohm coefficient, is given by

$$\chi_{Be} = \alpha_B \frac{a|\nabla(n_e T_e)|}{n_e B_\phi} q^2 \left(\frac{T_e(0.8\varrho_{max}) - T_e(\varrho_{max})}{T_e(\varrho_{max})}\right) \Theta\left(c_1 + s - c_2\frac{\omega_E}{\gamma_{ITG}}\right) \tag{2.86}$$

and

$$\chi_{Bi} = 2\chi_{Be}\,, \tag{2.87}$$

where n_e is the electron density, T_e the electron temperature, B_ϕ the toroidal field, a the minor radius and q the safety factor. The Bohm diffusivity becomes dominant in the outer region of the plasma, and in order to take into account its non local character a

dependence on the value of the electron temperature in the edge region has been included. The q dependence ensures the reproduction of the observed experimental scaling of global confinement with plasma current. Θ is the Heaviside step function. It defines the internal transport barrier (ITB) formation through its argument, that is a control parameter. When the argument in the step function changes its sign, the ITB either forms or collapses. In the model, ω_E is the flow shearing rate and γ_{ITG} is an approximation for the linear growth rate of the ITG instability, defined as v_{thi}/R, where v_{thi} is the ion thermal velocity. The gyro-Bohm diffusivity is expressed by

$$\chi_{gBe} = \alpha_{gB} \frac{a|\nabla T_e|}{B_\phi} \varrho^* \tag{2.88}$$

and

$$\chi_{gBi} = 2\chi_{gBe}, \tag{2.89}$$

where $\rho^*=\rho_L/a$ is the normalized gyro-radius (where ρ_L is the gyro-radius and a the minor radius). The gyro-Bohm diffusivity dominates in the plasma core and defines the local character of the transport. The coefficients α_B and α_{gB} are empirically determined.

2.2.4 CGM model

The semi-empirical critical gradient model (CGM) [58,59] is a transport model proposed in order to quantify the plasma behavior which develops above ITG and TE threshold. The majority of existing first principle transport models features the existence of a threshold above which the transport switches from residual to highly turbulent. However each of them shows a different sensitivity to the threshold. The CGM covers the basic properties of turbulent transport though not all the physics known from first principle turbulence simulations. It parameterizes turbulent transport into a handful of variables, in particular it depends explicitly on threshold and stiffness. This parameterization makes possible an easy comparison with experiments, and also provides an easy access to the scaling laws of global confinement. It was initially developed for electron heat transport and it has been recently used also for ions.

The CGM is based on the existence of an instability threshold in the inverse temperature gradient length and of a finite background transport below the threshold. In addition it is characterized by an electrostatic gyro-Bohm scaling law. This latter assumption relies on theory and scaling studies and is assumed valid in the limit of a small normalized gyro-radius. In the CGM model the thermal diffusivity is written as

$$\chi_{e,i} = -\chi_{se,i} q^{\frac{3}{2}} \frac{T_{e,i}}{eB} \frac{\varrho_{s,i}}{R} \left[\frac{R}{L_{Te,i}} - \left(\frac{R}{L_{Te,i}}\right)_{cr}\right] H\left[\frac{R}{L_{Te,i}} - \left(\frac{R}{L_{Te,i}}\right)_{cr}\right] + \chi_0. \tag{2.90}$$

Here χ_0 is the background diffusivity, which accounts for the background transport below the threshold. χ_{si} is the ion stiffness factor; it quantifies the stiffness level and characterizes how strongly T_i profiles are tied to the threshold. The dependence of the heat diffusivity on q, the safety factor, allows recovering the experimentally observed dependence of confinement on plasma current and the radial increase of transport from

core to edge. n_i is the ion density, T_i the ion temperature, e is the electron charge, B is the magnetic field, R the major radius. $\varrho_i = (m_i T_i)^{1/2}/eB$ is the ion Larmor radius, where m_i is the ion mass. For electrons the $\varrho_s = (m_i T_e)^{1/2}/eB$ is taken. H is the Heaviside step function, that gives the threshold effect above a critical value of $R/L_{Te,i}$, $(R/L_{Te,i})_{cr}$. The theory foresees the ion heat flux to be linear with R/L_{Ti} far from the threshold. In the experiments a quadratic dependence of the electron heat flux on R/L_{Te} is found. For ions not too far from the threshold it is not possible to identify if the real dependence is linear or quadratic because of experimental uncertainties. However recent perturbation experiments and gyro-kinetic modelling work support taking the ion heat flux quadratic in R/L_{Ti}, and then the ion heat diffusion coefficient linear in R/L_{Ti}, as it is written in the equation (2.90).

The CGM model, first validated against discharges of the ASDEX Upgrade machine, has been tested in several different fusion devices.

2.3 Experimental studies

The theoretical predictions about the developing of the anomalous transport as driven by ITG and TE modes instabilities characterized by parameters as threshold and stiffness are substantially confirmed by experimental observations. Theory foresees that the heat flux increases strongly above a threshold value of the inverse temperature gradient length so that temperature gradients tend to stay close to values near the threshold. This property is called stiffness of the temperature profiles.

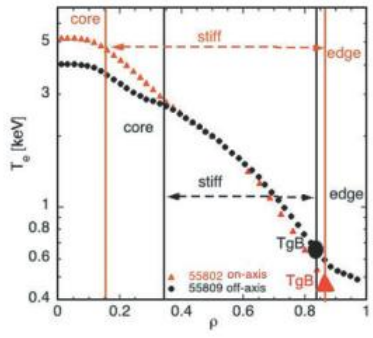

Fig. 2.7. Experimental T_e profiles for two JET discharges with NBI heating and on-axis (red) and off-axis (black) ICRH heating are shown in logarithmic scale. The thickness of the stiff region depends on the localization in the plasma of the additional heating [20].

Experimental studies show that the plasma does not have the same behavior at all radii. As it is shown in figure 2.7, where experimental electron temperature profiles are presented, three main regions can be identified according to the values that are reached by logarithmic temperature gradients. In the edge region the temperature of the plasma is low while its logarithmic gradient is well above the threshold value. In the stiff region, that is in the plasma core, the temperature increases and its logarithmic gradient is near the threshold. An approximate solution for the temperature profile is given by the

exponential shape $T(r) \approx T(r_e)e^{\left(\frac{R}{L_T}\right)_{cr}\frac{r_e - r}{R}}$, where r_e is the radius of transition between the edge and stiff regions, $(R/L_T)_{cr}$ is the threshold and R is the major radius of the tokamak. Finally the core region is characterized by a high temperature and by its logarithmic gradient under the threshold. In addition, figure 2.7 shows that the width of the single regions varies for different discharges. In this case it depends on the localization of the injected power deposition. The wider stiff region of the discharge represented with red triangles is due to on-axis heating. The black temperature profile belongs to an off-axis heated shot.

2.3.1 Methods to investigate the heat transport

In order to investigate experimentally the heat transport in tokamaks steady-state and perturbative studies have been carried out. In the steady-state analysis heat flux scans have been performed, using different additional heating systems and varying the level of power injected and the localization of the power deposition. In figure 2.8 a typical experimental schematic plot of the heat flux as a function of the inverse characteristic length of the temperature gradient R/L_T is shown. For values of R/L_T lower than a critical value (the threshold value) the heat flux reaches neoclassical values. Above the threshold value the heat flux grows strongly with R/L_T, as the transport becomes anomalous. Looking at the behavior of R/L_T, the tendency to stay close to the threshold value is evident. However experimentally different levels of stiffness have been found, as illustrated by the different curves.

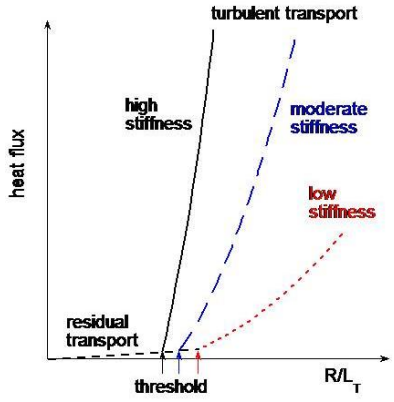

Fig. 2.8. Experimental schematic plot of the heat flux as a function of R/L_T. Above the threshold value different levels of stiffness have been found. High/medium/low stiffness characterize black/blue/red line.

Heat flux values are derived using codes for the calculation of the power deposition given by radio frequency and neutral beam injection additional heating systems. R/L_T are obtained through logarithmic fits of the temperature values of the considered zone. This analysis is local, however, as shown in figure 2.7, the stiffness region is a wide zone in

which we can think of a similar behavior of the plasma subject to anomalous transport mechanisms characterized by threshold and stiffness.

The heat flux is normally expressed in gyroBohm units. GyroBohm scaling has been predicted to characterize plasmas dominated by anomalous transport [20]. In the following formula the gyroBohm normalization is made explicit

$$q_{i,e}^{gB} = \frac{q_i}{(\rho_{i,e}/R)^2 v_{thi,e} n_{i,e} T_{i,e}}, \tag{2.91}$$

where $\rho_{i,e}$ is the ion/electron Larmor radius, R is the major radius of the tokamak, $v_{thi,e}=(T_{i,e}/m_{i,e})^{1/2}$, $n_{i,e}$ the ion/electron density and $T_{i,e}$ the ion/electron temperature.

Perturbative experiments have been widely used in order to complement the steady-state data and better determine threshold and stiffness values, especially when a large number of discharges, as required by a heat flux scan, is not feasible. T modulation allows to determine the slope of the heat flux vs R/L_T curve near the equilibrium point, i. e. they provide a rather accurate measurement of stiffness, whilst determination of threshold relies on the assumption of a curve shape for the extrapolation of zero flux. For the experiments discussed in this thesis, only steady-state methods have been used.

2.3.2 Electron heat transport

Several experimental studies in different devices have been carried out about the electron heat transport characteristics, and the existence of both the electron threshold and electron stiffness have been directly and indirectly observed. Correlation between edge and core T_e values has been observed, which is a sign of stiff behavior, because stiff profiles stay close to threshold so that the core and edge temperature values are directly linked.

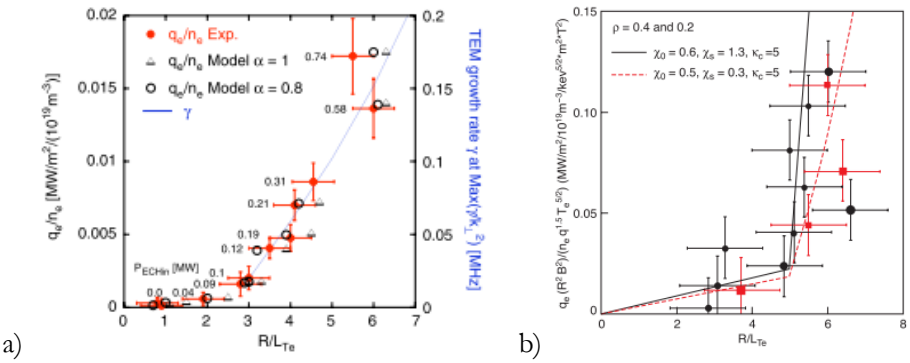

Fig. 2.9. Experimental and simulated electron heat flux density (a) and electron heat flux in gyro-Bohm units (b) as a function of the inverse electron temperature gradient length for ASDEX-Upgrade (a) and JET (b) discharges. (a) The line is given by gyro-kinetic simulations, red points are the experimental ones and black points are obtained by CGM based fluid simulations [61]. (b) Red points and lines refer to discharges with dominant electron heating. Black ones represent discharges with significant ion heating. Lines are the results of CGM based fluid simulations [60].

The results of the electron heat flux scans can be visualized in a plot of the electron heat flux, as shown in figure 2.9 for discharges of JET and ASDEX Upgrade. In both plots the change of slope of the electron heat flux is evident, as expected for the existence of a threshold. In the left plot it is shown to agree with the linear gyro-kinetic calculations indicated by the line and also with the points obtained using the CGM model. In the right plot the lines come from the fluid simulation using the CGM model, resulting from the best fit with experimental steady state and modulated data. Two different ranges of values of stiffness factor have been found for discharges with different type of heating as discussed in [60].

Perturbative studies have been extensively carried out [60,62]. A plot summarizing the electron stiffness and electron threshold found for different machines is presented in figure 2.10.

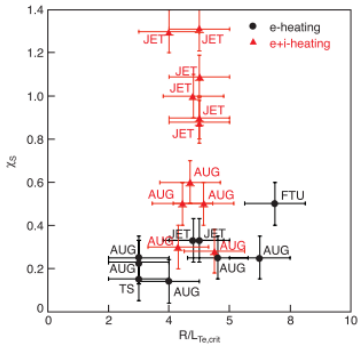

Fig. 2.10. Experimental values of electron stiffness versus the electron threshold for discharges with pure electron heating and with electron and ion heating (NBI) for several machines [60].

As shown in figure 2.10 the range of the electron thresholds is found between 3 and 8 for all the considered machines. They are in the range expected for the drift waves (see figure 1.8). The electron stiffness level shows a larger variability, reaching values between 0.2 and 1.3. For plasmas with pure electron heating similar values have been found in different machines. For electron and ion heating the electron stiffness reaches higher values. This suggests that electrons and ions are coupled and that a large amount of ion heating can induce a higher level of electron stiffness.

2.3.3 Ion heat transport

Experimental studies about ion heat transport have confirmed the critical temperature gradient behavior and the existence of profile stiffness also for the ion channel. A tight correlation between the core ion temperatures and the edge ion temperatures has been found. In addition a sharp change of the slope between the ion heat flux and the inverse of the ion temperature gradient length has been observed, similarly to the electron case (see figure 2.9). In figure 2.11, however, different values of the ion heat flux were obtained taking their values at different radii for the same shot, differently from the electron case, where the electron heat flux variation is obtained at the same radius

considering several similar shots, in which the deposition power profile varies. Because the threshold is not uniform in the space, the slope of the curve can be due to the mixed effect of the stiffness and the variation of the threshold, giving then a falsified determination of the stiffness.

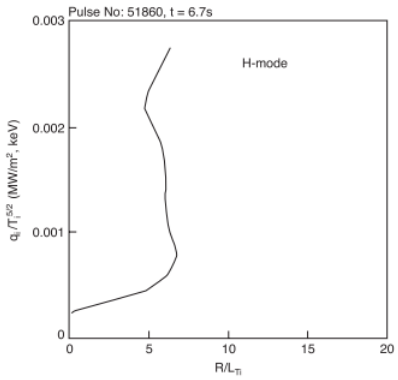

Fig. 2.11. Normalized ion heat flux as a function of the inverse ion temperature gradient for a JET discharge. Different heat flux values are obtained considering different radial positions of the same discharge [60].

Ion threshold and stiffness could be investigated in detail more recently with respect to the studies carried out for electrons. The essential reason was the unfeasibility of detailed observations and perturbative experiments for ions. In fact a method for localized ion heating and a T_i measurement with sufficient time resolution were not available simultaneously in the same device. Since 2006 ion heat flux scans and perturbative studies have been made possible at JET, using a particular kind of heating (the ion cyclotron resonant heating in the ^{3}He minority) and a high resolution diagnostic for the ion temperature measurements (upgraded charge exchange recombination spectroscopy). Direct experimental measurements of the ion threshold and stiffness have been carried out [57]. The CGM model seems to be a good tool to interpret data both of the heat flux scans and of the modulation experiments also for the ions. The modulation and the steady state data are found to satisfactorily fit the simulation results taking into account a radially increasing profile of the ion stiffness.

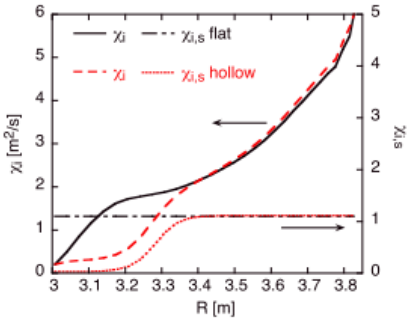

Fig. 2.12. Flat and increasing ion stiffness profiles and relative ion heat diffusivities used in the matching work between experimental data and simulations results [63].

Examples of increasing (hollow) and flat ion stiffness profiles used to match experimental results of JET discharges are shown together with the relative ion heat diffusivities in figure 2.12. As for the electron threshold scans of the ion heat flux down to neoclassical values have been achieved to identify the ion threshold value and its parametric dependences, as discussed in the next paragraph.

2.3.4 Mitigation of the ion stiffness

Recent experimental studies have shown that the ion heat transport and then the global plasma confinement can be influenced significantly by the plasma toroidal rotation [28]. In particular an ion stiffness level reduction is linked to a high rotation of the plasma. Figure 2.13 shows the ion heat flux as a function of R/L_{Ti} for discharges belonging to an experiment carried out in the JET tokamak. Discharges are homogeneous, that is with similar edge properties and plasma parameters as density, safety factor profile, T_e/T_i, Z_{eff}. In order to obtain different ion heat flux and rotation values the ion cyclotron radiofrequency heating (ICRH) system and the neutral beam injection (NBI) system have been used. ICRH has been used both on-axis and off-axis, varying then the localization of the power deposition. In addition the level of the input power has been varied for both ICRH and NBI systems. Since NBI are known to produce a torque which induces toroidal rotation, changing the level of the NBI power leads to different values of the rotation of the plasma.

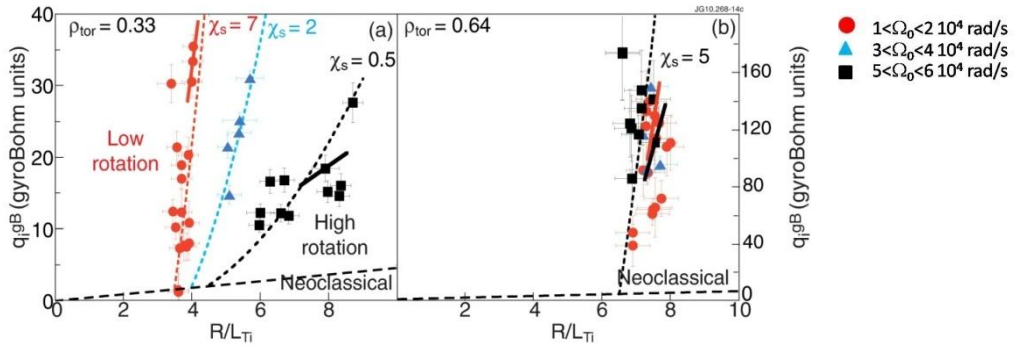

Fig. 2.13. Normalized ion heat flux (gyro-Bohm units) as a function of the inverse ion temperature gradient length in the inner (a) and outer (b) plasma region for similar plasmas and different levels of rotation (red points for low rotation, blue points for medium rotation, black points for high rotation). The segments indicate the local slope deduced from modulation. Dotted lines are given applying the CGM model with different ion stiffness values. Dashed line is indicative of neoclassical transport [29].

In figure 2.13a the analysis is carried out in the inner part of the plasma, at ρ=0.33. Three different curves are evident from this graph. The red circle points are characterized by a high stiffness level. They refer to discharges with low toroidal rotation. However blue and black points have a lower level of stiffness and the rotation values are higher for these points.

Calculating the ion threshold through linear gyro-kinetic codes gives the value $R/L_{Ticr} \simeq 3.5$, that is in agreement with the experimental threshold of the low rotation experimental data. An increase of the ion threshold for the high rotation curves can be supposed due to the flow shear effect, as described in paragraph 2.1.5. However calculations of this phenomena following the predictions of the Waltz rule for the considered JET discharges lead to a shift of the ion threshold much smaller than the one necessary in order to reach the measured values of R/L_{Ti} if the same high stiffness of the low rotation points were present. This is clearly not the case. Dashed lines indicate the predictions resulting from CGM model after a fitting work with the modulated and steady state data. The direct estimates of the stiffness level carried out directly by the modulation data are represented by the two solid segments in the graph. Both procedures indicate a clear decrease of stiffness with increasing rotation. Further confirmations of this behavior have been found from additional experimental studies.

In figure 2.13b the same analysis is shown for the outer part of the plasma (ρ=0.64). All the discharges are characterized by high stiffness level, independently of their rotation value. This difference of behavior in different regions of the plasma suggests a link with the spatial profile of the safety factor profile.

In figure 2.14 the results of a dedicated scan of the safety factor profile are presented for ρ=0.33, where families of points are divided according to their values of toroidal rotation and magnetic shear (s=(r/q)dq/dr).

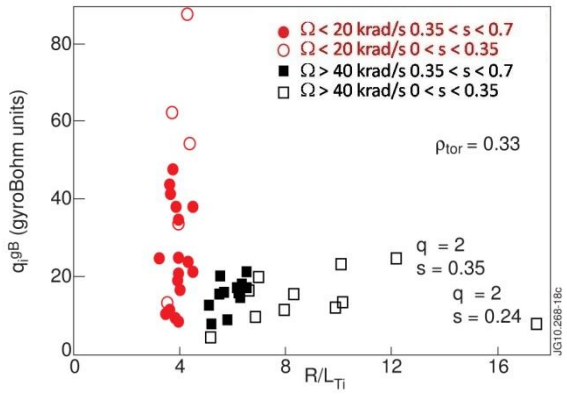

Fig. 2.14. Normalized ion heat flux (gyro-Bohm units) as a function of the inverse ion temperature gradient length in the inner plasma region for similar plasmas and different levels of rotation and magnetic shear (red (black) points for low (high) rotation, empty (full) points for low (high) magnetic shear) [30].

At low rotation the stiffness level is high and it is not influenced by the s values. For high values of rotation the stiffness changes significantly with varying q profile. This does not happen in the outer region of the plasma, where high stiffness is found for all the discharges, similarly to the figure 2.13b. Low values of s seem to be a necessary condition for the reduction of the ion stiffness by the plasma toroidal rotation. Confirmations of this behavior come from observations in the presence of rotation of the decrease of T_i

profile peaking with the current diffusion and associated peaking of the q profiles. It is verified analyzing T_i modulation data and from turbulence correlation measurements by reflectometry. This dynamic is completely absent in the case of low rotation.

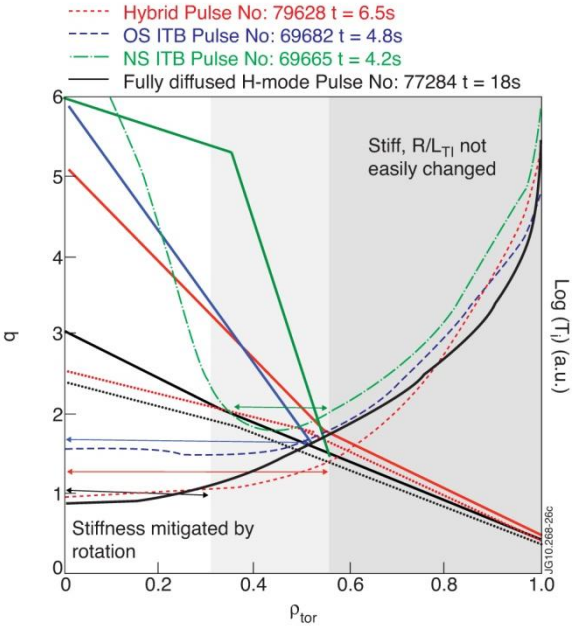

Fig. 2.15. Schematic graph of the q profiles and the relative ion temperature profiles in presence (full lines) and in absence (dotted lines) of the rotation. H-mode profiles are black colored, hybrids are red colored, AT regimes characterized by an ion ITB with an optimized q profile are in blue and AT regimes with a inverse q profile (negative magnetic shear) are green colored. Ion temperature profiles of AT plasmas in absence of rotation are not drawn. We can think they are very similar to the hybrid one. Without rotation, profiles are very stiff, and so very near to the threshold value. In addition ITB does not form in absence of rotation [30].

The reduction of the ion stiffness in presence of high rotation and low magnetic shear is supposed to be at the basis of all the situations characterized by higher core ion temperatures and then core ion improved confinement, as hybrids and AT scenarios, described in Chapter 1 of this thesis. In fact all these regimes present q profiles with broad regions of low magnetic shear s and have high rotation values. This new proposed paradigm, that is alternative to the usual interpretation for which the **E**x**B** flow shear and then the threshold up-shift are the main responsible for the higher confinement, can be illustrated by the schematic graph of figure 2.15.

Dotted T_i profiles show their threshold, which also represents the profile in absence of rotation, where the stiffness level is high and the ion temperature gradients are near to their threshold values. The presence of the rotation leads to the improved T_i profiles (full lines), which, in the region of the plasma where s reaches low values, can have much higher peaking because of the reduction of the ion stiffness. It happens in the inner plasma region, which is broadened in the case of hybrid or AT regimes with respect to H-mode plasmas. It allows to reach larger R/L_{Ti} values and then higher confinement. In the

outer region, where s reaches high values, the stiffness remains high and T_i profiles tend to be tied to the threshold values. Partial confirmations of this hypothesis have been found experimentally in improved confinement regimes [29].

For hybrid discharges low values of ion heat flux yield large values of R/L_{Ti}. This behavior can be given by a low stiffness level or an up-shift of the threshold. Without modulation data it is not possible to discriminate the actual cause. However, the ion threshold value obtained by linear gyro-kinetic calculations is found well below the experimental R/L_{Ti} values, and the threshold up-shift predicted by the Waltz rule is not sufficient to reach such high R/L_{Ti} values. The cause of the observed behavior seems to be a very low stiffness.

Analyzing a database of JET hybrid and H-mode discharges, R/L_{Ti} has been found to reach higher values for high rotation discharges with respect to low rotation shots. Comparing the observed R/L_{Ti} with the calculated ion threshold, high rotation shots have been found to have R/L_{Ti} well above the threshold, on the contrary low rotation shots R/L_{Ti} reach values very near the threshold. It seems that high rotation shots are characterized by low stiffness values and their T_i profile can significantly exceed the threshold, while low rotation shots have T_i profiles very stiff, that remain near the threshold value. This has been observed for low s values. In the case of high magnetic shear, R/L_{Ti} values of high and low rotation shots have been found very similar. In addition they are all near their threshold values.

Indications of the presence of a low stiffness level have been observed also for AT regimes. However the formation and the development of the ITB in the AT plasma scenario complicate the picture. The decreasing stiffness is supposed to play the major role in the sustainment of the ion ITB, with the threshold up-shift that intervenes in a non-linear feedback during the developing of the ITB.

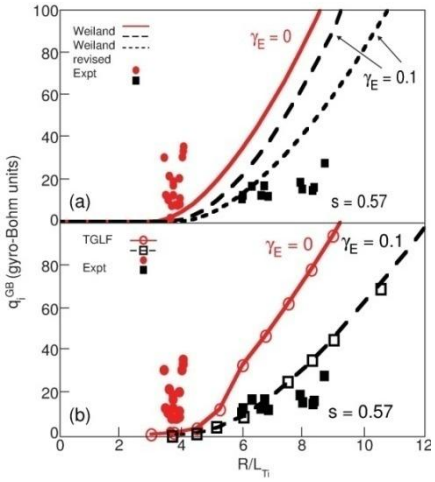

Fig. 2.16. Normalized ion heat flux (gyro-Bohm units) as a function of the inverse ion temperature gradient length. Points refer to experimental data of graph 2.13a. Lines are obtained through fluid simulations using (a) Weiland model and revised Weiland model, (b) TGLF in absence of rotation (red lines) and considering rotation (black lines) [30].

Several validation efforts of the experimental results on the ion heat transport and the role of the rotation on it have been carried out using quasi-linear fluid and gyro-fluid models and linear/non linear gyro-kinetic simulations [30]. Quasi-linear fluid models, as Weiland and GLF23, do not reproduce the experimental results and the change in the ion stiffness for high rotation shots. As figure 2.15a shows, only a small threshold up-shift effect is given by the simulations, because these models apply the Waltz rule on a given and restricted choice of spectral wave numbers that are chosen independently of the rotation. A recent revised Weiland model [64], in which the fastest growing mode number depends also on the rotation, shows a change in the slope of the curve given by the ion heat flux as a function of R/L_{Ti}, qualitatively reproducing the stiffness reduction effect as can be seen in figure 2.16a.

Also TGLF, a quasi-linear gyro-fluid model that makes use of all the wave number spectra, gives curves with different slopes for the cases with and without rotation, as figure 2.16b shows.

Several simulations have been carried out, and the more refined non linear gyro-kinetic models give results in worse agreement with experiments than the quasi-linear fluid models. No model correctly predicts the high stiffness level of the data in the absence of rotation. The impact of the rotation on the ion stiffness remains then an open issue on the theory side so far. Experimentally the ion stiffness has been found extremely high in non rotating plasmas, then in this case the ion temperature profiles are determined by the threshold behavior. In the presence of rotation, together with a low magnetic shear, the reduction of the ion stiffness leads to ion temperature profiles dominated by the stiffness level, and then it can produce the improvement of the ion core confinement.

The parametric dependences of the ion threshold and ion stiffness have to be investigated in this framework. In fact in the case of high rotation and low s the mitigation of the ion stiffness due to these two combined phenomena dominates over the threshold dependences. The effect that T_e/T_i has on the ion threshold has been experimentally investigated, in low rotation plasmas with similar q profiles. The impact of T_e/T_i has been found modest in the core region of the plasma for $T_e/T_i>1$. A small decrease of the ion threshold is observed with the growth of the ratio T_e/T_i, and this behavior has been confirmed by linear gyro-kinetic simulations and by theoretical predictions. However in these condition only values $T_e/T_i>1$ are able to be investigated, because it is experimentally impossible to produce low rotating plasma with $T_e/T_i<1$ since the stiffness level is high for the ions at low rotation. In the outer part of the plasma, where q profiles are peaked, a stronger dependence on T_e/T_i is theoretically expected. However here values of T_e/T_i significantly different from 1 are difficult to achieve. The impact of s/q on the ion threshold has been investigated too. At low rotation a very weak increase of the threshold with increasing s/q has been found.

Chapter 3

Discriminating the role of rotation and its gradient in determining ion stiffness mitigation in JET

The central role of ion temperature gradient threshold and stiffness in characterizing the turbulent ion heat transport has been described in Chapter 2 of this thesis. Knowing the dependence of threshold and stiffness on plasma physical quantities is then relevant to investigate how the ion heat transport and then the plasma performances can be improved. In particular recent experiments carried out in the JET device have shown that the plasma toroidal rotation, as reported in paragraph 2.3.4, has a significant effect of reduction of ion stiffness in the plasma core. However low (high) values of rotation corresponded to low (high) values of rotation gradient, so it was not clear if the effect of reducing the stiffness had to be ascribed to the absolute value of the rotation or to the rotation gradient. Experiments carried out at JET in order to separate the role of rotation and of rotation gradient in mitigating the ion stiffness level are described and analyzed in this Chapter. The tokamak JET is introduced in paragraph 3.1. Paragraph 3.2 gives a short description of the used heating systems. The diagnostics for obtaining the physical quantities that are at the basis of the data analysis of the discharges are presented in paragraph 3.3. The first experiment in which rotation and rotation gradient are decoupled is reported in paragraph 3.4: methods used to decouple rotation and rotation gradient, the experiment and the obtained results are described. In paragraph 3.5 a further data analysis of discharges with hollow rotation profile, and then positive gradient of rotation, is reported. Paragraph 3.6 summarizes the obtained results and contains some concluding remarks.

3.1 The Joint European Torus (JET) tokamak

JET is the largest tokamak machine in the world. It was designed to study plasma behaviour in conditions and dimensions approaching those required in a fusion reactor. The main aims of this machine are the investigation of heating, confinement and stability in reactor relevant plasma conditions, the optimization of operational scenarios, the investigation of plasma-wall interactions and the study of α-particle production, confinement, and consequent plasma heating.

The JET tokamak [65] is characterized by a major radius R=3 m and a plasma radius a=1.2 m. In the operational plane the poloidal cross-section is D-shaped, in order to

minimize stresses in the toroidal field coils and optimize confinement. The toroidal magnetic field is $B_T \leq 4$ T and plasma current is $I_P \leq 5$ MA. A divertor at the bottom of the vacuum vessel allows escaping heat and gas to be exhausted in a controlled way. In the period during which the experiments described in this thesis were performed, the first wall of the vacuum vessel was a carbon wall. Other important features of JET are:

- a plasma auxiliary heating system, consisting of Neutral Beam Injection (25 MW), Ion Cyclotron Resonance Heating (10 MW) and Lower Hybrid Current Drive (4 MW);
- a rich diagnostic set;
- a high frequency pellet injector for plasma re-fuelling and for ELM pacing studies;
- a massive gas injection valve for plasma disruption studies;
- capabilities to operate with Tritium fuel;
- Error Field Correction Coils.

3.2 Heating systems

3.2.1 Ohmic heating

For temperatures up to about 10^7 K (1 keV) tokamak plasmas are heated by the plasma current I_P through the Ohmic dissipation, because of the small but finite resistivity of the plasma. However the resistivity depends on the temperature as $T_e^{-3/2}$, so, in order to reach higher temperatures, of the order of the ones required for the ignition, additional heating is needed. The injection of energetic neutral beams and the resonant absorption of radio frequency electromagnetic waves are the two main mechanisms used to this scope.

3.2.2 Neutral beam injection (NBI) heating

In neutral beam injection heating systems, ionized particles are produced and accelerated to the required energy. Then they are neutralized by charge exchange in a gas target, and the residual ions are removed. When a high neutral beam energy is needed, positive ions sources, on which almost all present neutral injection systems are based, are not efficient, leading to a low neutral fraction. Using negative ions allows to reach much higher neutral fractions at high energy, but these sources are still under development. The produced neutral beam is injected into the plasma. The normal injection, that is perpendicular to the magnetic field, leads to ions losses caused by deviations from the ideal magnetic field structure due to the finite number of the toroidal coils (ripple effect). A more tangential injection reduces these problems, but the difficulty of access between the coils and the

increased pumping requirement in the longer drift ducts lead to constraints about the choice of the injection angle. In the plasma the injected atoms become ionized through collisions with the plasma particles, leading to ions and electrons with the same velocity and with the energy carried out almost entirely by the more massive ions. The fast ions are then slowed down and thermalized by Coulomb collisions, that transfer their energy to the plasma ions and electrons. The electron heating dominates initially, when the injection velocity is high, then the beam ions slow down, and the heating is transferred to the ions. For parallel injection, the fast ions also transfer their parallel momentum to bulk ions, inducing toroidal rotation. The large equipment size of the neutral beams system is a disadvantage of this heating mechanism, however it is compensated by the possibility of developing and testing it separately from the tokamak, in addition to predicting the heating profile independently of the magnetic configuration. In the following we will only describe ICRH which was the heating used in the experiment discussed in this thesis.

3.2.3 Radiofrequency (RF) heating

The second method of heating uses the electromagnetic waves to transfer energy to the plasma particles. The electric field of the wave accelerates the particles that collide with the plasma. However the collisional absorption is not efficient as heating mechanism, because it depends on the temperature as $T_e^{-3/2}$, similarly to the case of ohmic heating. The resonant absorption is instead a source of strong heating and becomes more efficient for increasing temperature. Several resonance frequencies capable of absorbing the energy of incident waves are present in magnetized multi-species plasmas. The most successful heating schemes are found to be ion cyclotron, lower hybrid and electron cyclotron heating.

3.2.3.1 Ion cyclotron resonance heating (ICRH)

The ion cyclotron resonance heating takes place for frequencies $\omega=\omega_{ci}$, where $\omega_{ci}=eB/m_ic$ is the ion cyclotron frequency. In this range of frequencies the typical propagating wave is the fast magnetosonic or compressional Alfven wave, which can be absorbed by one or more mechanisms or transformed into another type of wave. The absorption of the fast wave takes place when the wave frequency matches the fundamental ion cyclotron resonance frequency of one of the ion species in the plasma or a harmonic of it. Since the ion cyclotron resonance frequency is a function of the radial coordinate through the dependence of the magnetic field on it, the absorption region can be positioned by matching the wave frequency to the known toroidal field. The fundamental resonance of the majority species leads to a weak absorption. The main heating scenarios for this system are the second harmonic resonance of the majority species and minority schemes in multispecies plasmas. The absorption mechanism of the first scenario is a finite Larmor radius effect and only the most energetic ions interact effectively with the waves. In the minority heating scheme the wave power is absorbed

resonantly by the minority species at its fundamental cyclotron resonance. The resultant subpopulations with highly energetic tails transfer their energy to the bulk particles through Coulomb collisions. The conversion of the fast wave to one or more waves occurs in multispecies plasmas. The excited waves are absorbed by electron Landau damping and transit time magnetic pumping on the electrons, or by non linear effects on ions. The ICRH system has proved to be very successful in increasing the plasma temperature and it operates in a frequency range for which high power sources are readily available. Problems of impurities, that are partly responsible of the degradation in the confinement time, are the main disadvantage. They come from the antenna and its associated structures, that must be placed near the plasma in order to minimize the edge evanescence region of the fast wave allowing the tunneling of the wave and the wave-plasma coupling.

3.3 Diagnostic systems

Understanding the behaviour of tokamak plasmas, characterized by high temperatures ($T>10^7$ K (~1 keV)) and relatively low densities ($\sim 10^{19}$ to 10^{20} m^{-3}), and confined in a strong magnetic field (> 1 T) requires measuring a large number of plasma parameters, together with their spatial and temporal dependences. Because of the huge variety of aspects of the physics of plasma confinement and stability diagnostics for tokamak plasmas have been developed to study particular topics in tokamak research. The large spectrum of the diagnostics includes also complementary diagnostics, that measure the same physical quantity but have differing operational capabilities. In this paragraph we limit the treatment of the diagnostics to a short description of the physical principles behind those used for measuring the physical quantities useful for the experimental core transport studies carried out in the JET device and reported in this Chapter.

3.3.1 Electron cyclotron emission (ECE)

The electron cyclotron emission is a mechanism used for measurements of the plasma electron temperature profile. It is based on the emission of electromagnetic radiation due to the Larmor motion of the electrons around the magnetic field lines. The radiation takes place at the electron cyclotron frequency ω_{ce} and at its harmonics. The conditions of present tokamak plasmas (electron temperatures <10 keV, electron densities$<10^{20}$ m^{-3}) and the observations of the plasma at angles close to the perpendicular to the confining magnetic field allow to calculate the observed emission starting from the classical electrodynamics single particle emissivity and then integrating over the electron velocity distribution. Assuming a Maxwellian electron velocity distribution and taking into account transport and re-absorption of the radiation (the classical model of a radiating plasma is used) the radiation intensity for an homogeneous plasma of thickness L is given by

$$I(\omega) = I_B(\omega)(1 - e^{-\tau(\omega)}), \tag{3.1}$$

where

$$\tau(\omega) = \int_0^L \alpha(\omega) ds \tag{3.2}$$

is the optical depth, $\alpha(\omega)$ is the absorption coefficient and $I_B(\omega)$ is the blackbody radiation intensity. The frequency of the emitted radiation ω has a simple relation with the location of the point of emission because of the dependence of the toroidal magnetic field (that is the main component of the magnetic field) on the major radius R, $B_T=B_{T0}R_0/R$, where B_{T0} and R_0 are the toroidal magnetic field and the radius in the plasma centre. The ECE frequency, for observation at right angles to the magnetic field and along R is

$$\omega = n\frac{eB_0R_0}{m_eR}, \tag{3.3}$$

where n is the harmonic number. ECE occurs at long wavelengths because of the typical tokamak magnetic field strength, so the Rayleigh-Jeans approximation can be used, leading to

$$I_B(\omega) = \frac{\omega^2 T_e(R)}{8\pi^3 c^2}. \tag{3.4}$$

For tokamak plasmas some of the emission lines are optically thick ($\tau>1$) so $I(\omega)=I_B(\omega)$. Then measurements of the emission intensity in an optically thick harmonic gives the T_e profile through the simple relation

$$I_n(\omega) = \frac{\omega^2 T_e(R)}{8\pi^3 c^2}. \tag{3.5}$$

Four instruments for measuring the emission have been developed: microwave heterodyne radiometers, Fourier transform spectrometers, Fabry-Perot interferometers and diffraction grating spectrometers. In the JET device (paragraph 3.2) a modern ECE system is installed. It incorporates all the above written measuring instruments. They allow measurements of the electron temperature continuously in time with a time resolution < 10 μs and localized in space with a spatial resolution of a few cm.

3.3.2 LIDAR-High resolution Thomson scattering

The electron density is measured by the Thomson scattering mechanism, which is based on the scattering of electromagnetic waves by free electrons. It leads to a spectral broadening of the radiation due to the Doppler effect, that allows also the measurement of the electron temperature. Depending on the wavelength of the incident wave, the scattering of individual electrons can be added ($\alpha=(k\lambda_D)^{-1}<<1$), or collective effects due to correlated interactions between the plasma electrons have to be taken into account ($\alpha>1$). The most applied system is the first one, the so called incoherent Thomson scattering. The resulting spectrum is determined by the scattering of individual electrons. The power scattered per unit solid angle in the frequency bandwidth $d\omega$ as calculated by electromagnetic theory is given by

$$P_S = P_0 \frac{\partial s_T}{\partial \omega} n_e L S(k,\omega) d\omega, \tag{3.6}$$

where P_0 is the incident power, L the interaction length, $\partial s_T/\partial\omega$ is the differential Thomson cross section, derived by considering the acceleration experienced by an electron under the action of the electromagnetic field of an incident wave, and equal to $r_0^2 \sin\zeta^2$ (r_0 is the classical electron radius and ζ is the angle between scattered and incident wave). $S(k,\omega)$ is the form factor describing the frequency shift resulting from the electron motion (Doppler effect). For the case of a Maxellian distribution function it becomes for the incoherent case:

$$S(\lambda_S) = \frac{1}{\Delta\lambda_e \sqrt{\pi}} e^{-\left(\frac{\lambda_S - \lambda_0}{\Delta\lambda_e}\right)^2}, \tag{3.7}$$

where λ_s is the wavelength of the scattered radiation and $\Delta\lambda_e$ the 1/e width of the resulting spectrum:

$$\Delta\lambda_e \propto \lambda_0 \sin\left(\frac{\zeta}{2}\right)\sqrt{T_e}\,. \tag{3.8}$$

Then the electron temperature can be determined. By measuring the absolute level of the scattered power P_s, the electron density is obtained too. Relativistic effects are neglected in this treatment. They become important for plasmas characterized by temperatures of several keV, for which they must be taken into account for the calculation of the radiation spectrum. The incident radiation source needs to be a multimegawatt pulsed laser because the effect of the scattering is very weak, as the presence of the factor r_0^2 (equal to $8\ 10^{-30}$ m^2) in the expression of the scattered power shows. The method used in the JET machine is based on the LIDAR (Light Detection And Ranging) time-of-flight principle. A short laser pulse crosses the plasma generating the spectrum of the backscattered light. This spectrum is recorded as a function of the time by a fast detection and recording system. T_e and n_e are obtained by analyzing the spectrum through a spectrometer at each time point, at which the position of the laser pulse in the plasma is known too, allowing to have also the spatial dependences of T_e and n_e. In JET two LIDAR systems exist. For the core one the combination of the laser pulse length and detector response time gives a spatial resolution of about 10 cm, which means quite well resolved T_e and n_e profiles, because this length is considerably less than the minor radius of JET (equal to 1.2 m). The edge LIDAR system is characterized by a spatial resolution of about 2-3 cm. Since 2008 an HRTS system has been installed at JET, with the purpose of better resolving the steep gradients of electron temperature and density at the plasma edge and at the Internal Transport Barrier (ITB).

Two parallel laser beams are guided with the help of an assortment of mirrors and lenses. The beams finally enter the plasma vessel through a window on a horizontal port. While passing through the plasma the light scattered by electrons being hit by the laser beams is collected through another window on a vertical port. The changes in the back-scattered spectrum give information about the density and temperature of the plasma with a spatial resolution of 1,6 cm in the core and about 1 cm in the edge.

3.3.3 Charge exchange recombination spectroscopy (CXRS)

In tokamaks equipped with neutral beam injection, the ion temperature profile and the toroidal rotation profile are determined from the Doppler broadening and the Doppler shift of line radiation given by the reactions of charge exchange between the beam neutrals and plasma ions. The reaction can be written as

$$I^{z+}(\text{plasma}) + A(\text{injected}) \rightarrow I^{(z-1)+*}(\text{plasma}) + A^{+}(\text{injected}), \tag{3.9}$$

where A is the beam atom which does charge exchange with the plasma ion I that was in charge state z+ before the exchange. The ion is excited and can radiate its characteristic line spectrum when it decays. Assuming a Maxwellian distribution, the ion temperature can be calculated from the spectral line width

$$T_i = \frac{m_i}{k_B}\left(\frac{c\lambda_w}{\lambda_0\sqrt{8\ln 2}}\right)^2, \tag{3.10}$$

where m_i is the ion mass, k_B the Boltzmann's constant, c the speed of light, λ_w the full width at half maximum and λ_0 the wavelength of the transition. If the wavelength centre of the charge exchange recombination line is shifted with respect to an unperturbed line centre, the rotation velocity can be determined

$$v_{rot} = \frac{c\Delta\lambda}{\lambda_0}. \tag{3.11}$$

These relations are only valid under the assumption that Doppler broadening is the dominant mechanism determining the spectral line shape. Atomic physics effects can distort this simple picture and lead to a correction of the ion temperature and rotation.

3.3.4 Motional Stark effect (MSE)

The motional Stark effect (MSE) diagnostic is the standard technique for determining the q profile in tokamaks. As in the case of the CXRS, the injection of a neutral beam is needed for this diagnostic. The principle at the basis of the measurement relies on the Stark effect, that is the splitting of a spectral line produced by the electric field associated with an atom motion across a magnetic field. The energetic neutral beam, characterized by the high velocity **v**, passes through the magnetic field **B** and experiences a Lorentz electric field $\mathbf{E} = -\mathbf{v} \times \mathbf{B}$. The electric field causes the spectral emission to be split and polarized as described by the Stark effect. The Stark components of the split line are polarized either parallel or perpendicular to the electric field. When a hydrogen or deuterium beam is used, the Stark splitting is linear with the electric field and much larger than the Zeeman effect for beam energies above a few kilovolts. When viewed transverse to the induced electric field, different components in which are splitted the spectral lines are linearly polarized in different directions (parallel or perpendicular) with respect to the magnetic field. Polarimetry measurements of these directions result in a measure of the magnetic field pitch angle

$$\gamma_p = \tan^{-1}\left(\frac{B_\theta}{B_\phi}\right). \tag{3.12}$$

Some further knowledge of the plasma flux surfaces is needed to determine the q profile. The pitch angle is normally used as a constraint of the current density profile in reconstructing the plasma equilibrium using a free-boundary equilibrium reconstruction code. Measurements are slightly sensitive to the radial electric field, that has to be taken into account. The measured pitch angle, including a plasma radial electric field E_r, is given by

$$\gamma_{mp} = \tan^{-1}\left(\frac{v_b B_\theta \cos(\alpha+\Omega)+E_r \cos\Omega}{v_b B_\phi \sin\alpha}\right), \quad (3.13)$$

where γ_{mp} is the measured pitch angle, v_b is the beam velocity, α is the angle between the beam direction and the toroidal magnetic field and Ω is the angle between the viewing sightline and the toroidal magnetic field. The pitch angle and the radial electric field can be separated by two measurements that have a different sensitivity to E_r. This can be done in several ways. For example an E_r measurement can be made with a pair of views of the same beam at different angles Ω or different velocity components.

3.4 Rotation braking experiment

As reported in Chapter 2, the stiff region of the plasma temperature profiles is dominated by the anomalous transport, where the ion temperature gradients are above the ion threshold and tend to remain near this value even increasing ion heat flux. However this behaviour, called stiffness, is not the same for all the plasmas. The stiffness level can vary, and a wide interval of values has been found. If the stiffness is low the temperature gradient is less tied to the threshold value, and then can reach values much larger than the threshold ones. From the experiment described in paragraph 2.3.4 a strong link between rotation and stiffness level results. The experiment here described, carried out at JET, has the aim of separating the role of the toroidal plasma rotation and the toroidal rotation gradient in influencing the ion stiffness level.

3.4.1 Enhanced ripple and EFCC fields

In order to decouple the rotation and the rotation gradient values two known methods of plasma rotation braking have been used. The first one is based on the enhanced B_T ripple. In tokamaks the ripple, a periodic variation of the main toroidal field, exists because of the finite number of toroidal field coils. At JET it is possible to vary the BT ripple amplitude δ (defined as $\delta=(B_{Tmax}-B_{Tmin})/(B_{Tmax}+B_{Tmin})$) [66]. $\delta=0.08\%$ for standard JET operations, that are carried out with a set of 32 B_T coils carrying equal current. Because odd and even coils are powered independently, the imbalance current between the two coils set can be changed increasing the BT ripple up to $\delta=3\%$. The B_T ripple breaks the axi-symmetry of the magnetic field and enhances non-ambipolar losses of fast ions that induce a counter-torque leading to a significant reduction of both the edge and core rotation, but affecting less the core spatial rotation gradient [67-69]. The possibility of varying the ripple amplitude at JET and the significant effects that a large B_T ripple has

on the plasma rotation allow to alter the rotation with minor impact on rotational shear and without major changes to the scenario power level.

The second method consists of the application of low n external magnetic perturbation fields produced by the set of four external error field correction coils (EFCC) of JET [70]. Even in this case previous experiments show strong effects on the plasma rotation. The EFCCs set consists of four square shaped coils mounted outside the vacuum vessel. Depending on the wiring of the EFCCs either n=1 or n=2 periodic fields can be created. Low n perturbation fields break the toroidal symmetry. The plasma flows then along distorted flux surfaces and it is subjected to a drag toroidal force, defined by the neoclassical toroidal viscosity (NTV), that influences the plasma rotation and its gradient [71]. A reduction in toroidal rotation at different radii by the same factor ($gradv_\phi/v_\phi$=constant) has been observed over the whole plasma core and stronger rotation braking has been found near the edge pedestal [72-74].

3.4.2 Experimental set-up

The discharges carried out in the experiment described and analyzed here are characterized by the parameters reported in table 3.1.

	Standard	Enhanced B_T ripple	EFCC
I_p (MA)	1.5	1.5	1.5
B_T (T)	2	2	1.85
n_{e0} ($10^{19}m^{-3}$)	3	3	3
q_{95}	5	5	5
T_e/T_i	0.9-1.1	0.9-1.1	0.9-1.1
triangularity	low	low	low
number of experimental points	23	21	4

Table 3.1. Parameters of the discharges without braking rotation methods (standard), with enhanced B_T ripple and with the application of error field correction coils (EFCCs).

In this experiment, shots characterized by no methods of rotation braking (they are characterized by the JET standard B_T ripple δ=0.8% and error field correction coils are not used: in this thesis we call them standard shots), shots with enhanced B_T ripple and shots with application of EFCCs have been produced. All the obtained discharges are homogeneous with respect to the parameters listed in the table 3.1. The total injected power is kept fixed for all the shots. Ion Cyclotron Resonance Heating (ICRH) and Neutral Beam Injection (NBI) have been used as heating systems. However we have varied the strength of the power coming from the individual heating systems. In

particular NBI heating power has been changed from 4 to 7 MW, in order to obtain shots characterized by significant plasma toroidal rotation values in the cases in which methods of rotation braking have not been applied. For discharges where enhanced B_T ripple or EFCCs have been switched on, the rotation reaches reduced values. With this procedure a large spectrum of toroidal rotation values has been obtained. ICRH heating power has been varied from 0 to 2 MW and the localization of the power deposition has been changed too. It has been applied both on-axis and off-axis (in this last case the peak of power deposition is for $\rho \sim 0.7$, where ρ is the square root of the normalized toroidal magnetic flux). For the ICRH heating the (H)-D minority scheme has been used with $n_H/n_e \sim 8\%$ and 20-30% of the ICRH core power delivered to thermal ions. Different localizations of the power deposition give rise to different ion heat flux values in the core of the plasma.

Power deposition profiles are obtained by code calculations. The PION code [75] is employed for ICRH heating. It uses a ray-tracing package to derive input power and provides a calculation of the plasma heating by ion cyclotron resonance frequency waves through a power deposition model and a time dependent Fokker-Planck solver, giving as results a consistent power deposition profile and a velocity distribution of resonating ion species. It can take into account second harmonic ion resonances and the presence of neutral beam introduced fast ions. For NBI power deposition a first analysis has been done using the code PENCIL [76]. It solves a simplified Fokker-Planck equation that is used to describe the fast ion dynamics. Fast ion self-collisions and the effects of toroidal electric field on the fast ion dynamics are neglected. The resulting bounce averaged Fokker-Planck equation is then solved using an eigenfunction expansion in the pitch angle variable. The PENCIL code does not take into account the ripple effect, so three representative discharges (one with enhanced B_T ripple, one with standard ripple and one with the application of EFCCs fields) have been reprocessed with ASCOT [77,78]. It is a guiding center orbit-following Monte Carlo code that includes in the calculations fast ion losses due to the enhanced B_T ripple. It uses as an NBI source for ion birth profile the code PENCIL. In ASCOT the binary collision model can be used and the electric field can be solved self-consistently using as basis the collective motion of the test particles. An example of the obtained NBI power depositions is shown in figure 3.1. As we can see, the ripple effect has been found negligible for $\rho < 0.4$, allowing to calculate the NBI power deposition values in the core without any ripple correction. The ion NBI power deposition profiles obtained by ASCOT have been found higher than using PENCIL code (according to [79]), with the same percentage difference for all the discharges between the two code calculations. The PENCIL NBI ion heat fluxes have then been corrected by this percentage difference.

Through the spatial integration of ion power density profiles and determining the collisional electron-ion transfer by means of interpretative transport simulations we can calculate the radial ion heat flux.

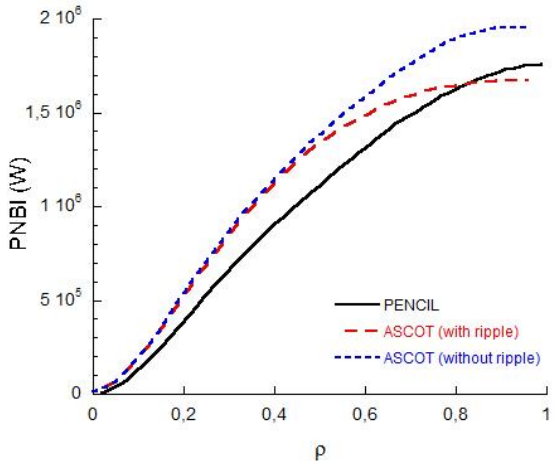

Fig. 3.1 Power deposition of NBI heating system as calculated by PENCIL code and by ASCOT code with and without the inclusion of the enhanced B_T ripple effect. Shown profiles refer to the enhanced B_T ripple shot 77010 at the time of 5 s.

Physical quantities required by our data analysis are ion temperature, toroidal rotation and their gradients, electron density and safety factor. Values of ion temperature and toroidal rotation have been averaged in time over a stationary interval. The gradient of ion temperature has been obtained by an exponential best-fit over 4 CX (Charge Exchange Spectroscopy) channels, while for the toroidal rotation gradient a linear fit over 4 CX channels has been used. In both cases, fits are centered on the chosen radial position and the measured quantities are averaged in time over a stationary interval. They are calculated with respect to the flux surface minor radius, $\rho_{gs2}=(R_{out}-R_{in})/2$, where R_{out} (R_{in}) is the outer (inner) boundary of the flux surface on the magnetic axis plane.

3.4.3 Data analysis and experimental results

In order to understand if the methods of rotation braking have led to an actual decoupling between the plasma toroidal rotation values and their gradients the graph represented in figure 3.2 has been built. It shows the rotation as a function of the relative rotation gradient for the discharges of the experiment. The analysis has been carried out at the radial position $\rho=0.25$: it encloses the on-axis ICRH power but not the off-axis one, giving the maximum ion heat flux scan, useful in order to investigate the stiffness level of the analyzed shots. Discharges without methods of rotation braking present higher values of rotation and rotation gradient with respect to discharges in which enhanced B_T ripple or EFCCs have been applied. The enhanced B_T ripple shots reach higher values of rotation gradient relative to the rotation value if compared with the trend proper of the standard discharges. Shots where EFCCs are switched on are in line with the standard discharge trend. Only enhanced B_T ripple seems to be able to decouple rotation and rotation gradient for discharges characterized by the values of table 3.1 and with the above described heating powers. It is then possible to investigate the role that rotation and rotation gradient have separately on the ion stiffness.

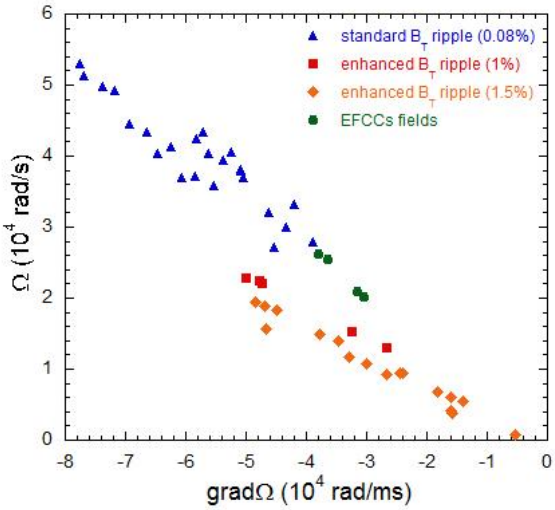

Fig. 3.2 Toroidal rotation as a function of toroidal rotation gradient for standard B_T ripple (triangles), enhanced B_T ripple (squares 1% and diamonds 1.5%) and EFCCs (circles) shots. Rotation and its gradient have been taken at ρ=0.25. Larger B_T ripple leads to lower values of rotation with respect their gradients, and then larger decoupling between rotation and rotation gradient.

To this aim, a first analysis has been done comparing ion temperature profiles of plasmas characterized by similar gradient of rotation and different rotation values.

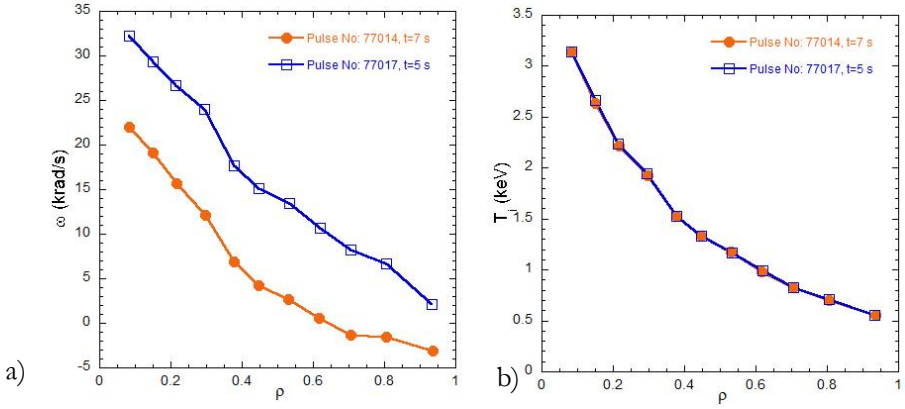

Fig. 3.3 Toroidal rotation profiles (a) and relative ion temperature profiles (b) of two analyzed shots: one is standard (77017) and the other is characterized by enhanced ripple (77014). In the neighbourhoods of ρ=0.25 the shot number 77014 (line with circles) is characterized by a value of rotation gradient similar to the one of the shot number 77017 (line with squares). The represented profiles are taken at the times indicated in the legend of the graphs.

In figure 3.3 an example of this comparison is shown. It refers to one of the shots with enhanced B_T ripple characterized by reduced rotation with respect to rotation gradient and a standard shot with similar power level and plasma parameters except for the ripple level, with the same value of rotation gradient and associated larger rotation. As shown in

figure 3.3b, where ion temperature profiles for the two shots are presented, ion temperature and their gradients are identical, even if the values of rotation differ significantly. This is verified not only around the radial position ρ=0.25 but along all the temperature profiles. We can note that the rotation profiles are characterized by very similar gradients for every radius (the perfect match of the two profiles has to be considered a coincidence).

Through enhancing the B_T ripple or applying the EFCCs fields, discharges with a reduced rotation gradient with respect to rotation cannot be produced, therefore, limiting to shots of this experiment, a comparison between plasmas with similar values of rotation and different rotation gradient is not feasible. However using as auxiliary heating counter-NBI in reverse I_P configuration is known to produce plasmas with flatter and lower toroidal rotation with respect to the corresponding co-NBI plasmas because of off-axis torque deposition [28,80]. A discharge that belongs to a different experiment, characterized by parameters very similar to the ones of table 3.1 and heated by counter-NBI with a power strength nearly equal to the power of our experiment shots, is taken into account for the comparison. It is compared with an enhanced ripple discharge, which has similar values of rotation and higher rotation gradient around the radial position ρ=0.25, as shown in figure 3.4a. Looking at the relative ion temperature profiles represented in figure 3.4b, the similar absolute value of the rotation does not lead to similar core ion temperature profiles if the rotation gradient changes between the shots.

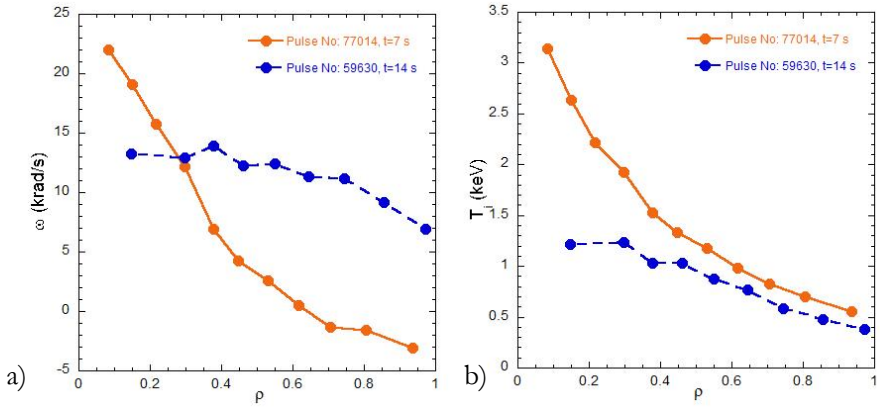

Fig. 3.4 Toroidal rotation profiles (a) and relative ion temperature profiles (b) of two analyzed shots. At ρ=0.25 the shot number 77007 (solid line) is characterized by a value of rotation similar to the one of the shot number 77017 (dashed line). The represented profiles are taken at the times indicated in the legend of the graphs.

Then from the comparison of experimental profiles of the shots the variation of ion temperature gradient seems due to changes of the rotation gradient rather than of the absolute value of rotation.

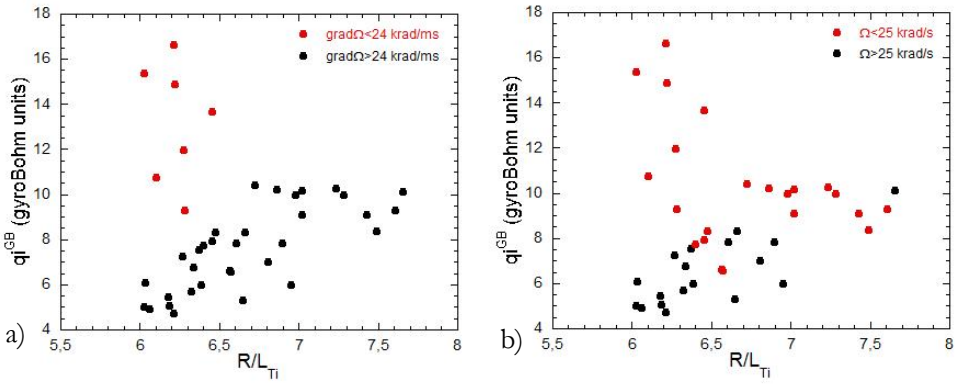

Fig. 3.5 Gyro-Bohm normalized ion heat flux q_i is shown as a function of the ion critical gradient length R/L_{Ti} at ρ=0.25. Points are grouped with respect to the values that the rotation gradient (a) and the rotation (b) of the relative shots reach in ρ=0.25.

Larger ion temperature gradients can be due to higher ion threshold values or to lower ion stiffness values. In order to clarify this point a second analysis has been done, taking into account the value of the ion heat flux of all the discharges. Although this point was already clarified in figure 2.13, a further confirmation was searched in this set of discharges. The ion heat fluxes at the radial position ρ=0.25 are plotted as functions of the logarithmic gradient of the ion temperature calculated at the same radius in figure 3.5. The ion heat flux is expressed using the gyro-Bohm normalization. The obtained points have been divided according to their values of rotation gradients at the radial position ρ=0.25. In particular circles (squares) represent pulses characterized by a rotation gradient less (more) than 24 krad/ms. We can see that the behaviour shown by the experimental results described in paragraph 2.3.4 of this thesis is confirmed. In that case we remember that rotation and rotation gradient were coupled. Here two net distinct curves form in dependence of the rotation gradient. The curve represented by circles determines a very stiff behaviour of the plasmas characterized by low rotation gradient. With growing ion heat flux ion temperature gradients do not increase significantly. Squares determine a curve with a slope that indicates a low level of stiffness for plasmas with high rotation gradient. We can note a strong increase of the ion temperature gradients with increasing ion heat fluxes.

The behaviour observed in figure 3.5a is only partially reproduced dividing points according to the rotation values rather than rotation gradient values. In figure 3.5b circles (squares) represent pulses characterized by a rotation less (more) than 25 krad/s. Several discharges are characterized by coupled rotation and rotation gradient, so the two curves of high and low stiffness form despite the distinction of the points on the basis of their rotation values. However, some of the points with low rotation values sit in the curve of low stiffness. These are the ripple enhanced discharges having high rotation gradient but low rotation value, which are represented by the green triangles in figure 3.6.

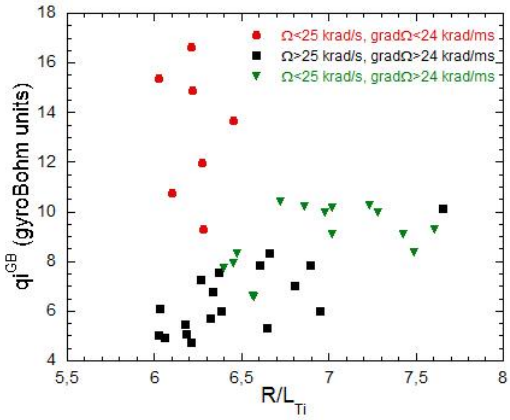

Fig. 3.6 Gyro-Bohm normalized ion heat flux q_i is shown as a function of the ion critical gradient length R/L_{Ti} at ρ=0.25. Graphs of fig 3.4a and 3.4b are here resumed. Points with decoupled rotation and rotation gradient are pointed out: they are indicated with reversed green triangles.

Then we can conclude that it is the rotation gradient that matters in reducing the ion stiffness level, and not the absolute value of rotation.

3.5 RF driven hollow rotation experiment

The analyzed discharges of the above described experiment and those shots belonging to the experiment reported in paragraph 2.3.4 are characterized by profiles of plasma toroidal rotation that are monotonic and peaked in the central part of the plasma, i. e. with negative rotation gradient. In order to understand if the sign of the rotation gradient can play a role in influencing the ion stiffness, and then the ion temperature profiles, discharges belonging to a different experiment have been analyzed. Several experimental observations on different machines have shown that in plasmas the toroidal rotation is sensitive to the ^{3}He concentration [81,82]. In particular ICRF mode conversion has been found to drive toroidal flow and in JET hollow rotation profiles have been observed, leading to suppose the existence of a torque in the opposite direction with respect to the plasma current one [83]. A selection of discharges that exhibit hollow rotation profiles in presence of (^{3}He)-D ICRH heating have been analyzed and compared with similar discharges in which the rotation profile was not hollow but flat.

3.5.1 Experimental set-up

The parameters of the discharges analyzed are reported in table 3.2. The heating is provided by the ICRH heating system, with a power strength equal to 7 MW. The power deposition has been varied from dominant electron in 3% (H)-D minority to dominant ion in 4-8% (^{3}He)-D to dominant electron in 20% (^{3}He)-D where mode conversion takes place. Other discharges characterized by the parameters of the table 3.2 but NBI heated

have been included in our analysis, in order to have high negative rotation gradient plasmas to compare with the positive ones obtained from hollow rotation profiles.

The power deposition and then the ion heat flux have been derived using the code PION.

Physical quantities have been measured and obtained as described in paragraph 3.4.2.

	Discharges parameters
I_p (MA)	1.8
B_T (T)	3.3
n_{e0} ($10^{19}m^{-3}$)	3.5
q_{95}	5
T_e/T_i	0.9-1.2

Table 3.2. Parameters of the analyzed discharge set with RF driven hollow rotation profiles.

3.5.2 Data analysis and experimental results

Some discharges of the experiment are found to exhibit a hollow rotation profile for a limited time interval, while a flat rotation characterizes these shots for the rest of the discharge. Comparing the ion temperature profiles corresponding to hollow rotation with those for which the rotation is flat, the role of rotation and rotation gradient can be investigated also for positive rotation gradient.

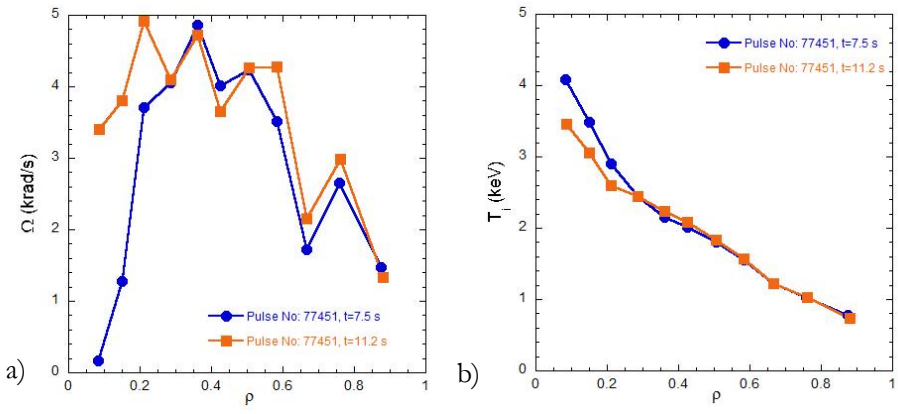

Fig. 3.7 Toroidal rotation profiles (a) and relative ion temperature profiles (b) of the shot 77451 at 7.5 s and 11.2 s. For $\rho<0.3$ the shot number 77451 at 7.5 s (line with circles) is characterized by hollow rotation, instead at 11.2 s (line with squares) the rotation is flat. In this region the T_i reaches higher values in the case with hollow rotation.

An example is reported in figure 3.7. Rotation profiles and corresponding T_i profiles of one pulse for two different times (and different ^{3}He concentration) are shown. The

rotation profile is hollow for $\rho<0.3$ at time equal to 7.5 s, with rotation values still in the co-IP direction. The rotation becomes flat at t=11.2 s. As shown in figure 3.7b, we find different T_i profiles in the plasma region within $\rho=0.3$. In this zone higher values of the T_i gradient are observed for the case of hollow rotation (where the rotation gradient is rather high and positive, even if the rotation value is lower with respect to the case of flat rotation). In order to compare properly the different shots, they have been plotted again in the qi_{gB} vs R/L_{Ti} plot in figure 3.8. Here circles, characterized by low rotation and rotation gradient, belong to high stiffness curve, triangles have medium rotation and rotation gradient and sit in the medium stiffness curve and squares, that are characterized by high rotation and gradient of rotation, form the low stiffness curve, consistently with the graph of figure 3.6. The points obtained from the profiles shown in figure 3.7 are circled. The one with flat rotation has a low value of rotation and of rotation gradient, so it is shown with a circular indicator. It is found to sit among circles and clearly belongs to high stiffness family. The point calculated at the time in which the rotation is hollow is represented by a reversed triangle and it is characterized by medium positive rotation gradient and low rotation. The normalized ion heat flux in the hollow rotation cases is comparable to that of other flat cases, whilst the ratio T_e/T_i is a bit higher in the case of hollow rotation, which should even decrease R/L_{Ti} in this case due to a threshold decrease (see eq. (2.67)). Instead, a systematic high value of R/L_{Ti} is seen in hollow cases, which we ascribe to reduced stiffness due to the rotation gradient. We can see that the points with medium rotation gradient belong to the medium stiffness curve independently of the sign of the gradient. It is then the absolute value of the rotation gradient that influences the ion stiffness level, no matter what sign it has.

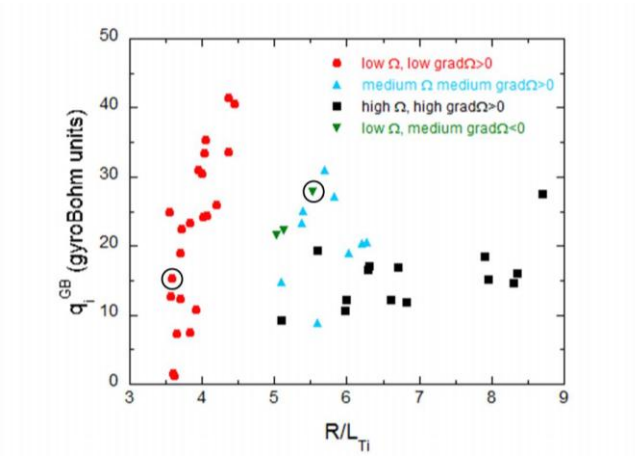

Fig. 3.8 Gyro-Bohm normalized ion heat flux q_i is shown as a function of the ion critical gradient length R/L_{Ti} at $\rho=0.25$. Points are grouped with respect to the values that the rotation and the rotation gradient of the relative shots reach in $\rho=0.25$.

3.6 Summary

Experiments are presented where the correlation between the absolute value of the rotation and its gradient has been broken by enhancing the B_T ripple, which has effect on the rotation, lowering its value, while it acts less strongly on the rotation gradient. The use of magnetic perturbations by EFCCs has instead led to lower values of both rotation and rotation gradient, that follow the same correlation trend of the shots with standard B_T ripple and without the application of EFCCs.

Comparing pairs of discharges characterized by similar rotation and different rotation gradient values and pairs of discharges with similar rotation gradient values and different rotation values, the observed behaviour of the ion temperature profiles indicates a dependence on the gradient of rotation rather than its value. Besides, from the analysis of all the shots of the experiment about the dependence of the ion heat flux on the normalized logarithmic gradient of ion temperature, net distinct curves of different ion stiffness have been found for different gradients of rotation, confirming the previous results reported in paragraph 2.3.4. If instead the discharges are grouped according to different values of rotation a mixed behaviour is seen. In particular, the discharges with decoupled low rotation and high rotation gradient sit well in the low stiffness curve. We can then conclude that the ion stiffness mitigation is due to the rotation gradient rather than the rotation value.

In addition, comparing discharges characterized by hollow rotation profiles with discharges with flat rotation profiles, the ion temperature profile peaking is observed to be higher in the case of hollow rotation, i. e. for a high positive rotation gradient, although the rotation value is lower than in the cases with flat rotation profile. Analyzing for these discharges the behaviour of the ion heat fluxes as functions of normalized logarithmic gradient of ion temperature, in relation with discharges with lower values of rotation gradient and similar values even if opposite (negative) sign, results indicate that the level of ion stiffness depends on the absolute value of the rotation gradient, independently of its sign.

Chapter 4

Numerical analysis of the impact of the ion threshold, ion stiffness and temperature pedestal on global confinement and fusion performance in JET and in ITER plasmas

In Chapter 3 the dependence of the ion stiffness reduction on the absolute value of plasma toroidal rotation gradient has been shown experimentally. However this result gives information about the role of the rotation on a local level. Because we are interested in the impact that the rotation has on the global performances of tokamaks, it is very important to find a link between local transport studies and the parameters that describe the global behavior of the plasma. To this scope a numerical work consisting in a series of transport simulations with scans of local quantities as ion threshold, ion stiffness and temperature pedestal height have been carried out, allowing to quantify the effect that these parameters separately have on the global performance. As global parameters we consider the global confinement and the equivalent fusion power. The first is more sensitive to the ion temperature of the plasma edge, the second depends mainly on the core ion temperature. The semi-empirical transport model CGM described in paragraph 2.2 of this thesis has been used: it depends explicitly on threshold and stiffness, allowing to vary them separately and quantify their effects. The CGM has been implemented in JETTO, a 1.5 D core transport code of the JET integrated code suite, shortly described in paragraph 4.1. JET discharges have been simulated using as basis of the simulations a reference discharge of the JET database characterized by the improved confinement regime "hybrid" (paragraph 1.3). The dependence of global parameters on the injected power has been investigated too. Paragraph 4.2 presents the characteristics and the dependences of the considered global confinement parameter. Simulations and results are reported in paragraph 4.3. The same numerical analysis has been carried out for ITER. The ITER machine is described in paragraph 4.4, together with the simulations and the results of the numerical work. The summary and conclusions follow in paragraph 4.5.

4.1 The JETTO code

JETTO [81] is a one-and-half-dimensional (1.5 D) transport code solving the time-dependent plasma transport equations averaged over the magnetic flux surfaces. Besides the transport solver, it includes an internal equilibrium solver and many packages, among which heating modules and several transport models, both empirical and theory-based. Transport equation are expressed as

$$\frac{1}{V'}\frac{\partial}{\partial t}\left(V' n_j\right) + \frac{1}{V'}\frac{\partial}{\partial \rho}\left(V' \langle(\nabla\rho)^2\rangle \Gamma_j\right) = \langle S_{n_j}\rangle \qquad j = 1, \dots, n_H \quad (n_H < 3) \tag{4.1}$$

$$\frac{3}{2}(V')^{-5/3}\frac{\partial}{\partial t}\left[(V')^{5/3} n_e T_e\right] + \frac{1}{V'}\frac{\partial}{\partial \rho}\left\{V' \langle(\nabla\rho)^2\rangle \left[q_e + \frac{5}{2} T_e \Gamma_e\right]\right\} = \langle P_e\rangle \tag{4.2}$$

$$\frac{3}{2}(V')^{-5/3}\frac{\partial}{\partial t}\left[(V')^{5/3} \sum_{j=1}^{n_H} n_j T_i\right] + \frac{1}{V'}\frac{\partial}{\partial \rho}\left\{V' \langle(\nabla\rho)^2\rangle \left[\sum_{j=1}^{n_H}\left(q_j + \frac{5}{2} T_i \Gamma_j\right)\right]\right\} = \langle P_i\rangle \tag{4.3}$$

$$\frac{1}{V'}\frac{\partial}{\partial t}\left(V' \sum_{j=1}^{n_H} n_j m_j \langle R^2\rangle \Omega\right) + \frac{1}{V'}\frac{\partial}{\partial \rho}\left[V' \sum_{j=1}^{n_H}\left(\langle R^2\rangle m_j \Omega \Gamma_j + \langle R^2\rangle \Pi^{\phi\rho}\right)\right] =$$

$$= \sum_{j=1}^{n_H} \langle R^2\rangle S_{M_j}^{\phi\rho} + \langle R^2\rangle S_{M_e}^{\phi\rho} \tag{4.4}$$

$$\frac{\partial \psi}{\partial t} - \frac{A\eta_{||}}{\rho\mu_0}\frac{\partial}{\partial \rho}\left(K\frac{\partial \psi}{\partial \rho}\right) + \frac{V'\eta_{||}}{2\pi\rho}(j_{bs} + j_{cd}) = 0, \tag{4.5}$$

where quasi-neutrality and equal temperature T_i for the n_H ion species (n_H is the number of all the ion species) are assumed. $\rho = \sqrt{\phi/\pi B_\phi}$ is the flux surface label, with ϕ the toroidal flux. ψ is the poloidal flux. V is the volume and V' means the differentiation with respect to ρ. <> denote the flux surface average. A and K are geometrical factors. μ_0 is the vacuum permeability. $\eta_{||}$ is the parallel electrical resistivity, given by the neoclassical expression [82]. $\Omega = V_t/R$ is the angular toroidal rotation. G_j, q_j and $\Pi^{\phi\rho}$ are the particle, heat and toroidal momentum fluxes. (for $\Pi^{\phi\rho}$ we adopt the following definition $\Pi^{\phi\varrho} = -\chi_M \frac{\partial \Omega}{\partial \rho}\langle|\nabla\rho|^2\rangle \sum_{j=1}^{n_H}(n_j m_j)$). S_{nj} is the source and sink term for particles due to atomic processes. P_e and P_i are heat sources and sinks due to auxiliary heating, energy exchange due to different species, charge exchange losses, radiation. S_{Mj} denotes momentum sources, such as neutral beam injection. j_{bs} is the bootstrap current, j_{cd} the externally driven current.

Transport models contributions enter the equations (4.1-4.5) through the terms G_j, q_j and $\Pi^{\phi\rho}$. Transport equations form a complex integro-differential system. An appropriate set of initial and boundary conditions is required to predict the time evolution of the simulated unknown quantities n_e, T_e, T_i, Ω, B_θ. The initial profiles of all the unknown quantities can be constructed either from the experimental data or from some prescribed formula, and they are read from an external file at the first time step. The boundary conditions are needed both in the centre and at the separatrix. In the centre the boundary condition takes the form $\partial u/\partial\rho = 0$ (where u is the unknown quantity to be modelled) for all the quantities. At the plasma edge experimental values are typically imposed in JETTO. The boundary condition for the poloidal magnetic field is determined by the

total plasma current. The value of Z_{eff} (the effective atomic number) is needed in the simulations and normally the experimentally measured value is used.

Several numerical modules are implemented in JETTO. The equilibrium is solved through the code ESCO, that takes the pressure and the current density profile as input from JETTO and then solves the Grad-Schluter-Shafranov equation in order to calculate the equilibrium and flux surfaces. The equilibrium can also be taken fixed by using EFIT [83], a code of equilibrium reconstruction which calculates the equilibrium and the flux surfaces starting from the experimental magnetic measurements. The equilibrium is always calculated at the beginning of the JETTO transport simulation and can be recalculated later during the transport calculation.

Amongst the other numerical models here we mention the heating packages. They are codes implemented and coupled with JETTO. The codes PION [72] for ICRH heating, PENCIL [73] and ASCOT [74] for NBI heating have been described in paragraph 3.4. The power deposition and current density profiles of the lower hybrid current drive system (LHCD) are calculated through the Fast Ray Tracing Code (FRTC) [84], that is coupled to JETTO. It includes a fast ray-tracing package and the calculation of the quasi-linear diffusion coefficient and a 1D Fokker-Planck equation for the electron distribution function.

Several transport models are implemented in JETTO. Among them we recall the semi-empirical models Bohm-gyroBohm [51] and Critical Gradient model [52,53] and the first principle models Weiland [44] and GLF23 [50]. They are all described in paragraph 2.2 of this thesis.

4.2 Global confinement

As shown in Chapters 1 and 2 of this thesis, processes that determine transport in tokamaks are very complex. The dependence of global energy confinement properties on plasma parameters as derived by first principle is not validated. The global energy confinement time is described by empirical scalings that are based on datasets coming from relevant operating regimes as L-mode or H-mode. Such scalings are widely used to predict the performances of next devices (as for example ITER) and also as a normalization for plasma energy in simulations carried out by transport codes as JETTO. In particular the confinement parameter H_{98} [85] is used in numerical predictions. It is defined as the ratio of the thermal energy confinement time τ_E and the experimental scaling of energy confinement time of H mode plasmas $\tau_{IPB98(y,2)}$. It depends on the physical quantities shown in the formula (4.6).

$$H_{98} = \frac{\tau_E}{\tau_{IPB\ 98(y,2)}} = \frac{W_{th}}{0.0562\, P^{0.31} I_P^{0.93} B_0^{0.15} n^{0.41} R_0^{1.97} \kappa_a^{0.78} (a_0/R_0)^{0.58} A^{0.19}} \qquad (4.6)$$

Here W_{th} is the total thermal energy, P the total power (given by the sum of the ohmic power, the injected power and the α power), I_P the plasma current, B_0 the magnetic field, n the density, A the average ion mass. The confinement parameter depends also on geometrical parameters: the major radius R_0, the minor radius a_0, the elongation κ_a

(defined as the ratio of the plasma volume and $2\pi^2 a_0^2 R_0$). Normally H_{98} is around one for H-mode plasmas, while for plasmas characterized by improved confinement it reaches higher values.

4.3 JET plasmas

A first series of simulations is carried out using as input parameters the physical quantities belonging to a hybrid discharge produced at JET. As reported in Chapter 2, recent studies show that in hybrid discharges a relevant improvement of the core confinement, that is interpreted as due to the variation of the ion stiffness, has been observed [29], in addition to the improvement of the confinement due to increased pedestal. For hybrid plasmas H_{98} is found to achieve values about 1.4 [86]. Our scans work aims not to obtain the typical hybrid plasma values of the confinement parameter (that depends for example on the shape of the electron temperature profile, which here is modeled only to be consistent with the resultant ion temperature profile), but rather to quantify the changes in H_{98} following variation of ion heat transport parameters.

It is reasonable to expect that the hybrid scenario is a regime in which the effect of the variation of the ion stiffness is more significant than in non-hybrid discharges because, following the interpretation of paragraph 2.3.4, hybrids are characterized by a broader region in which improved ion temperature profiles are observed. The impact of the ion stiffness variation is expected significant also with respect to the effects on the confinement variation due to changes of the ion threshold and the height of temperature pedestal.

In this context quantitative estimates of the impact that the variation of these parameters has on the global scale have been done through the simulation work described in the following.

4.3.1 Simulation set-up

Several simulations have been done in order to scan four significant parameters: the inverse ion temperature gradient length threshold, the ion stiffness, the height of temperature pedestal and the input power. For each scan only one parameter has been varied while we have kept all the other quantities unchanged. The JETTO code with the CGM as transport model has been used for this simulation work. This allows to put as input data, and then to vary separately all the scanned parameters. The plasma rotation has not been modelled and the stiffness level has been varied as a parameter, independently on the rotation. However the CGM is the only transport model which depends explicitly on the ion stiffness level, and for now transport models that predict correctly the effect of the rotation on the ion stiffness are missing.

Geometrical and physical parameters have been taken from the hybrid JET shot number 77043 as basis of the simulations. The characteristic parameters are shown in table 4.1.

	Hybrid JET plasma (shot number 77043)
I_p (MA)	1.7
B_T (T)	1.9
n_{e0} ($10^{19}m^{-3}$)	5.1
Z_{eff}	2.3
q_0	1.28
P_{ADD}(MW)	25.5

Table 4.1. Parameters of the experimental JET discharge 77043 used as input in the numerical simulations.

Beside the above indicated parameters, the input data taken from the JET database includes equilibrium configuration, geometry, density profile and the initial and boundary conditions for electron and ion temperatures, quantities that, together with the plasma current, are considered predictive in this numerical work, i.e. calculated solving ion and electron heat transport equations and current diffusion equation. NBI power deposition profiles have been taken from PENCIL code calculations, already described in paragraph 3.4 of this thesis. The neo-classical ion heat transport is calculated using NCLASS [87], a transport code inside JETTO. For the scans with fixed temperature pedestal height and/or power we started keeping the parameters typical of the JET hybrid plasma: 1.5 keV for the temperature pedestal and 25.5 MW of NBI power. Then we modified these parameters, reducing the height of the temperature pedestal to 1 keV or the power to 17 MW.

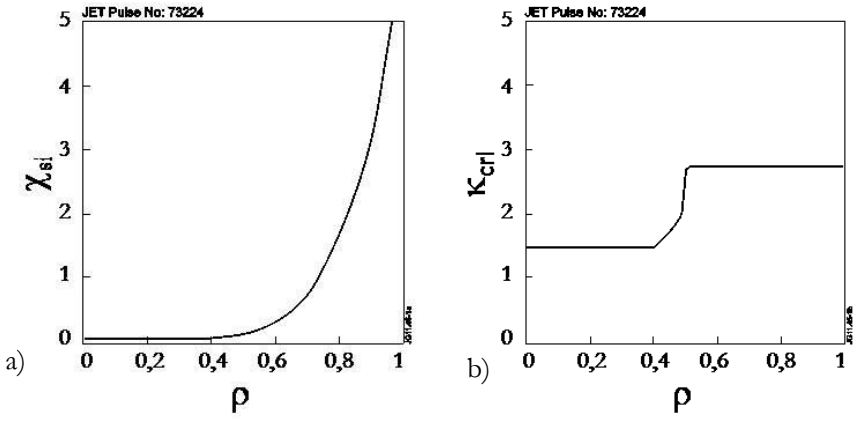

Fig. 4.1. Stiffness (a) and threshold (b) profiles as obtained by modulation experiments.

	ION STIFFNESS	**ION THRESHOLD**	**TEMPERATURE PEDESTAL**	**POWER**
SCAN of ION STIFFNESS	from 0.1 to 2	4	1.5 keV	25.5 MW
		4	1.5 keV	reduced, 17 MW
		4	reduced, 1 keV	25.5 MW
		profile	1.5 keV	25.5 MW
		profile	1.5 keV	reduced, 17 MW
		profile	reduced, 1 keV	25.5 MW
SCAN of ION THRESHOLD	0.4	from 3 to 12	1.5 keV	25.5 MW
	0.4		1.5 keV	reduced, 17 MW
	0.4		reduced, 1 keV	25.5 MW
	2		1.5 keV	25.5 MW
	2		1.5 keV	reduced, 17 MW
	2		reduced, 1 keV	25.5 MW
	profile		1.5 keV	25.5 MW
	profile		1.5 keV	reduced, 17 MW
	profile		reduced, 1 keV	25.5 MW
SCAN of TEMPERATURE PEDESTAL	0.4	4	from 0.1 to 3 keV	25.5 MW
	0.4	4		reduced, 17 MW
	2	4		25.5 MW
	2	4		reduced, 17 MW
	profile	profile		25.5 MW
	profile	profile		reduced, 17 MW
SCAN of POWER	0.1	7	1.5 keV	from 17 to 60 MW
	0.1	4	1.5 keV	
	0.1	7	reduced, 1 keV	
	2	7	1.5 keV	
	2	4	1.5 keV	
	2	7	reduced, 1 keV	

Table 4.2. Scans of ion stiffness, ion threshold, temperature pedestal and power for hybrid JET plasmas.

In scans with fixed ion stiffness and/or ion threshold we have chosen their values following the results obtained by recent heating power modulation experiments [28,57], which allow to distinguish the effects of stiffness and threshold, providing a direct measurement of them. In particular we have done simulations with ion stiffness and ion threshold constant over the radius, with ion threshold equal to 4, and considering values of both high and low ion stiffness in order to take into account the broad range it covers

in experiments. The modulation experiments analysis has led to determine ion stiffness and ion threshold radially varying profiles, which allow to achieve a better match with the experimental data with respect to stiffness and threshold radially uniform values. According to these results we have repeated the scans using the radially dependent profiles of ion stiffness and ion threshold shown in figure 4.1. In all the simulations presented in this paper, fixed values of threshold (equal to 5) and stiffness (equal to 1) have been taken for electrons following the recent results of perturbative experiments [54]. A list of the scans made is shown in table 4.1.

4.3.2 Simulation Results

4.3.2.1 Stiffness effect

First the scan of the ion temperature gradient stiffness is presented. In figure 4.2 we show an example of a scan of ion stiffness keeping fixed all the other parameters. In particular the case of typical hybrid plasma temperature pedestal height, equal to 1.5 keV, and power of 25.5 MW, with constant ion threshold equal to 4. Values of the normalized logarithmic gradient of ion temperature are shown in dependence of the ion stiffness level for different radial positions in figure 4.2a. All the values reached by R/L_{Ti} exceed the threshold ($(R/L_{Ti})_{cr}=4$). Then the stiff region (it is defined in paragraph 2.3) extends at least from $\rho=0.33$ to $\rho=0.73$, and the ion stiffness value influences a wide region of the ion temperature profiles, which are shown in figure 4.2b. The T_i value in the plasma centre varies significantly with increasing stiffness, from 7.6 keV to 5 keV. This behaviour is found similar in the simulations with other values of pedestal height, power and ion threshold.

The impact that ion stiffness has on the global scale is shown in figure 4.3, where the confinement parameter is presented as a function of the ion stiffness for different values of the power or/and the ion and electron temperature pedestal height. The following considerations can be done:

- as expected, the confinement parameter, and then the confinement, decreases with increasing ion stiffness independently of pedestal and power values. It is verified for a fixed ion threshold constant in radius (solid lines) and with radial profile (dashed lines), though in this last case the confinement parameter is slightly less sensitive to the stiffness changes;
- the variation of H_{98} with ion stiffness is found larger for the case of reduced temperature pedestal height and typical hybrid plasma power: changes from high stiffness to low stiffness increase the confinement parameter by 30% in the case of constant threshold equal to 4;
- reducing the pedestal height leads to lower temperature profiles, that however, for low ion stiffness, grow up to almost reach the profiles obtained for higher pedestal in the core region. For high stiffness the difference between the

temperature profiles keeps significant in both the edge and the core region. So in this last case we have an energy content very different for the high pedestal and the reduced pedestal simulations. H_{98}, which is directly proportional to the thermal energy, is then affected by this behaviour and decreases more in the case of reduced pedestal height;

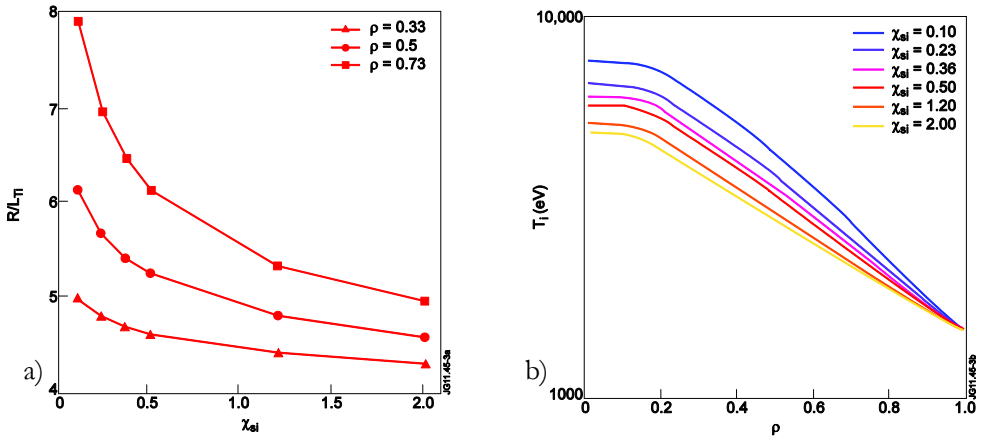

Figure 4.2.(a) R/L_{Ti} as a function of the stiffness level χ_{si} is shown for different values of the radial coordinate. It refers to the case of typical hybrid plasma power and temperature pedestal height, and threshold = 4. Triangular indicators are for ρ=0.33, circles for ρ=0.5, squares for ρ=0.73, where ρ is the normalized toroidal minor radial coordinate. (b) Correspondent ion temperature profiles on logarithmic scale; different colors are used for the different values that ion stiffness reaches in the scan.

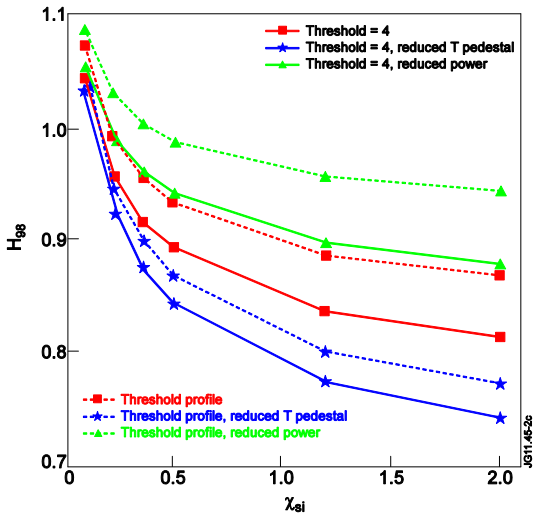

Fig. 4.3. Confinement parameter as a function of the ion stiffness level χ_{si}, for constant ion threshold (solid lines) and for the threshold profile presented in figure 4.1 (dashed lines). The simulations with typical hybrid plasma temperature pedestal and power are shown with red lines (for the case with solid line correspondent ion temperature profiles and R/L_{Ti} are represented in figure 4.2) those with reduced temperature pedestal with blue lines, and the case with reduced power is represented with green lines.

- in the case of reduced power we find the lowest variation of the confinement parameter. However H_{98} changes significantly also in this last case, by about 15%. Reducing the injected power causes the decrease of the temperature profiles with respect to the case of typical hybrid power, and then of the thermal energy, however the confinement parameter reaches higher values because it is also inversely proportional to the input power as the formula (4.1) shows. The difference between the temperature profiles obtained changing the power is found lower for higher ion stiffness and leads to similar values of the thermal energy. Then H_{98} varies less with the ion stiffness for the case of reduced power.

4.3.2.2 Threshold effect

The scan of the ion temperature gradient threshold is then presented. In figure 4.4 the effect of the threshold variation on R/L_{Ti} and on the ion temperature profiles is shown. It refers to the case of low constant stiffness, typical hybrid plasma temperature pedestal height (1.5 keV) and power (25.5 MW). In figure 4.4a we can see that R/L_{Ti} is not always higher than the chosen threshold of the scan, represented by the x-axis. In particular it occurs at inner radius for high values of ion threshold and is due to insufficient core power to keep the temperature above the threshold. Outside this region, the ion temperature profiles reach higher values for a higher ion threshold, as shown in figure 4.4b. The ion threshold growth leads to increasingly larger central region below threshold and dominated by neoclassical transport.

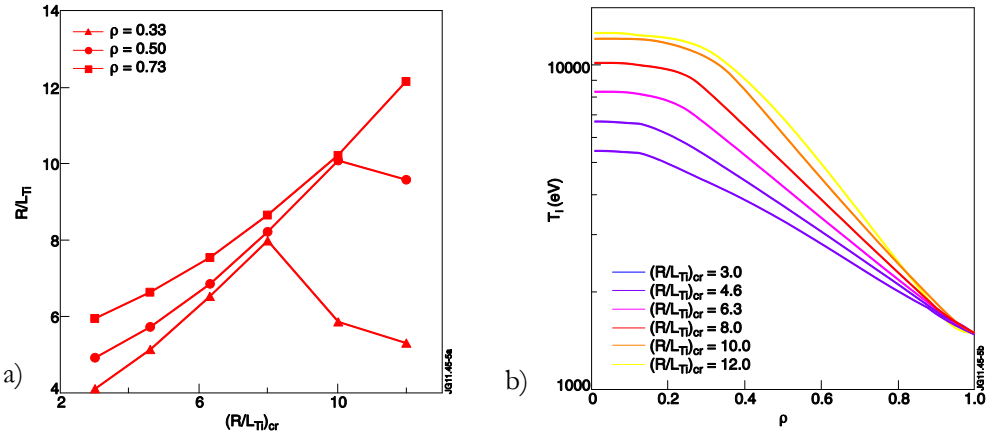

Fig. 4.4. (a) R/L_{Ti} as a function of the ion threshold $(R/L_{Ti})_{cr}$ is shown for different values of the radial coordinate. It refers to the case of stiffness = 0.4, typical hybrid plasma temperature pedestal height and power. Different curves in the graph refer to different radial positions. Triangular indicators are for ρ=0.33, circles for ρ=0.5, squares for ρ=0.73. (b) Correspondent ion temperature profiles are shown in logarithmic scale: different colors are used for the different values that ion threshold reaches in the scan.

The global analysis is reported in figure 4.5. The confinement parameter increases with increasing ion threshold, as expected. This takes place for all the values chosen for the

ion stiffness level (constant or dependent on the radial coordinate), and for every considered temperature pedestal height and power.

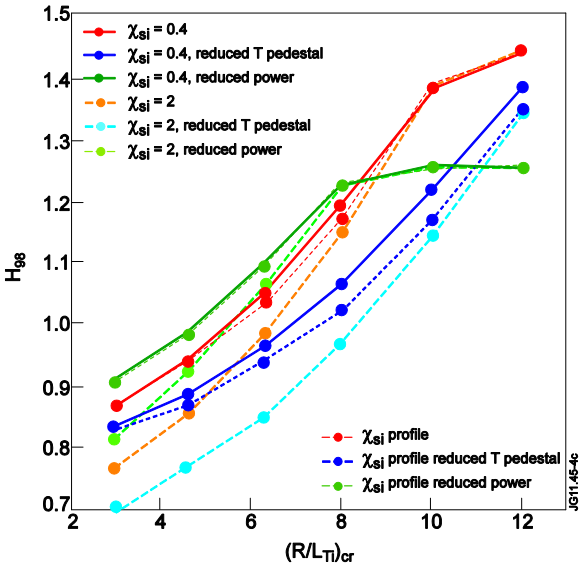

Fig. 4.5. Confinement parameter as a function of the ion threshold $(R/L_{Ti})_{cr}$ for low constant ion stiffness (solid lines), for high constant ion stiffness (dashed lines), for the stiffness profile represented in figure 4.1 (dotted lines). With red lines the case for typical hybrid plasma temperature pedestal and power is shown (for the case with solid line correspondent ion temperature profiles and R/L_{Ti} are represented in figure 4.4), with blue lines the case for reduced temperature pedestal, and with green lines the case for reduced power.

Increasing threshold makes a significant change in H_{98}. For high values of the ion threshold the growth of the confinement parameter tends to saturate in the case with hybrid plasma temperature pedestal height, especially for the scan with reduced power. This does not happen reducing the height of the temperature pedestal because lower ion temperature values are obtained, and, for ion thresholds until 12, the injected power seems to be sufficient to drive turbulent ion transport. For ion thresholds less than 7 the increase of H_{98} is larger for all the cases. We have to note, however, that from linear gyro-kinetic scans and considering the threshold up-shift effect due to rotation through the Waltz rule, the ion threshold is typically found to reach values not exceeding 7 in the usual range of parameters of the H-mode or hybrid plasmas. In this range the variation of H_{98} is up to 30% with high stiffness (dashed lines), and of about 20% in the other cases. Observing figure 4.4 for ion thresholds lower than 7, R/L_{Ti} is found higher than the threshold for all the considered radial positions. Its growing is higher for the inner radius. In the plasma centre the ion temperature varies from 5.4 keV for $(R/L_{Ti})_{cr}$=3 to 9 keV for$(R/L_{Ti})_{cr}$=7.

4.3.2.3 *Pedestal effect*

In the scan of temperature pedestal height both ion and electron temperature pedestal values have been varied. Looking at figure 4.6, where the case of low constant stiffness

(equal to 0.4), constant threshold (equal to 4) and typical hybrid plasma power (25.5 MW) is shown, the normalized logarithmic ion temperature profiles are above the threshold for every radial position, similarly to the case of the ion stiffness scan (figure 4.6a). The correspondent ion temperature profiles are represented in figure 4.6b. The central temperature changes from 4 keV for a pedestal of 100 eV to 9.8 keV for a pedestal of 3 keV.

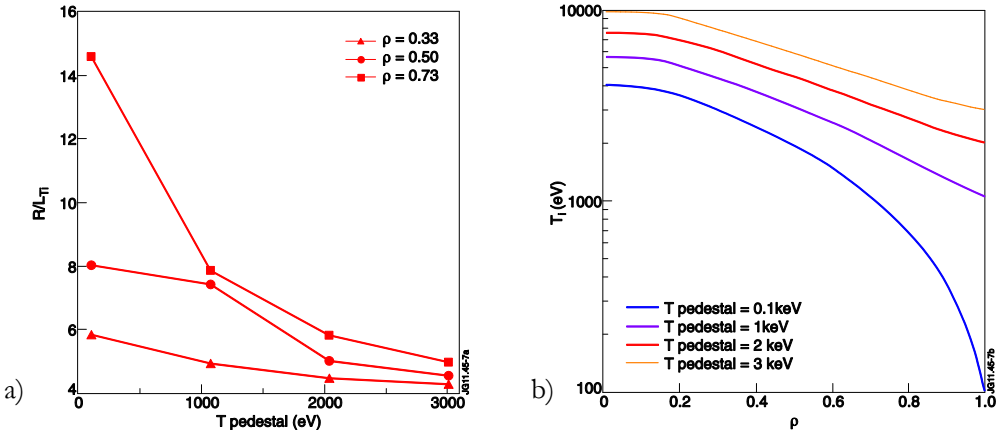

Fig. 4.6. (a) R/L_{Ti} as a function of the ion and electron temperature pedestal height is shown for different values of the radial coordinate. It refers to the case of constant threshold (equal to 4), hybrid plasma power and stiffness = 0.4. Different curves in the graph refer to different radial positions. Triangular indicators are for ρ=0.33, circles for ρ=0.5, squares for ρ=0.73. (b) Correspondent ion temperature profiles are shown in logarithmic scale: different colors are used for the different values that the T pedestal reaches in the scan.

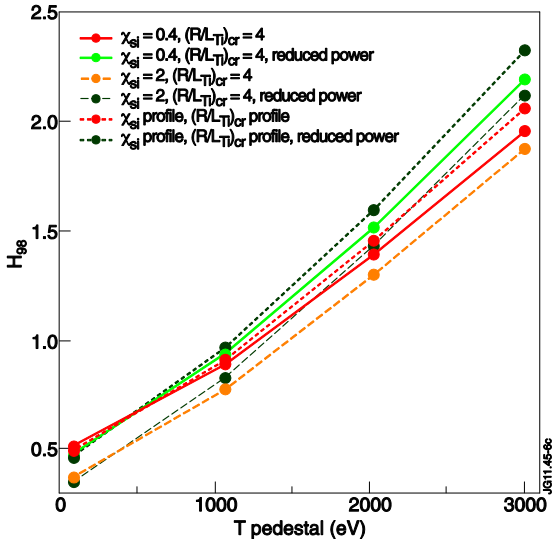

Fig. 4.7. Confinement parameter as a function of the ion and electron temperature pedestal height, for low constant ion stiffness and constant ion threshold (solid lines), for high constant ion stiffness and constant ion threshold (dashed lines), for the stiffness and threshold profiles represented in figure 4.1 (dotted lines). With red lines we have represented the case of typical hybrid plasma power(for the case with solid line correspondent ion temperature profiles and R/L_{Ti} are represented in figure 4.6), with the green ones the case of reduced power.

Results on the global scale are shown in figure 4.7. The confinement parameter increases with increasing temperature pedestal height: as expected it plays a very important role in increasing H_{98}. For reduced power (green lines) the increase of the confinement parameter is slightly higher. Choosing different values for the fixed threshold and stiffness does not lead to large changes: the case with stiffness and threshold profiles (dotted lines) gives slightly larger variation in the confinement parameter, which also assumes slightly higher values. We can state that H_{98} varies by about 80% changing the temperature pedestal from 0.1 keV to 3 keV.

4.3.2.4 Injected power effect

Finally the injected power scan results are reported, for which a substantially different behavior has been found for different ion stiffness values. In figure 4.8 ion temperature profiles with varying injected power are shown for high constant threshold and typical hybrid plasma temperature pedestal height. In figure 4.8a, where the stiffness is low, values from 9.2 keV to 17.1 keV are reached by the ion temperature in the centre of the plasma when varying the power. For high stiffness (figure 4.8b), the values vary from 8 keV to 10.6 keV, and only in the very centre, where transport is below the threshold.

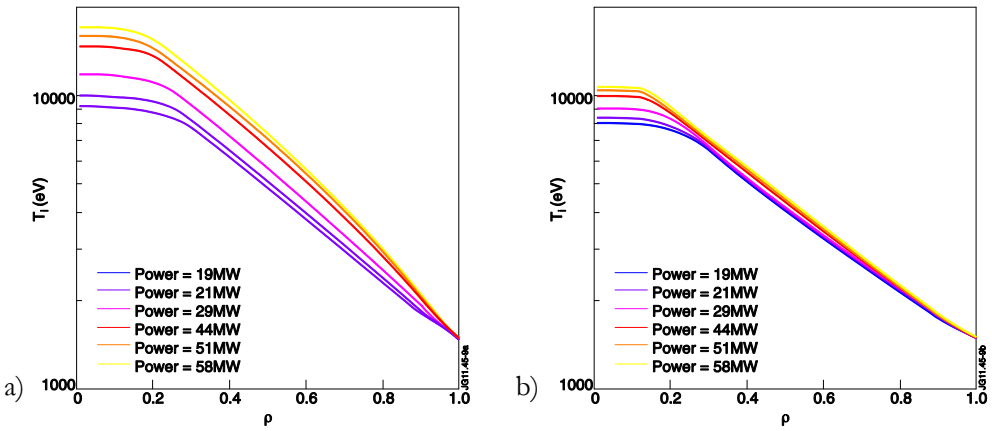

Fig. 4.8. Ion temperature profiles in logarithmic scale are shown, (a) for low constant stiffness (equal to 0.1), (b) for high constant stiffness (equal to 2); both the graphs refer to the case with high constant threshold (equal to 7) and typical hybrid plasma pedestal height (equal to 1.5 keV). Different colors are used for the different values that power reaches in the scan.

Results of the global analysis are shown in figure 4.9. For low stiffness (figure 4.9a) the confinement parameter does not depend on the power value. This holds for different fixed thresholds and temperature pedestal heights. Then the dependence on the injected power of energy confinement time for the hybrid JET plasmas characterized by low stiffness seems to be in good match with the behavior of the energy confinement time obtained from the experimental scaling for H-mode plasmas. In the case of high stiffness, H_{98} decreases with increasing power for a given set of temperature pedestal and threshold, as shown in figure 4.9b. Roughly 10% loss of H_{98} (coming from core

confinement) is predicted on typical JET power levels when going from 20 MW to 30 MW at high stiffness.

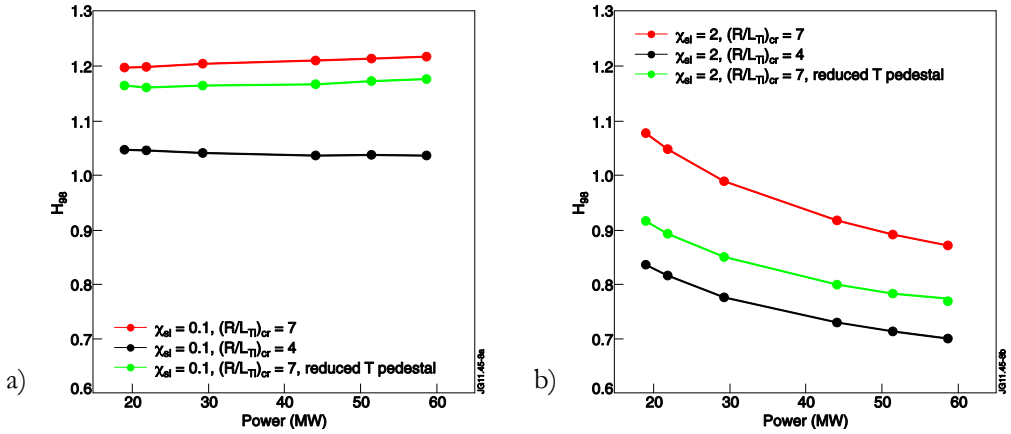

Fig. 4.9. Confinement parameter as a function of the power, (a) for low constant stiffness (equal to 0.1), (b) for high constant stiffness (equal to 2). With red lines we have represented the simulations with typical plasma hybrid temperature pedestal height and high constant threshold (equal to 7), with black lines the case of typical plasma hybrid temperature pedestal height and low constant threshold (equal to 4), and with green ones reduced pedestal height and high constant threshold (equal to 7).

4.4 ITER plasmas

The second series of scan simulations is based on the parameters that characterize the ITER machine. For ITER plasmas the impact of the variation of each scanned quantity on global plasma performance is studied through the behaviour of the confinement parameter and also of the fusion power obtained from the simulations. Fusion power is defined as the product between the reactivity of fusion reaction products (see Chapter 1, formula 1.3) and the energy released by the single reaction. The analysis of this parameter is included in the numerical study because what counts for a future reactor is to produce power from fusion reactions rather than to reach the best possible confinement. Before reporting scans results, a short description about the ITER project is given.

4.4.1 The International Thermonuclear Experimental Reactor project (ITER)

Although significant progress has been made with JET and other fusion experiments, it was clear from an early stage that a larger and more powerful device would be needed to create the conditions expected in a fusion reactor able to provide positive energy balance and to demonstrate its scientific and technical feasibility. ITER [88] will be a machine of the tokamak type that has, as the main aim, to demonstrate net prolonged power production through fusion reactions in a deuterium-tritium plasma. In order to produce more energy with respect to the one needed to heat the confined plasma for extended periods of time, ITER will be twice the size of the largest existing tokamak, JET, and

with greater expected fusion performance. These extrapolations in size and in physics performance provide the major challenges to the design of ITER.

Some of the main parameters of ITER are reported in table 4.3. ITER is designed to generate 500 MW of fusion power sustained for more than 400 seconds. A value of the fusion power gain Q>1 means that ITER should produce more power than it consumes. Q is defined as the amount of thermal power that is generated by the fusion reactions, divided by the amount of external heating power. JET in 1997 has reached Q=0.65 transiently and Q=0.24 in steady state conditions. ITER has to be able to produce Q=10 for hundreds of seconds, and Q larger than 5 during longer periods, possibly one hour or more.

ITER Parameters	
Major Radius	6.2 m
Minor Radius	2.0 m
Plasma Elongation	1.85
Toroidal Magnetic Field	5.3 T
Nominal Plasma Current	15 MA
Additional Heating Power	73 MW
Plasma Pulse Length	400 s
Average Electron Density	$1.1 \cdot 10^{20}$ m^{-3}
Average Ion Temperature	8.9 keV
Peak Fusion Power	500 MW
Fusion Power Gain (Q)	>10

Table 4.3. Main ITER parameters [86].

The inductive H-mode scenario has been chosen as the primary operating mode for ITER [88]. In the flattop phase the total current amounts to about 15 MA. The maximum toroidal field of 5.3 T is applied. The fully developed D-shaped plasma with X-point configuration is expected to have an elongation of $\kappa_{95}\sim1.7$ and a triangularity $\delta_{95}\sim0.33$ at the flux surface enclosing 95% of poloidal flux. The average electron density is $<n_e>\sim1.1\ 10^{20}$ m^{-3}. Full NBI power of 33 MW is applied to the plasma together with about 20 MW of radio frequency heating (ICRH). 400 MW of fusion power with $Q\simeq10$ and a flattop pulse length of 300-500 s are expected, according to the first simulations.

Compared with current conceptual designs for future fusion power plants, ITER will include most of the necessary technology (for example superconducting magnets and remote handling) that will then be possible to test, but will be of slightly smaller dimensions and will operate at about one-fifth of the power output level. However, similarly to future reactors, ITER will be characterized by the condition of burning plasma, which means that most of the heating from the plasma will come from the fusion reactions. Producing, studying and controlling this burning plasma is one of the most relevant scientific aims of ITER. Finally ITER should test and develop concepts for breeding tritium from lithium inside the blanket surrounding the plasma.

4.4.2 Simulation set-up

The parameters foreseen for the ITER baseline H-mode scenario are used as basis for the numerical simulations for ITER. Some of them are shown in table 4.3. The input power has been taken fixed: P_{NBI} = 33 MW, P_{ICRH}= 20 MW. PION and PENCIL, two codes described in the paragraph 3.4 of this thesis, have been used in order to calculate the ICRH and the NBI power deposition profiles respectively. Three parameters have been scanned: the ion stiffness, the ion threshold and the ion and electron temperature pedestal height. As in the case of hybrid JET plasmas, only one parameter varies for each scan, the others are kept fixed. When the temperature pedestal height is taken constant we have chosen the lower value of 3 keV or the higher value of 4 keV, following the estimates carried out for the ITER baseline scenario [89]. For fixed threshold and stiffness, values of the simulations of the JET hybrid discharge reported in the previous paragraph have been used. Making hypothesis about parameters as threshold and stiffness is challenging for a machine like ITER. Our investigation has taken into account the range of values that have been found in experimental studies carried out at JET, basing on the fact that threshold and stiffness are dimensionless parameters and refer to JET regimes similar to the ITER baseline scenario. A list of the scans made is shown in table 4.4.

	ION STIFFNESS	**ION THRESHOLD**	**TEMPERATURE PEDESTAL**
SCAN of ION STIFFNESS	from 0.1 to 2	4	3 keV
		4	4 keV
		profile	3 keV
		profile	4 keV
SCAN of ION THRESHOLD	0.4	from 3 to 12	3 keV
	0.4		4 keV
	2		3 keV
	2		4 keV
	profile		3 keV
	profile		4 keV
SCAN of TEMPERATURE PEDESTAL	0.4	4	from 2 to 6 keV
	2	4	
	profile	profile	

Table 4.4. Scans of ion stiffness, ion threshold and temperature pedestal for ITER plasmas.

4.4.3 Simulation Results

4.4.3.1 Stiffness effect

The scan of the ion stiffness, using different values of ion and electron temperature pedestal height and different ion thresholds, is first illustrated. Figure 4.10 refers to the case of ion threshold equal to 4 and temperature pedestal height of 3 keV. Looking at figure 4.10b, the large growth of the ion temperatures with decreasing ion stiffness is evident. This leads from T_{i0}=14 keV for χ_{si}=2 to T_{i0}=27 keV for χ_{si}=0.1. It is due to a significant increase of the gradient of T_i in the external part of the core as in the case of JET hybrid discharge, but also to its larger growth in the core and in the central region of the plasma. While in JET R/L_{Ti} is under the ion threshold values in the very central region, in the ITER case we find R/L_{Ti} quite over it. This can be explained by the use of the on-axis ICRH system in ITER, which is characterized by a deposition power maximum in the centre of the plasma. It is scheduled in ITER together with the NBI system that is expected to give a more radially distributed deposition power. The cases with other temperature pedestal height and ion threshold show a similar T_i and R/L_{Ti} development to the one represented in figure 4.10.

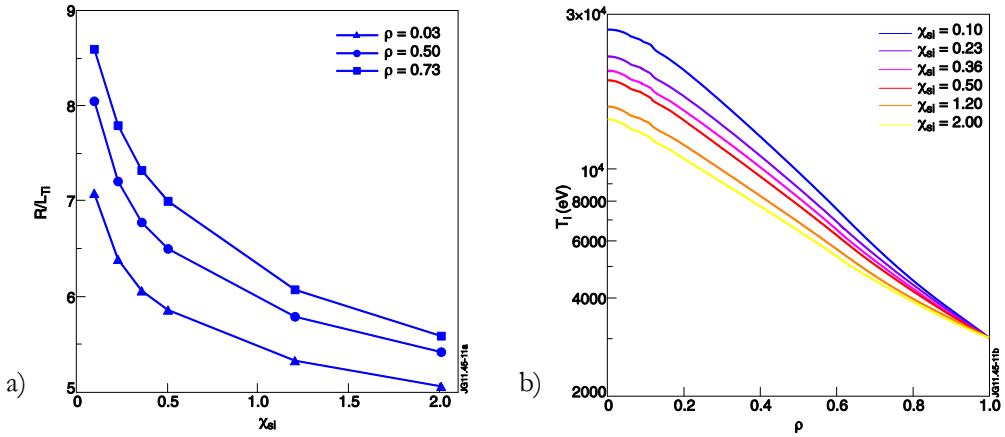

Fig. 4.10. (a) R/L_{Ti} as a function of the ion stiffness is shown for different values of the radial coordinate. It refers to the case of constant threshold (equal to 4), power and temperature pedestal height = 3 keV. Different curves in the graph refer to different radial positions. Triangular indicators are for ρ=0.33, circles for ρ=0.5, squares for ρ=0.73.(b) Correspondent ion temperature profiles are shown in logarithmic scale: different colors are used for the different values that the ion stiffness reaches in the scan.

The influence that ion stiffness variations have on global parameters is shown in figure 4.11. H_{98}, shown in figure 4.11a as a function of the ion stiffness, has the same behaviour as in the JET hybrid plasmas, but it is less sensitive to stiffness in ITER than in JET. In fact in this case the difference caused by changes in the stiffness is less than 10%. This is true also with a constant fixed value of the ion threshold and the variation is even lower with threshold profile. For the temperature pedestal height equal to 3 keV (blue lines) we find a confinement parameter more sensitive to stiffness changes, though with a lower

value with respect to the case with higher pedestal. In figure 4.11b the fusion power as a function of the ion stiffness is shown. We note that changes in stiffness cause an important variation of the fusion power, by over 50% of the total value. The drastic increase of the fusion power caused by the low stiffness can be explained by the large variation of the ion temperatures with the ion stiffness shown in figure 4.10b and their R/L_{Ti} values of figure 4.10a. As explained above, the ICRH gives an important contribution to the increase of the ion temperatures, and then to the magnitude of the fusion power.

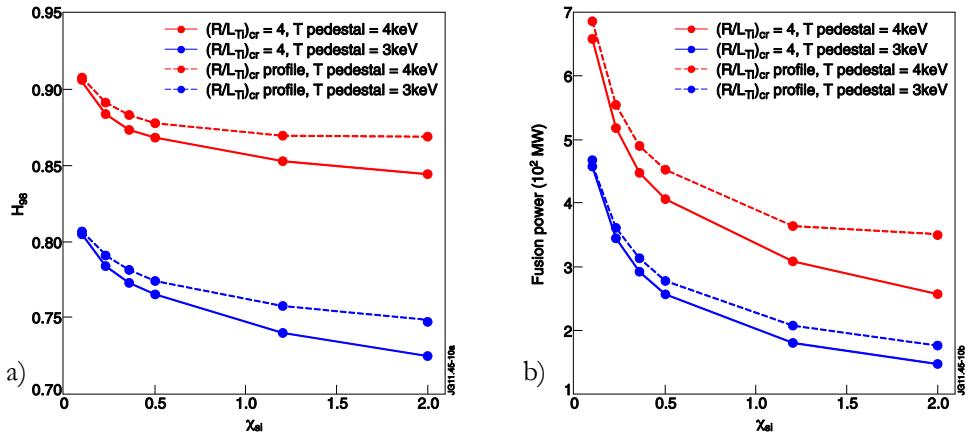

Fig. 4.11. Confinement parameter (a) and fusion power (b) shown as functions of the stiffness level χ_{si}. With blue lines we indicate the case with pedestal height equal to 3 keV (for the case with solid line correspondent ion temperature profiles and R/L_{Ti} are represented in figure 4.10), with red lines the case with pedestal height equal to 4 keV. Solid lines are used for constant threshold (equal to 4), dashed lines for the threshold profile shown in figure 4.1.

The different sensitivity of the confinement parameter between JET and ITER is due to the inclusion of the α power in the total power (that includes also ohmic power and heating power), on which H_{98} depends as shown in the formula (4.1). In fact, as we can see also from the large variation of the fusion power represented in figure 4.11b, the α power contributes significantly to the total value of the power. For lower ion stiffness the ion temperature achieves higher values, then the confinement parameter increases because it is directly proportional to the thermal energy. However, also the α power is larger and it causes a reduction of the H_{98} with respect to the case of JET hybrid plasmas, in which the α power is always equal to zero. This behaviour takes place for all the scans performed for ITER, where nuclear fusion reactions have been enabled.

4.4.3.2 Threshold effect

The ion temperature gradient threshold scan is then presented. In figure 4.12a we can see the confinement parameter as a function of the ion threshold for different values of ion stiffness and temperature pedestal. As for the scan of ion stiffness, the variation of H_{98} is much lower with respect to the JET case whilst the behavior is similar. Under the ion

threshold value of 7 the confinement parameter increases with increasing threshold up to about 10%, and its growth is larger (11%) in the case of high ion stiffness (dashed lines).

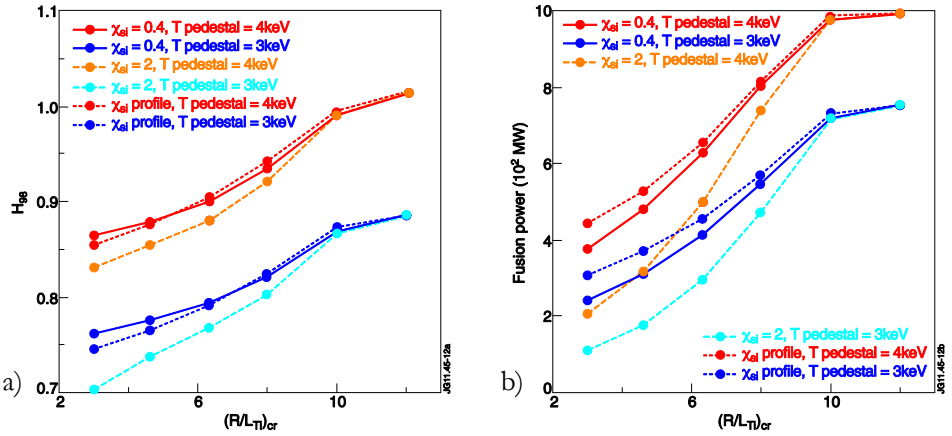

Fig. 4.12. Confinement parameter (a) and fusion power (b) shown as functions of the ion threshold. With hot (cold) colors we indicate the case with pedestal equal to 4 keV (3 keV). Solid lines are for low constant stiffness, dashed lines for high constant stiffness, dotted lines for the stiffness profile represented in figure 4.1.

For values of the ion threshold higher than 7 the increase of H_{98} is lower. As for JET hybrid simulations it corresponds to the R/L_{Ti} under threshold, that in the ITER case takes place in the outer region of the plasma, while in the centre it does not happen because of the ICRH power. The variation of the fusion power is larger for high constant ion stiffness, as figure 4.12b shows: the impact of the ion threshold on the fusion power is considerable and it gives a variation of over 50%. Besides, if the temperature pedestal height is equal to 4 keV the value of the fusion power is higher by almost 100 MW. It is a significant variation, however comparable with the difference of the fusion power due to using different ion stiffness levels.

4.4.3.3 Pedestal effect

Finally in figure 4.13a we can see the confinement parameter as a function of the temperature pedestal height. Also in this scan the increase of H_{98} has the same behaviour as in the case of the JET shot. The results shown in figure 4.13 agree with the previous scans about the role of the temperature pedestal height on ITER fusion power and confinement [90,91]. H_{98} grows more than 30% with increasing temperature pedestal from 2 keV to 6 keV, achieving a variation of 40% for high stiffness. In figure 4.13b the huge growth of the fusion power with increasing pedestal height is shown. Over 80% of increase and values of fusion power almost of 1000 MW are obtained for stiffness and threshold dependent on radial coordinate. Using different ion stiffness levels leads to fusion power values that differ by about 100 MW.

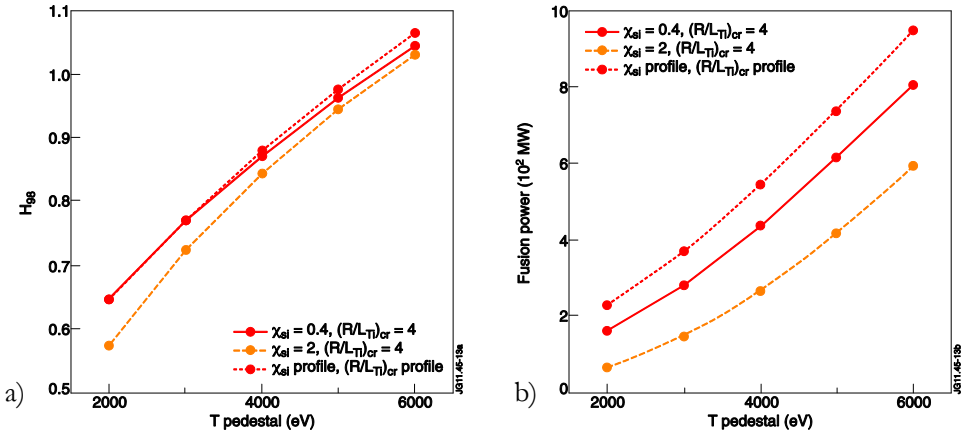

Fig. 4.13. The confinement parameter (a) and the fusion power (b) are shown as functions of the ion and electron temperature pedestal height. With solid lines we indicate the case with low constant ion stiffness (equal to 0.4) and constant ion threshold (equal to 4), with dashed lines we have used high constant ion stiffness (equal to 2) and constant ion threshold (equal to 4). With dotted lines the case of ion stiffness and ion threshold profiles (represented in figure 4.1) is shown.

4.5 Summary

Series of scans of ion stiffness, inverse ion temperature gradient length threshold, temperature pedestal height and injected power have been performed to study quantitatively their impact on global plasma performance, confinement and fusion power. The fluid transport code JETTO has been used together with the semi-empirical transport model CGM, which includes explicitly the control parameters of turbulent transport. It has been then possible to obtain a quantitative estimate of the impact of the local transport parameters on the core plasma transport and globally on the plasma.

First, hybrid JET plasmas have been used as basis of the simulations. The results show that changes up to 30% in the confinement parameter H_{98} and thereby in the plasma confinement can be achieved by changing the ion stiffness from very low values (χ_{si}=0.1) to high values (χ_{si}=2). Variations between 20% and 30% have been obtained from the scan of the ion threshold. Changes of over 50% in the H_{98} have been found by changing temperature pedestal height. This numerical work has then pointed out that the dependence of the global plasma performance on the ion stiffness is quantitatively significant, also in relation with the global effects due to the ion threshold and the temperature pedestal height, considering the variation of the three scanned parameters within a realistic interval of values defined by previous experimental studies. The relevance of the ion stiffness variation can partly explain the confinement improvement characteristic of JET hybrid plasmas, that are thought to be characterized by a larger region of low stiffness with respect to the standard H-mode plasmas. In addition we have seen that in the case of low stiffness, for a given choice of threshold and pedestal height, the energy confinement time in the JET hybrid scenario plasmas seems to depend on the injected power exactly as the energy confinement time obtained from the H-mode scaling law reported in the formula 4.6. This does not happen if the ion stiffness is high. In this

case the confinement parameter decreases with increasing input power. The power dependence of the H_{98} scaling then seems not to describe high stiffness plasmas adequately.

The scans have then been extended to ITER plasmas. The confinement parameter has been found to be less sensitive to the ion stiffness and ion threshold variations than for JET hybrid plasmas. However, looking at the fusion power changes, the effect of the variation of these parameters is very relevant. The scan of the ion and electron pedestal height gives large changes in the confinement parameter also for ITER plasmas, and a huge variation of the fusion power. The lesser sensitivity of H_{98} to the ion stiffness and threshold variation is due to the inclusion of the α power in the total power, that leads to a partial compensation of the changes of thermal energy, because the α power increases with growing thermal energy.

Understanding the magnitude and trends of all the three parameters is then relevant for the operations of the future fusion devices, influencing crucially their core ion temperature and then the achievable fusion power. Therefore, when predicting the performance of future machines as ITER, it is very important to know the ion stiffness level of their plasma, beyond the ion threshold and the temperature pedestal values, while in the present model validation efforts stiffness is rarely taken into account.

Chapter 5

Physics based modelling of H-mode and Advanced Tokamak scenarios for FAST: analysis of the role of rotation in predicting core transport in future machines

In the conclusions of Chapter 4 the relevance that the ion stiffness level has on the global performance of tokamak machines is pointed out. We know this parameter depends on several physical and geometrical quantities of the plasma, among which the influence of the plasma toroidal rotation gradient has been shown experimentally ([30] and paragraph 2.3.4) and confirmed in Chapter 3 of this thesis. Different scenarios, and then different kind and intensities of the additional heating can lead to different rotation values, and then to variations of the ion stiffness level. In particular, the toroidal rotation seems to be an essential ingredient to achieve advanced scenarios, characterized by improved core confinement, as reported in [29] and in paragraph 2.3.4. When tokamak scenarios are predicted, it is then important to take into account the ion stiffness level and its dependence on the toroidal rotation. Such effect is not included in first principle models available at the time of this thesis work, therefore the critical gradient model (CGM) (which features an adjustable stiffness level) has been used when reasonable extrapolations from JET were possible. In cases in which this was not possible, the Bohm-gyroBohm transport model has been used. This has been preferred to theory-based models such as GLF23 or Weiland, which have been shown not to feature the effects of high rotation and low magnetic shear on ion stiffness discovered on JET. The Bohm-gyroBohm instead is semi-empirical and calibrated on experimental data, and in fact includes a beneficial effect of high rotation and low magnetic shear as described in [92] and reported in Chapter 2, eq. 2.86, although the model is not cast in terms of stiffness.

This Chapter reports the core transport modelling work carried out in order to predict the operational scenarios for the FAST (Fusion Advanced Studies Torus) machine, including the plasma rotation in the simulations and analyzing its role in the considered scenarios. FAST is a device proposed as a possible European ITER satellite.

In paragraph 5.1 a short description of the machine together with the foreseen heating systems and the possible scenarios of operations and the investigated ones are presented. Paragraph 5.2 reports the simulations set-up. Simulations have been carried out with the

awareness that predicting performance and scenarios in future fusion devices beyond the level of 0D scaling laws is a challenging task. On one hand we do not yet have at disposal fully validated core and edge predictive transport models, on the other hand, assuming 1D profile conservation starting from data in existing machines and using dimensionless parameter scaling is at least partially hindered by expected differences between present and future machines, such as in plasma rotation, amount of electron heating and impurity concentrations. In this situation, the predictive activity has to wisely combine both theory based simulations and empirically based considerations, with the strongest possible link to experimental results in existing devices. The results of the scenarios predictive modelling are described in paragraphs 5.3, 5.4 and 5.5. Summary and conclusion are finally reported in paragraph 5.5.

5.1 Fusion Advanced Study Torus (FAST) proposal

The fusion advanced study torus FAST is a new machine proposed to support the ITER experimental exploitation [93,94]. The need of a physics and technology accompanying program for ITER, including one or more satellite tokamak experiments, is widely admitted. FAST is aimed at integrated investigations of fast particle physics, plasma operations and plasma wall interaction in burning plasma relevant conditions. It is meant to work with deuterium plasmas and to use fast ions, accelerated by heating systems (in the energy range of 0.5-1 MeV), in order to investigate the non linear dynamics relevant for the understanding of α particle behavior in burning plasmas. Then the particle confinement, both thermal and supra-thermal, which is determined by their orbit size normalized to the plasma minor radius, has to be similar to that of ITER, and this condition determines the values that must be reached by the plasma current I_p.

The parameters that characterize FAST are in a dimensionless range as close as possible to that of ITER, in order to explore the most severe ITER operational issues. In particular the ratio between electron-ion equipartition time and energy confinement time τ_{e-i}/τ_E is similar. This condition leads to have equal electron and ion temperatures, and to a similar ratio of fast ion collisional slowing down time to energy confinement time (τ_{SD}/τ_E), then to a similar ratio even between the fast ion β_H (H stands for 'hot') and the thermal plasma β, because $\beta_H/\beta \approx \tau_{SD}/\tau_E$ (it applies if the largest fraction of heating is provided by fast ions, that is under reactor relevant conditions but also in the FAST H-mode reference scenarios). In FAST the ITER geometry is reproduced.

Besides inductive H-mode scenarios, advanced regimes with long pulse duration with respect to the current diffusion time and up to full non-inductive current driven (NICD) scenarios are foreseen as FAST scenarios.

In addition technical innovative solutions for the divertor directly relevant for ITER are foreseen to be tested and, through a high ratio between the total available power from auxiliary heating systems and the system size, conditions of large heat loads on divertor plasmas can be reproduced. FAST is planned to be equipped with a large number of diagnostics similar to those of ITER.

Finally numerical benchmarks of codes and models together with the model verification and validation in ITER relevant plasma conditions can be carried out.

5.1.1 FAST heating systems

Three auxiliary radiofrequency heating systems have been foreseen for FAST. It will be equipped with ICRH as main heating scheme, with the aim of addressing several important burning plasma issues, as fast ion transport due to collective mode excitations and cross-scale couplings of micro-turbulence with meso-scale fluctuations due to the energetic particles themselves. They can be investigated by experimental studies of the fast ion tail produced by ICRH. The mechanism at the basis of ICRH is described in Chapter 3 of this thesis. In FAST up to 30 MW of power in the 30-90 MHz frequency range will be coupled.

The second foreseen heating system is the lower hybrid (LH) heating. The lower hybrid resonance heating uses waves at frequencies $\omega_{ci}<<\omega<<\omega_{ce}$, where $\omega_{ce}=eB/m_ec$ is the electron cyclotron frequency. One of the most fundamental properties of this heating system is the existence of a critical value of the parallel refractive index $n_{||}$, defined as the ratio between the vacuum wavelength and the wavelength parallel to the magnetic field in the plasma, below which the wave has two evanescence regions, one in the plasma edge, similarly to the fast wave of the ICRH system, the second is more internal and prevents the wave from penetrating into the internal plasma. In the above described frequency range and for a refractive index which respects the accessibility condition two waves can propagate, the fast and the slow modes. Originally the LH heating was conceived with the scope of heating the ions by launching the slow wave at a frequency below the LH resonance. This wave then propagates up to the LH resonance and is absorbed there. However experiments have shown the wave tends to be absorbed by electron Landau damping before having reached the resonance, the location of which is not completely controlled. Now the frequency is chosen above the central LH frequency, then all the power goes to electrons. The slow wave, which propagates parallel to the magnetic field, can accelerate the electrons in one direction if the wave launch spectrum is asymmetric, producing a current. The main application of LH is non-inductive current drive: today it is the best, experimentally proven, current drive method. FAST foresees 6 MW of LH at the frequency of 3.7 or 5 GHz.

Among the RF systems for FAST, the electron cyclotron radio-frequency heating (ECRH) is also included. For the electron cyclotron heating scheme, frequencies of the order of the electron cyclotron frequency $\omega=\omega_{ce}$ are required. High power microwaves have the required frequencies. Only the electrons respond to these waves and only the electrons are heated directly by absorbing resonantly the energy of the waves. However, under certain conditions, the ions are heated by the electrons through collisions. The absorption process of the electron cyclotron resonance is similar to the ion cyclotron case, even if for electrons relativistic effects are important. This is true even at temperatures at which the thermal velocity would not normally be thought of as being in the relativistic

regime. The ECRH system has several advantages, among which the main ones are a very localized heating, due to the fact that the absorption is quite narrowly localized around the cyclotron resonance layer. It may be used to control the current profile, with a view to suppressing MHD instabilities. In addition problems of impurities due to sophisticated coupling scheme structures required for the ICRH and LH schemes are absent in the case of electron cyclotron waves. They in fact are not evanescent in the vacuum, then launching systems can be put relatively far from the plasma, reducing the possibility of interaction with the plasma and the consequent impurities introduction. In FAST ECRH is planned to be used at the frequency of 170 GHz for central heating. It is foreseen to be used also at half radius for MHD control.

The FAST load assembly has been conceived to accommodate 10 MW of Negative Neutral Beam Injection (NNBI), allowing to produce fast particle populations with different anisotropy and profile localization, and to provide momentum input and current drive. NNBI is based on the processes described in Chapter 3 of this thesis.

5.1.2 FAST operational scenarios

For all the foreseen scenarios [95], FAST plasma equilibria have been designed to be, as much as possible, similar to that of ITER (see figure 5.1). All the experimental scenarios are planned to have the same plasma shape with major radius R=1.82 m and minor radius a=0.64 m, elongation κ=1.7 and triangularity $<\delta>$=0.4. The FAST scenarios investigated in this thesis work are shown in table 5.1. Two H-mode scenarios are presented. The reference H-mode, shown in the first column of table 5.1, is planned to have a duration of the high performance phase longer than the resistive diffusion time. This scenario is called reference because it is finalized to achieve all the main FAST physics goals in a unique integrated scenario. It is characterized by B_t=7.5 T and I_p=6.5 MA. 30 MW of ICRH at 73 MHz in (^{3}He)-D minority scheme is assumed as additional heating. Alternatively using B_t=6 T and I_p=5.5 MA, 15 MW of ICRH at 58 MHz in (^{3}He)-D minority and 15 MW of ECRH (170 GHz, 1st Harmonic O-mode from LFS) are the additional powers proposed, as illustrated in the second column of table 5.1. The last column of table 5.1 shows one of the proposals for the advanced scenarios studies in FAST. It refers to a full non inductive current drive scenario, where the plasma current is provided for the 60-70% by the bootstrap current and for the 30-40% by the LH driven current. B_t=3.5 T and I_p=2 MA are the parameters chosen for this scenario. A toroidal field lower than that of H-mode allows to achieve longer discharge duration. The heating power is 30 MW, provided fully by the ICRH system at 35 MHz in (^{3}He)-D minority, plus 4 MW provided by the LH at 5 GHz, $n_{||}$=2.3.

FAST	H-mode reference	H-mode (ECRH)	AT Full NICD
I_p (MA)	6.5	5.5	2
q_{95}	3.2	2.9	5
B_T (T)	7.5	6	3.5
$<n_{20}>$ (m^{-3})	2.2	2.2	0.9
P_{th_H} (MW)	14 ÷18	14 ÷ 18	5 ÷ 7
β_N	1.3	1.4	3.4
τ_E (s)	0.37	0.38	0.18
τ_{res} (s)	5.5	5	2 ÷ 5
T_0 (keV)	12.5	11.3	21.0
$t_{discharge}$ (s)	20	26	170
$t_{flat\text{-}top}$ (s)	13	17	160
I_{NI}/I_p (%)	11	16	170
P_{ADD}(MW)	30	15+15	30+4

Table 5.1. H-mode and AT scenarios for FAST

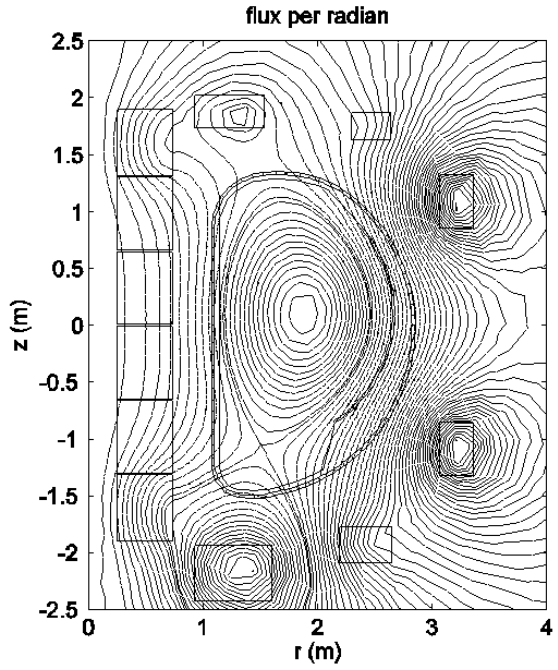

Fig. 5.1. FAST equilibrium [91].

The effect of replacing 10 MW of ICRH power with 10 MW of NNBI power (with beam energy of 700 keV) in the H-mode reference scenario and in the AT scenario is investigated. The injection of neutral beams is known to give rise to plasma rotation, that can lead to improved confinement and then improved plasma performances, as discussed in Chapter 2, and also observed experimentally and described in Chapter 3 of this thesis.

5.2 Simulations set-up

The simulations have been carried out using the JETTO code. The input quantities and the considered effects are listed in the following. Some of them (the magnetic equilibrium boundary, the ECRH deposition profiles, the pedestal values) are the results of a separate work carried out in parallel and are simply inserted in the transport code JETTO.

Magnetic equilibrium boundary: it has been produced by the full free boundary plasma equilibrium FIXFREE code [96,97] in the standard EQDSK format (including the chosen functional form of the kinetic plasma pressure and the diamagnetic total plasma current). We used a slightly peaked current density profile as initial guess. A boundary file with the last closed surface derived from FIXFREE calculations [98] has been inserted as input in JETTO, and then the fixed boundary Grad-Shafranov solver ESCO has been applied for the self-consistent evolution of the plasma equilibrium.In order to take into account the contribution of the fast particles to the total plasma pressure, a fixed multiplier 1.2 has been applied to the thermal pressure within ESCO.

Power deposition profiles: for ICRH heating profiles we have either used the PION code called self-consistently by JETTO or the TORIC [99] code which is run outside JETTO and then used as input for JETTO (this procedure requires a few iterations between JETTO and TORIC). The full-wave code TORIC solves the Maxwell-Vlasov integro-differential wave equations in the ion cyclotron range of frequencies (ICRF) in 2D axisymmetric equilibria. It is used in connection with the SSQLFP code [100], which solves the quasi-linear Fokker-Planck equation in 2D velocity space. Power deposition profiles of the ion minority, majority and electrons are determined first. Then, the effective temperature of the minority ion tail and the fraction of fast ions are evaluated consistently. Moreover, quasi-linear analyses determine how the power absorbed by the minority tail is redistributed by collisions among the main thermal plasma particles, majority ions and electrons.

Good match between the RF deposition predicted by TORIC and PION is obtained as shown in figure 5.2 for the case with n_{3He}/n_e=3%.

The ECRH heating profiles have been provided by the GRAY code [101], which is also outside the JAMS suite and required iterations with JETTO. For AT scenarios FRTC [102], within the JAMS suite, has been used to calculate LH heating and current drive profiles.

The NNBI power and torque profiles have been computed using the orbit following ASCOT code called self-consistently by JETTO. The ASCOT NBI deposition for FAST

device has been compared with the deposition predicted by the NEMO/SPOT code [103].

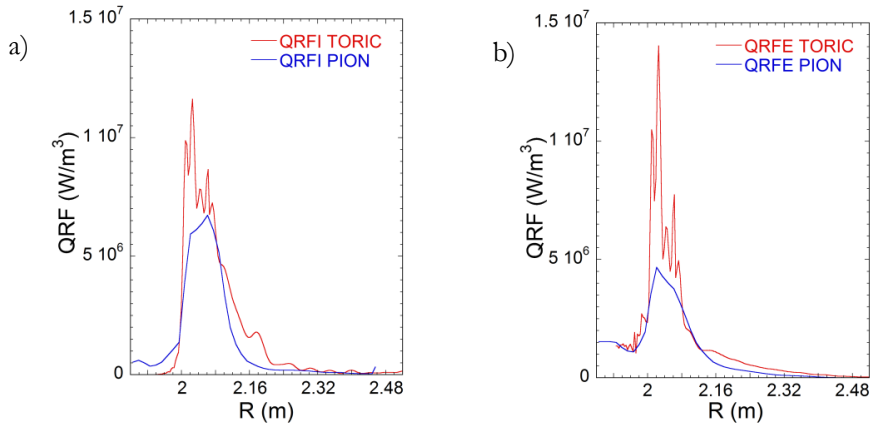

Fig. 5.2. ICRH deposition profiles for ions (a) and electrons (b) with red lines for TORIC and blue lines for PION (7.5 T, 73 MHz, n_{3He}/n_e=3%).

Pedestal values: they have been estimated with a simplified process. From the relation between the pedestal energy and the total energy (W_{ped} ~ 40% W_{tot} [104,105]) in a good quality H-mode (with an H factor equal to 1) the temperature pedestal can be calculated, once the mean plasma density is known. This last quantity has been assumed close to the Greenwald limit. The same temperature pedestal has been used in all simulations. In any case the modelling work is focused on core transport issues, and transport models characteristic of the core plasma have been used. The pedestal values have been inserted in the JETTO code with different methods. For almost all the simulations the edge temperatures have been assigned at the top of the pedestal. A more realistic method has been used in the case with ECRH+ICRH as heating systems: ETB and ELMs have been used to obtain the temperature pedestal. After verifying the equivalence of the two methods of producing the boundary conditions, the first one has been chosen because of the better stability of the simulations.

Sawteeth effect: it has not been taken into account for the H-mode scenario simulations because of the high margins of uncertainty in including verisimilar sawteeth and possible stabilization techniques. A flattening of profiles within q=1 is expected in conditions where sawteeth are allowed to develop.

Poloidal rotation effect: the poloidal rotation is assumed to be neoclassical.

Density profile: for the H-mode scenario the density profile has been in first instance assigned with rather flat shape according to typical H-mode density profiles, in second instance calculated with first-principle models, resulting in significant peaking due to the low collisionality.

Toroidal rotation effect: when the effect of rotation is considered, the toroidal momentum transport equation is solved. Rotation is modeled by assuming a turbulence driven inward momentum pinch, as reported in paragraph 4.1 (the assumptions of Prandtl num-

ber $Pr = \chi_\phi/\chi_i = 1$ and pinch number $Rv_\phi / \chi_\phi \sim 4$ are made following the results of experimental investigations and theoretical studies [40,41,106-110]), with the boundary value of the rotation due to edge intrinsic rotation or the torque caused by NNBI at high plasma density. The impact of rotation on plasma performance has been evaluated either according to existing transport models or according to recent JET results on ion stiffness mitigation in presence of rotation and low magnetic shear.

Different core transport models have been used: first principle models (Weiland and GLF23) and semi-empirical models (mixed Bohm-gyroBohm and Critical Gradient Model). In the CGM simulations the electron and ion thresholds have been calculated from the theory based formulas reported in Chapter 2 of this thesis ((2.67), (2.73)), whilst the stiffness coefficients have been chosen following the results of recent transport experiments on JET [26-28,57], i.e. $\chi_{se} \sim 1$ for electrons and $\chi_{si} \sim 2\text{-}4$ for ions, which implies rather high stiffness for both heat transport channels. In cases in which the toroidal rotation has been included in the prediction, the ion stiffness profile shown in figure 4.1, and obtained from experimental studies at JET, has been used. It is characterized by a low value of stiffness in the inner radial part of the plasma and an higher value externally.

All the simulations have been made with evolving current, ion and electron temperatures. In all the following figures, the radial coordinate is the square root of the normalized toroidal magnetic flux, indicated as rhotn.

5.3 Reference H-mode scenario with 30 MW ICRH

Simulations of the reference H-mode scenario shown in the first column of the table 5.1 are carried out Different transport models are used and the resulting ion and electron temperature profiles together with the assigned density are shown in figure 5.3.

For electrons the range of predicted temperatures is not large, although the Bohm-gyroBohm model gives much broader T_e profiles than all other models. In the very central region of the plasma the CGM model produces electron temperatures much higher with respect to other models. However in this zone the T_e profile is characterized by R/L_{Te} under the TEM threshold. The residual transport is then responsible for this plasma zone. For all the transport models the neoclassical diffusivity has been taken into account, neglecting the plausible finite turbulent diffusivity which can exist below the threshold, for instance due to some residual small-scale turbulence or to turbulence spreading. We know the electron neoclassical diffusivity is very small, and it causes a very peaked T_e in the central plasma. However, because in this region mechanisms different from the processes that are at the basis of the considered transport models take place, using these tools to model temperatures in the very central region makes no sense. In addition central temperatures are not significant for the global confinement. Then we are not interested in predicting their values.

For ions there is a wider range of predictions, up to a factor 2 in central T_i. A choice must then be made amongst the different models to select the most reliable prediction. It is not granted that all the models work well in the domain of high B_T machines, as they have

commonly been validated against data of medium-size, lower B_T machines. We tend to attach better reliability to the predictions of GLF23 which has the broadest physics basis and to CGM which is derived directly from experimental data of different devices and from inter-machine comparisons [27], and which turns out to agree to good extent for ions with GLF23. In the region between ρ=0.2 and ρ=0.8 the CGM electron temperature profile is little larger even though similar to the GLF23 profile, so we can indicate a substantial agreement also for electron temperatures obtained by CGM and GLF23 models.

Therefore we would retain as most reliable prediction, for the FAST reference H-mode scenario with 30 MW ICRH, values of T_{i0}~12 keV, T_{e0}~15 keV with a density n_{e0}~2.4 10^{20} m^{-3} and a confinement time τ~0.4 s, yielding a value of the triple product equal to $n_{e0}T_{i0}\tau \sim 1.5\ 10^{21}$ keVs/m^3.

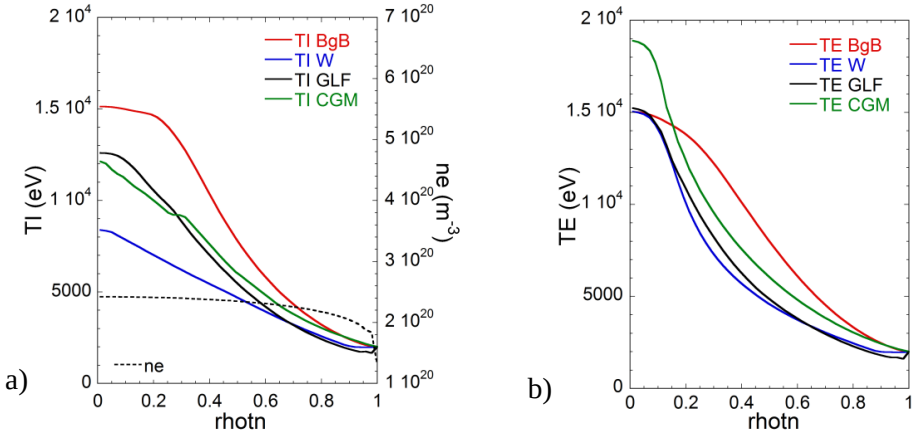

Fig. 5.3. Ion (a) and electron (b) temperature profiles for 7.5 T reference H-mode scenario, 30 MW ICRH calculated with PION, using different transport models: red profiles are for Bohm-gyroBohm, blue for Weiland, black for GLF23 and green for CGM. The assigned density profile is shown in (a) with dotted line.

In order to obtain a more physics based simulation, also the density profile has been calculated consistently by the different models (Bohm-gyroBohm, Weiland, GLF23). Temperature and density profiles obtained using different transport models are shown in figure 5.4. Good agreement between the 3 different models has been found in predicting a rather peaked n_e profile, which makes conditions easier from the point of view of disruption limits, still retaining high central n_e values.

The simulations with GLF23 corresponds to T_{i0}~11 keV, T_{e0}~13 keV with a density n_{e0}~3.3 10^{20} m^{-3} and a confinement time τ~0.5 s, yielding $n_{e0}T_{i0}\tau$ ~1.7 10^{21} keVs/m^3.

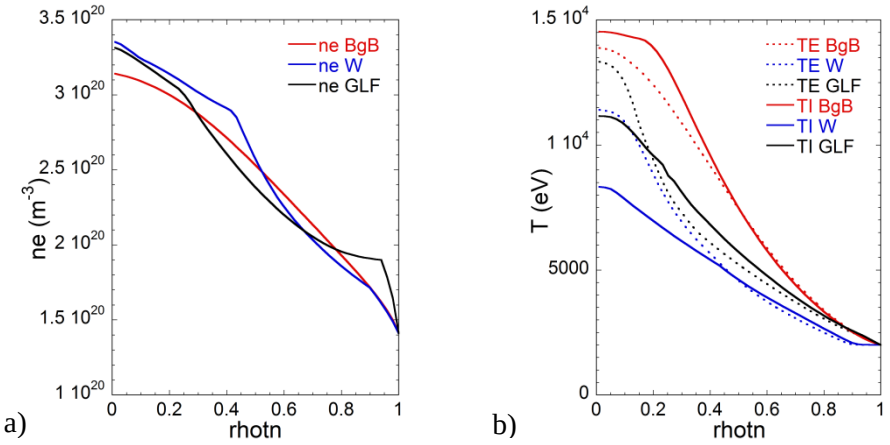

Fig. 5.4. Ion and electron temperature profiles (a) and calculated density profiles (b) for 7.5 T reference H-mode scenario, 30 MW ICRH calculated with PION, using different transport models: Bohm-gyroBohm in red, Weiland in blue, GLF23 in black.

5.4 H-mode scenario with 15 MW ICRH and 15 MW ECRH

For the substitution of 15 MW of ICRH with 15 MW of ECRH power, the ECRH power deposition profile of figure 5.5 has been calculated through the code GRAY.

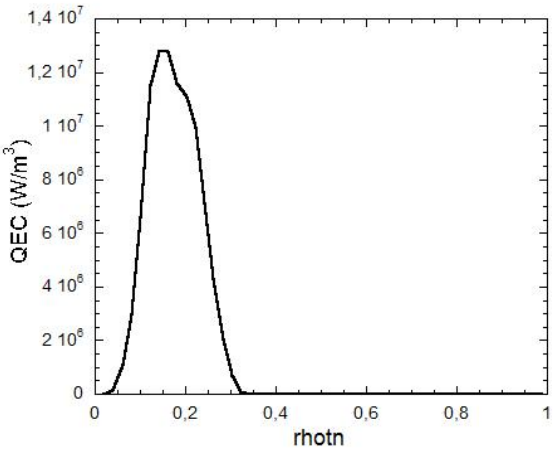

Fig. 5.5. ECRH power deposition profile calculated by GRAY. The ECRH is characterized by 15 MW of power, 170 GHz, 1st Harmonic O-mode from LFS. The deposition profile is the result of the superposition of 15 beams of 1 MW launched at toroidal angle of 0° and with different poloidal angles, chosen in order to have a uniform volumetric power density in the range between rhotn=0.15 and rhotn=0.25.

The obtained temperature profiles are shown in figure 5.6, where they are directly compared to those with 30 MW ICRH. Differently from figure 5.3, for both cases ICRH profiles are provided by TORIC, and the Bohm-gyroBohm model was used in an older version. The substitution of 15 MW ICRH with 15 MW ECRH is not beneficial from the point of view of confinement, although it is known to alleviate the issue of high impurity

influx from ICRH antenna. Colder ions and not significantly hotter electrons than the full ICRH case are found. It is caused by increased electron heating and decreased ion heating, together with the high electron stiffness and the decrease in ITG threshold associated to higher T_e/T_i values (as described in the paragraph 2.3.4 of this thesis). Therefore we have proceeded with the analysis focusing on the 30 MW ICRH H-mode, investigating in detail the effect of plasma rotation.

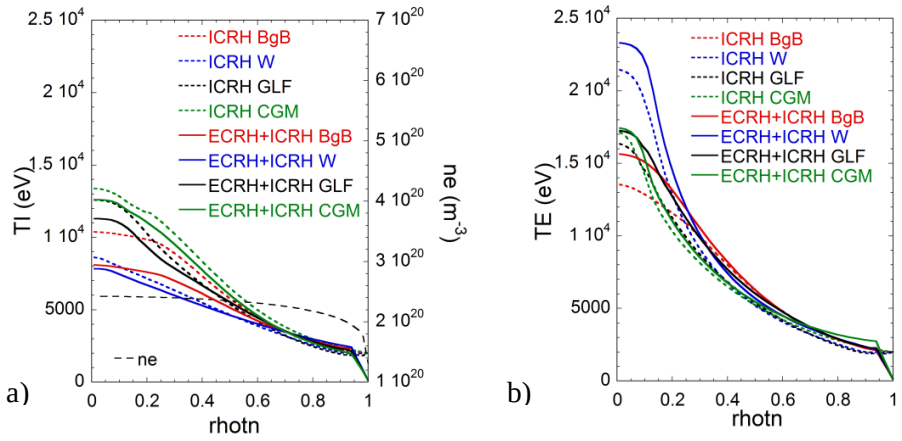

Fig. 5.6. Assigned density (a) and ion (a) and electron (b) temperature and profiles for the case of 6 T H-mode with ICRH +ECRH (full line) and full ICRH (dotted line). Red lines are for old Bohm-gyroBohm, blue for Weiland, black for GLF23 and green for CGM. ICRH is calculated with TORIC.

5.5 H-mode scenario simulations including the effect of rotation

Finally, also the role of toroidal rotation has been taken into account. From the recent experimental studies reported in paragraph 2.3.4 and confirmed by the results obtained in Chapter 3 it seems to have a key role in achieving improved ion core confinement, not only through the well-known threshold up-shift, but through a significant reduction of the ion stiffness in the region where q profile is flat [27-30,111,112]. Such ion core confinement improvement seems to be an essential ingredient for obtaining steady-state scenarios with a core region of enhanced pressure gradient and associated bootstrap current.

The rotation has been included in the simulations by self-consistently modelling also the momentum transport with the physical assumptions described in paragraph 5.2. Two sources of rotation have been considered. First, the edge driven intrinsic rotation, which, due to the inward pinch, can be transported into the plasma core. This intrinsic rotation is a well known observation in tokamaks [35,113], but a quantitative understanding of the phenomenon is still lacking, therefore extrapolation to non-existing devices is to be taken with care. Second, the core torque due to 10 MW NNBI, which allows a safer prediction through the ASCOT code.

5.5.1 H-mode scenario with 30 MW ICRH and intrinsic rotation

At present the mechanism at the basis of the intrinsic rotation is not totally understood and theory-based predictions of this phenomenon are lacking. For these reasons, in order to include the effect of the intrinsic rotation in the predictive work of the scenarios for FAST, we have followed the empirical scaling provided by Rice [35] and illustrated in figure 5.7, for which the intrinsic rotation depends on the plasma parameters with the following expression

$$M_A = 0.65 \cdot \beta_T^{1.4} q_*^{2.3}, \qquad (5.1)$$

where M_A is the Alfven Mach number (given by the ratio between the toroidal rotation velocity and the Alfven speed $C_A \approx B_T/\sqrt{\mu_0 n_e m_{ave}}$, with $m_{ave} \approx m_i[1 - (Z_{eff} - 1)/Z_I]$, where Z_I is the charge of the dominant impurity ion) and $q^*=2\pi\kappa a^2 B/\mu_0 R I_p$.

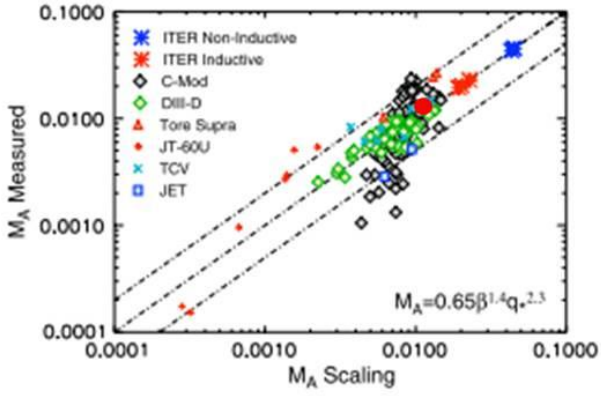

Fig. 5.7. The measured Alfven Mach number as a function of the scaling reported in the formula (5.1) for different machines: C-Mod (black diamonds), DIII-D (green diamonds), Tore Supra (red triangles), JT-60U (red + signs),TCV (blue × signs) and JET (blue squares). Dashed lines represent a factor of two variation. Red and blue asterisks are for ITER inductive and non-inductive scenarios, respectively. The red point indicates the M_A estimate for FAST for the reference H-mode scenario. Figure modified from [32].

This scaling has recently been questioned on the basis of new JET experimental evidence [113]. However, since high values of intrinsic rotation are measured in C-MOD, a high field compact machine conceptually similar to FAST, it may be still legitimate to assume for FAST an edge rotation value as predicted by the existing C-MOD driven empirical scaling. Then we have derived for FAST an edge rotation value Ω=30 krad/s. No torque sources are included. Figure 5.8 shows the rotation profile obtained with the assumptions described above (Pr =1 and $Rv_\phi/\chi_\phi \sim 4$). A very significant rotation gradient is predicted.

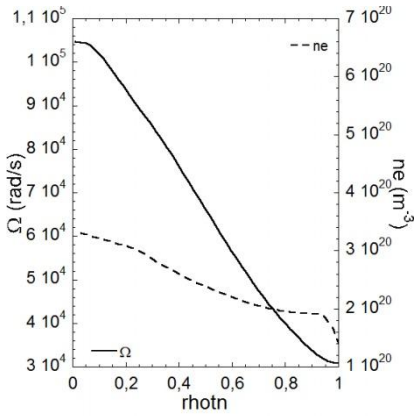

Fig. 5.8. Assigned peaked density and calculated rotation.

In the transport code JETTO the implementation of the rotation into the Weiland model is very recent and still under test. For GLF23 the rotation model does not feature a momentum pinch. Forcing a momentum transport model by prescribing Prandtl and pinch number, as described in paragraph 5.2, and still using GLF23 or Weiland for heat, leads to numerical instabilities problems, still unresolved. For these reasons the two first principles models cannot be used to investigate the impact of rotation.

In order to estimate the rotation effect on confinement we have then used the CGM model in which the stiffness value has been decreased in the centre as found in JET and reported in paragraph 2.3.4 of this thesis [28-30]. Unlike the first investigated case (figure 5.3), the assigned density profile is supposed peaked, according to the results represented in figure 5.4.

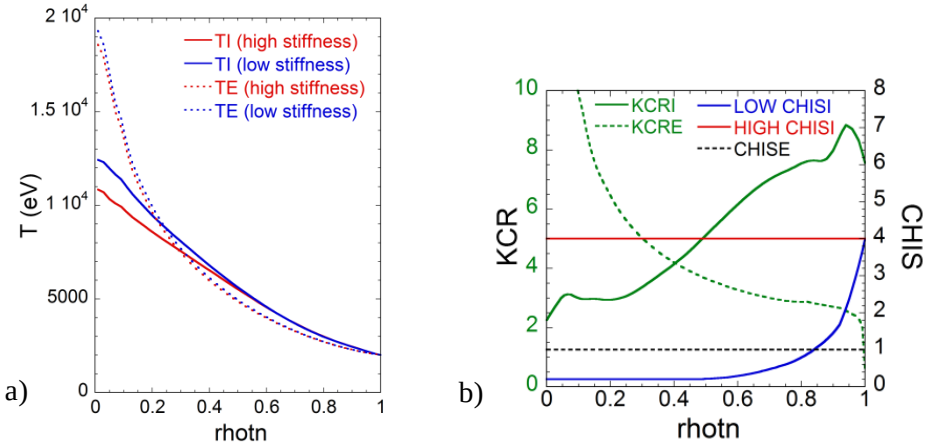

Fig. 5.9. T_i, T_e (a) profiles for 7.5 T 30 MW ICRH H-mode scenario using Pr=1, $Rv_\phi / \chi_\phi \sim 4$ and edge intrinsic rotation for momentum transport and CGM for heat transport with low ion stiffness in the rotating case. (b) Threshold (kcr) and stiffness (chis) profiles for ions and electrons.

The assumed profiles for threshold and stiffness are shown in figure 5.9b. Whilst the threshold profiles are calculated using theory-based formulas and are kept the same in the

two cases with and without rotation, different ion stiffness profiles have been taken from JET results with/without rotation. This extrapolation is rather arbitrary, but we presently lack a theoretical model describing the effect of rotation on ion stiffness, which has been experimentally found much more significant than the threshold up-shift in JET. Figure 5.9a shows the impact on ions (electrons are unaffected by rotation. About the very central electron temperature value that is much larger with respect to the profiles of figure 5.4a, obtained with other transport models, we refer to the explanation given in the paragraph 5.3). It is seen that in the H-mode scenario the impact of rotation is significant from ρ~0.5 to the centre but not dramatic. With the effect of the rotation the ion temperature increases by 1.5 keV.

5.5.2 H-mode scenario with 20 MW ICRH and rotation driven by 10 MW NNBI

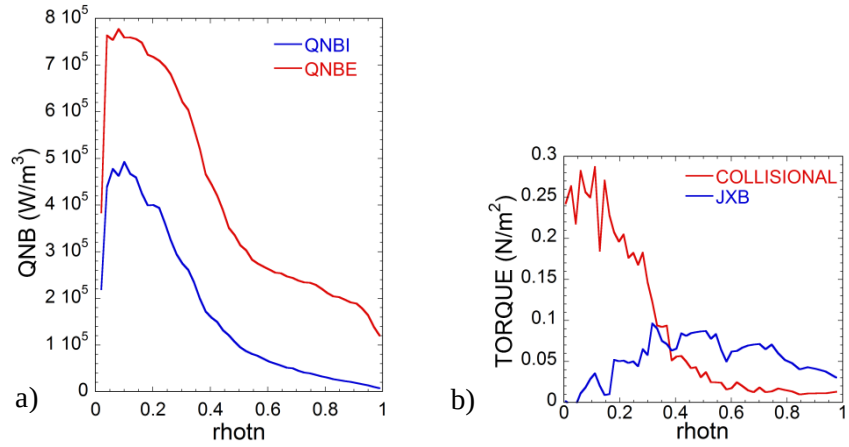

Fig. 5.10. NNBI power depositions (a) and torque (b) profiles calculated by ASCOT for 7.5 T 10 MW NNBI + 20 MW ICRH H-mode scenario using Bohm-gyroBohm for heat transport.

Instead of an intrinsic source of rotation we can provide an external source of rotation introducing the NNBI power [114]. In particular 10 MW of RF heating have been replaced by 10 MW of NNBI. The NNBI power depositions, calculated by ASCOT, can be seen in figure 5.10a and are peaked at the plasma centre, although a very significant fraction of power is deposited externally due to the high density. In figure 5.10b the torques are presented. The collisional torque is the dominant one in the central region, whilst the **J**x**B** torque is dominant in the region ρ>0.5.

Figure 5.11 shows the rotation profiles obtained with 10 MW NNBI + 20 MW ICRH both in absence and in presence of an edge driven intrinsic rotation, compared with the cases at 30 MW ICRH. In all cases the momentum equation is solved using the diffusivity and pinch calculated as discussed in paragraph 5.2.

The CGM model, utilized for the case of only ICRH, has not been used to calculate the heat transport when ICRH and NNBI are the heating systems, because the outcome of CGM would not substantially differ from the case shown in figure 5.7 and 5.8, since the

rotational shear is very similar. The heat transport is instead here calculated using the Bohm-gyroBohm model with the ad hoc criterion that switches off turbulent transport in the region where a suitable combination of **E**x**B** flow shear and magnetic shear is reached (see the description of the Bohm-gyroBohm model in paragraph 2.2 of this thesis).

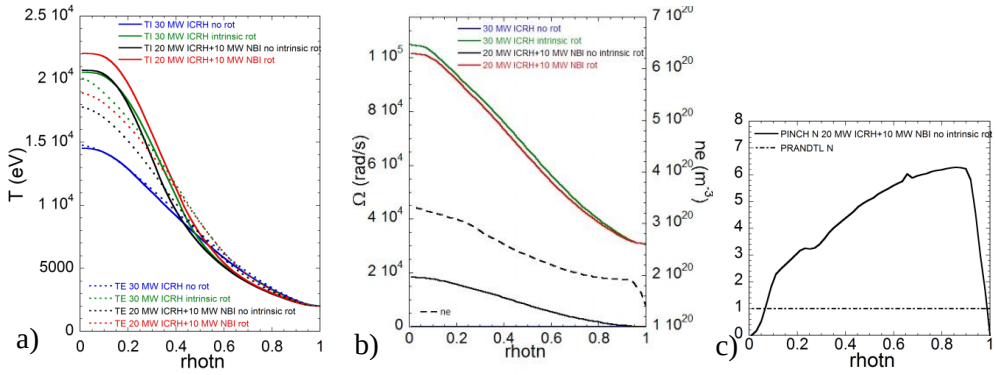

Fig. 5.11. Assigned peaked density and calculated rotation (a), T_i, T_e (b) profiles and Pinch and Prandtl numbers (c) for 7.5 T 30 MW ICRH (blue without and green with edge intrinsic rotation) and 20 MW ICRH + 10 MW NNBI (black without and red with edge intrinsic rotation) H-mode scenario using BgB for heat transport.

The Bohm-gyroBohm model together with the above described criterion is a very rough model, which produces the same effect on transport (likely overestimated, if one compares with figure 5.8a) for any rotation value that fulfils such criterion, irrespective of its value.

The rotation induced by the NNBI, in the absence of intrinsic rotation (this case is shown by black profiles of figure 5.11), is already enough to produce stabilization with respect to the full ICRH non-rotating case, thereby peaking the temperature profiles significantly. Adding an edge intrinsic rotation under the assumptions described earlier dominates on the effect of the NBI torque, as shown by the green lines of figure 5.11, but the temperature profiles do not peak further due to the model assumptions. However the NNBI driven rotation is based on a sounder physics, and therefore would ensure in FAST a basic level of rotation. Intrinsic rotation can be thought to further increase the attained rotation values.

5.6 AT scenario simulations including the effect of rotation

The role of rotation is essential in Advanced Tokamak (AT) scenarios. As described in paragraph 1.3 of this thesis, the q profile is also an essential factor to give rise and sustain the improved confinement that characterizes these scenarios, however it has been shown experimentally in several machines that the q profile alone is not sufficient to produce advanced scenarios [115,116]. In particular, for steady state scenarios, a reversed or flat q profile is necessary but not sufficient in order to provide ion ITB formation. A reversed or flat q profile is known to be produced using the lower hybrid (LH) heating system. It is also capable of driving plasma current, which, together with the neoclassical bootstrap

current mechanism, represent the current sources for obtaining a partial or full non-inductive plasma regime. In our simulations the LH heating is imposed through the power deposition and current density profiles calculated with the fast ray tracing code (FRTC), that is coupled with JETTO, as described in the paragraph 4.1 of this thesis. The used power deposition profile is shown in figure 5.12.

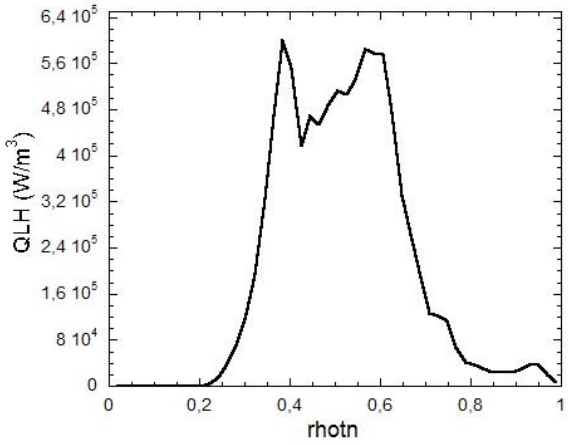

Fig. 5.12. LH power deposition profile calculated by FRTC. The LH is characterized by 4 MW of power, 5 GHz of frequency and the peak of value of parallel index refraction spectrum $n_{peak||}$=2.3.

Simulations of the AT scenario have been performed using the Bohm-gyroBohm model. Because of the key role of the rotation for the AT generation and sustainment, the analysis of this scenario has been done directly considering the presence of the toroidal rotation, intrinsic or/and driven by heating systems. The CGM model, used in H-mode simulation, has to be excluded because we do not have sufficient empirical data in order to suppose realistic values of stiffness and threshold for predictions of advanced scenarios of a new machine. The two first principles models Weiland and GLF23 cannot be used to investigate the effect of rotation as explained in paragraph 5.5.1. The inclusion of the rotation into the AT transport simulations is then possible only using the Bohm-gyroBohm model.

As in the case of H-mode scenario, two possible sources of toroidal rotation have been considered. The effects of the edge driven intrinsic rotation have been investigated in the simulation of the AT scenario characterized by 30 MW of ICRH. Substituting 10 MW of ICRH with 10 MW of NNBI has then permitted to study the impact of the core torque arising from the NNBI system.

5.6.1 AT scenario with 30 MW ICRH and intrinsic rotation

In the case with intrinsic rotation the ITB criterion embedded in the Bohm-gyroBohm model is switched on, yielding ITB formation by suppressing turbulent transport when a suitable combination of rotational and magnetic shear is reached (see paragraph 2.3.4 of this thesis). Temperature profiles resulting from an ITB formation are compared with the

case without rotation in figure 5.13a, where the assigned density profile is shown too. Figures 5.13b, 5.13c represent the profiles of angular rotation and safety factor, calculated in the simulations before (5.13b) and during (5.13c) the ITB formation in the case of the existence of the toroidal rotation driven by a momentum pinch. In the phase before ITB formation the presence of turbulent momentum pinch allows for peaked rotation profile (figure 5.13b) and sufficient rotational shear to trigger ITB. However, when the ITB is fully established and turbulence stabilized, it is expected that the turbulent momentum pinch vanishes as illustrated in figure 5.14, where the Pinch number profile before and during the ITB formation are shown together with the Prandtl number profile. This leads to loss of the ITB.

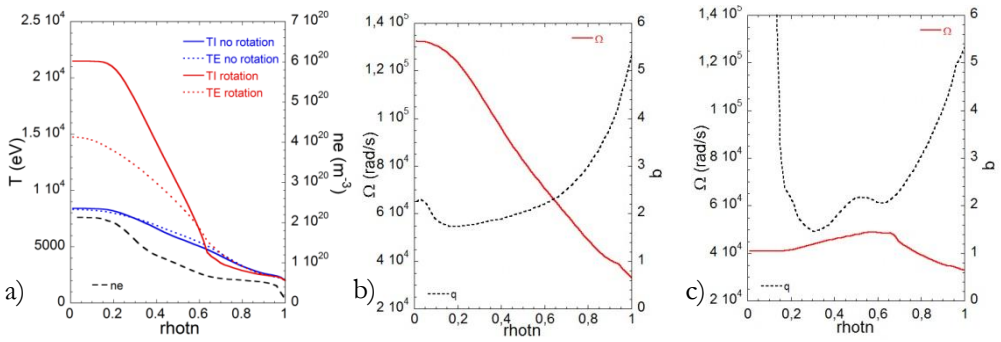

Fig. 5.13. (a) Ion and electron temperatures and imposed density profile for a 3.5 T ICRH+LH AT scenario with reversed q profile. Rotation is driven by edge intrinsic rotation and momentum pinch. Bohm-gyroBohm is used for heat transport and TORIC for ICRH. (b) Rotation and q profile obtained before the ITB formation, under the hypothesis of edge intrinsic rotation and turbulent pinch. (c) Rotation and q profile obtained during the ITB phase, under the hypothesis of no pinch in the ITB and existence of a core counter-torque driven by ICRH.

This could lead to a cyclic behaviour, such as observed in Tore Supra for reasons linked to magnetic shear [117]. The presence of a non-zero torque inside the ITB radius is the only way forward to guarantee stable ITB sustainment. In Alcator C-MOD ITB formation and sustainment for ICRH plasmas has been observed, due to the existence of some source of counter-torque caused by ICRH itself [118]. It leads to a hollow rotation profile, that allows sufficient shear to maintain the ITB. The presence of a counter-torque generated in pure ICRH plasmas is known and has been observed in several machines [119,120]. Following this dynamics we obtain the hollow rotation profile shown in figure 5.13c, and temperature profiles very similar to those in figure 5.13a, obtained for peaked rotation. The difference between the q profiles shown in the figures 5.13b and 5.13c is due to a known feedback loop. In fact the ITB formation causes the pressure gradient enhancement, which leads to the bootstrap current generation. This last quantity produces hollow current profiles, that induces a more reversed q profile, which further contributes to the ITB formation.

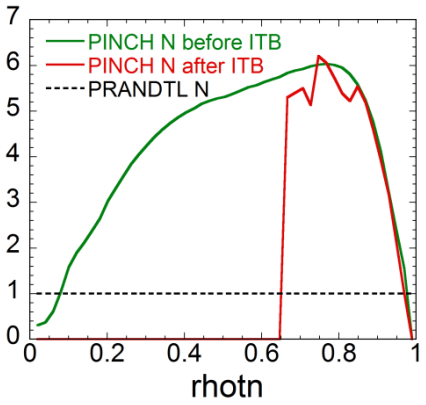

Fig. 5.14. Profiles of Pinch number and Prandtl number for the phase before ITB formation (green) and during ITB sustainment (red).

Profiles of the current density for the case in which the intrinsic rotation is present are shown in figure 5.15. They are relative to the rotation and q profiles represented in figures 5.13b and 5.13c, before the ITB formation and during the ITB.

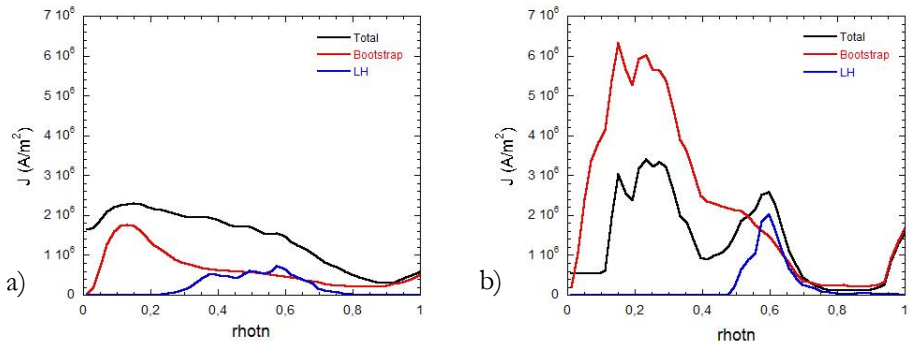

Fig. 5.15. Current deposition profiles (a) before the ITB formation and (b) during the ITB phase.

A fully non-inductive pulse can be achieved with the intrinsic edge rotation, fully reversed q profile, and sustained ITB at $\rho \sim 0.6$. Indicative values are $T_{i0} \sim 20$ keV, $T_{e0} \sim 15$ keV with a density $n_{e0} \sim 2\ 10^{20}$ m^{-3} and a confinement time $\tau \sim 0.2$ s, yielding a triple product value $n_{e0}T_{i0}\ \tau \sim 8\ 10^{20}$ keVs/m^3. These parameters have to be regarded as overestimated due to the simplistic assumptions of the Bohm-gyroBohm model.

5.6.2 AT scenario with 20 MW ICRH and rotation driven by 10 MW NNBI

As for the H-mode scenario, also in AT scenario 10 MW of ICRH have been substituted with 10 MW of NNBI power. Figure 5.16 shows the rotation profiles obtained in absence and in presence of the intrinsic rotation, before the ITB formation (b) and during the ITB phase (c). In the initial phase, in presence of intrinsic rotation, the rotation assumes similar values to the case with 30 MW of ICRH; in absence of intrinsic rotation, the rota-

tion is much lower, but still peaked. Also in this case the ITB formation is allowed and it then causes the vanishing of the turbulent momentum pinch.

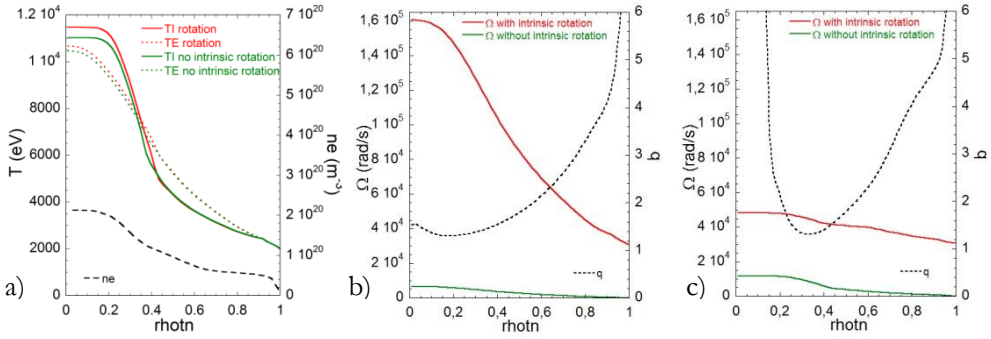

Fig. 5.16. (a) Ion and electron temperatures and imposed density profile for a 3.5 T ICRH+NBI+LH AT scenario with reversed q profile. Rotation is driven by NNBI driven co-torque, in presence and in absence of edge intrinsic rotation and momentum pinch. Bohm-gyroBohm is used for heat transport, TORIC for ICRH and ASCOT for NNBI. (b) Rotation and q profile obtained before the ITB formation, under the hypothesis of turbulent pinch, in presence and in absence of edge intrinsic rotation. (c) Rotation and q profile obtained during the ITB phase, under the hypothesis of no pinch in the ITB and the existence of a co-torque driven by NNBI in presence and in absence of edge intrinsic rotation.

However, as we can see looking at figure 5.16c, the rotational shear is still present because of the existence of NNBI driven co-torque. It then permits the sustainment of the ITB, as the correspondent ion and electron temperatures profiles show in figure 5.16a. The q profile is reversed, however the different magnetic shear evolution with respect to the case of only ICRH leads to a narrower ITB region. In addition, having substituted 10 MW of centrally localized ICRH with 10 MW of broader NNBI power causes lower central temperature values. Also in the AT scenario the effect of the intrinsic rotation dominates on the NNBI driven torque. As remarked before, however, NNBI provides a more reliable source for toroidal rotation shear, which is an essential ingredient for achieving ITB formation.

5.7 Summary

In conclusions, refined core transport modelling of FAST scenarios based on a careful combination of existing theory based models and latest experimental results from existing machines confirmed the expectation that FAST can be a valuable aid to ITER exploitation and to address integrated scenarios (in H mode and in Advanced Scenarios) with a full tungsten wall and with a meaningful wall load ($P/R^2 \sim 12$ MW/m^2). The reference H-mode scenario performance has been assessed thoroughly, fully predicting T_e, T_i, n_e, and rotation, and evaluating the effect of rotation on thermal transport. The idea of lowering the amount of ICRH power by introducing an additional type of heating has been evaluated. ECRH does not seem advantageous, whilst NNBI offers various advantages, providing both fast particle energy in parallel direction and a safer basis for the genera-

tion of a beneficial toroidal rotation with respect to the mere intrinsic one. This will also allow to achieve fully non-inductive AT scenarios with ITB formation. The simulations provided a range of scenarios on which fast particle and burning plasma studies can be performed. Figure 5.17 shows TORIC calculations for the perpendicular beta of the fast ^{3}He ions (β_{Hperp}) heated by 30 MW ICRH at ^{3}He=3% (peak power density on the minority species~15 MW/m^3) in the reference H-mode scenario, as a function of density and electron temperature. In the transport simulations presented above for the H-mode reference scenario, typical values at the ICRH deposition (ρ~0.25) are T_e~8 keV, n_e~2.8 10^{19} m^{-3}, resulting in β_{Hperp}~2%. These values are well in line with the needs for exciting meso-scale fluctuations with the same characteristics of those expected in reactor relevant conditions, as investigated in detail in [121]. Lowering the ^{3}He concentration results ultimately in a lower beta due to lower peak values of power density and lower minority density, although the fast ion energies increase. The scenario flexibility available in FAST, as described by this work, is an important element for energetic particle physics studies.

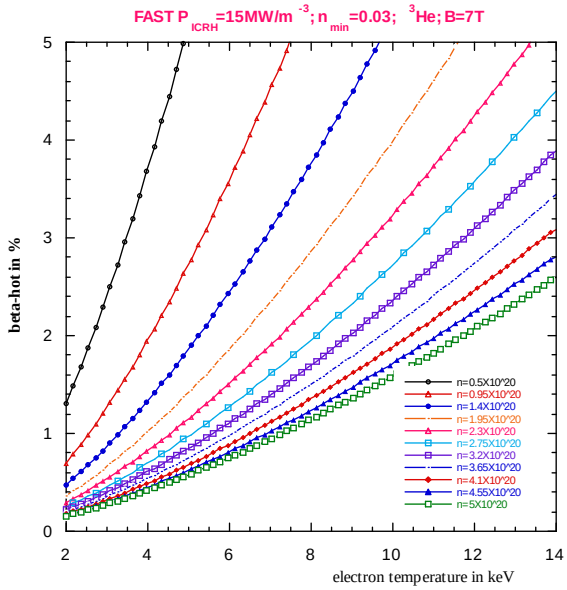

Fig. 5.17. Perpendicular beta of the fast particle component calculated by TORIC in reference H-mode scenario with 30 MW ICRH (~15 MW/m^3 peak power density) at ^{3}He=3% as a function of T_e for different density values.

Chapter 6

Gyro-kinetic simulations for the determination of the linear ion threshold value for FAST plasmas

In Chapter 5 predictive simulations for the future machine FAST have been described. To accomplish this task several assumptions and approximations have been done, linking theoretical and numerical predictions with experimental studies. In particular the ion inverse temperature gradient length threshold used in the CGM simulations has been calculated starting from the Romanelli's approximated formula, reported in Chapter 2. Through gyro-kinetic codes it is possible to give an estimate of the ion threshold including physical effects that have been neglected in the approximations at the basis of that formula. In this Chapter the calculation of the linear ion threshold through the gyro-kinetic code GKW (Gyro-Kinetics at Warwick) for the reference H-mode FAST scenario is reported. A short description of the theory on which GKW is based is written in paragraph 6.1. The simulations set-up together with the method for deriving the ion threshold and the obtained results are illustrated in paragraph 6.2. Finally a short summary and comments are presented in paragraph 6.3.

6.1 GKW

GKW [122,123,112] is a non linear flux tube gyro-kinetic code that aims at solving the turbulent transport problem arising in core plasmas of tokamaks. In the following the ordering proper to the code, its domain and coordinates system are presented. Then the method used to derive the gyro-kinetic equation is reported, and the inclusion of collisions is described. Maxwell equations are then derived in the gyro-kinetic form in the electrostatic case. Finally the outputs of the code interesting for us are described.

6.1.1 Orderings

The complete description of the plasma turbulence requires to solve 6 dimensional Vlasov (or Fokker-Planck) equations for each species, coupled with Maxwell equations [124]. The complexity of this kinetic approach is reduced by the gyro-kinetic theory, that leads to a 5 dimensional problem through the elimination of the fast cyclotron time scale. It is allowed when the frequency of the fluctuations is smaller than cyclotron frequencies. This can be expressed in the timescale ordering parameter

$$\epsilon_\omega \sim \frac{\omega}{\omega_{c\alpha}} \ll 1 \,, \tag{6.1}$$

where α indicates the considered species. This ordering is justified for instabilities of ITG or TE modes, that are thought to be some of the main responsible of turbulent transport in core plasmas as described in Chapters 1 and 2 of this thesis. The gyro-kinetic theory allows for perpendicular fluctuations on the scale of the gyro-radius $k_\perp \rho_i \sim 1$. Fluctuations are assumed to occur on the scale of the gyro-radius, which is ordered small relative to the background gradients, as expressed in the spatial scale ordering parameter

$$\epsilon_B \sim \frac{\rho_i}{L_Q} \sim \frac{\rho_i}{R} \ll 1, \tag{6.2}$$

where L_Q is the characteristic length of the variation of the background quantities $Q=\{B, T, n, \Omega\}$, and it is ordered to be on the scale of the device R. In addition the amplitude of the fluctuations, assumed small with respect to the background parameter, can be described by the fluctuation parameter

$$\epsilon_\delta \sim \left|\frac{\delta n}{n}\right| \sim \frac{e\delta\phi}{T} \ll 1. \tag{6.3}$$

Treating core turbulence of plasmas characterized by a large aspect ratio, the simplest ordering $\epsilon_\omega \sim \epsilon_\delta \sim \epsilon_B$ is employed and the expansion is expressed in terms of the normalized gyro-radius

$$\rho_* \equiv \frac{\rho_i}{R} \equiv \epsilon_B. \tag{6.4}$$

In order to exploit the ordering of eq. (6.3), the so called δf approximation can be made. It consists in splitting the distribution function f_{tot} into a perturbed distribution f and a background distribution F, $f_{tot}=F+f$, with ordering

$$f \sim \rho_* F. \tag{6.5}$$

Turbulent timescale orderings are expressed with respect to the thermal velocity v_{th}, that describes the parallel streaming along the magnetic field lines $v_{||} \sim v_{th}$. Perpendicular to the magnetic field, length scales may be of the scale of the gyro-radius since $v_d \sim \rho_* v_{th}$. The gyro-kinetic theory is then valid for cases without strong equilibrium flows. The parallel and the perpendicular perturbed dynamics are ordered as

$$\frac{k_{||}}{k_\perp} \sim \rho_* \ll 1. \tag{6.6}$$

which is equivalent to ordering the gradients of the perturbed distribution function as

$$\nabla_{||} f \sim \rho_* \nabla_\perp f. \tag{6.7}$$

From (6.2) the ordering that characterizes the variation of the perturbed distribution function with respect to the variation of the background distribution function perpendicular to the magnetic field is the following

$$\nabla_\perp f \sim \nabla_\perp F. \tag{6.8}$$

Instead, parallel to the magnetic field

$$\nabla_{||} f \sim \rho_* \nabla_{||} F. \tag{6.9}$$

If the existence of a toroidal rotation is foreseen, as in GKW, it is taken of the order of the thermal velocity $v_{tor} \sim v_{th}$. In GKW the equations are formulated in the co-moving system of a toroidally rotating plasma. In the laboratory frame the perpendicular component of the toroidal rotation appears as an **E**x**B** drift velocity, that is of the order of the thermal velocity. In order to satisfy the quasi-neutrality, a background potential is required in the presence of the centrifugal force. In the comoving frame the perturbed potential ϕ and the background potential Φ are taken to be of the following order

$$\phi \sim \frac{T}{e}\rho_*, \qquad \Phi \sim \frac{T}{e}. \tag{6.10}$$

Φ is an equilibrium quantity, so its gradient is ordered with the system size, and perpendicular perturbed and background gradients are of the same order $\nabla_\perp \Phi \sim \nabla_\perp \phi$. Then the **E**x**B** velocity in the rotating frame is ordered $v_E \sim \rho_* v_{th}$, the same order as the other drifts, according to the gyro-kinetic ordering. The potential parallel gradients fulfil $\nabla_{||}\Phi \sim \nabla_{||}\phi/\rho_*$.

6.1.2 Domain and coordinates system

GKW uses the local limit, which means that a small plasma region is simulated. It is characterized by a domain with a perpendicular extension near zero with respect to the device dimensions ($l_\perp/R \sim 0$), but larger than the turbulence scale length ($l_\perp >> \rho_i$). The background quantities are considered constant across the domain, but their gradients are kept as a linear drive term. The turbulence can be assumed homogeneous in the perpendicular plane, allowing periodic boundary conditions and a Fourier decomposition to be used in the perpendicular direction. The local limit is used in conjunction with a field aligned coordinate system, in which a parallel coordinate s parametrises a field line, and the other two (non-orthogonal) coordinates (radial (ψ) and binormal-axisymmetric (ζ)) are perpendicular to the field. The local limit in field aligned coordinates thus represents a 'flux tube' bounded by four field lines in which the effect of the magnetic shear is incorporated in the coordinate system. The parallel boundary is treated with a shifted-periodic boundary condition which preserves both poloidal and toroidal periodicity. The flux tube geometry tailors the simulation domain to the $k_\parallel \ll k_\perp$ structure of the turbulence, whilst also allowing a reduction of the simulation volume by exploitation of the axisymmetry. GKW is formulated in straight field line (Hamada) coordinates [125], in which the contravariant poloidal and toroidal components of the magnetic field are both flux functions.

The '$\sigma - \alpha$' equilibrium [126] (with s the magnetic shear and α is a measure of the Shafranov shift between the centres of consecutive magnetic surfaces, here set to zero) is directly implemented in the code. It is the simplest choice for the geometry of a tokamak, in which the flux surfaces are concentric circles, and the approximation of small aspect ratio is done. The coordinates can be approximated as

$$\psi = \frac{r}{R}, \qquad \zeta = \frac{1}{2\pi}(q\theta - \phi), \qquad \xi = \frac{\theta}{2\pi}, \tag{6.11}$$

where r/R is the aspect ratio, θ is the poloidal angle and ϕ is the toroidal angle.

6.1.3 Derivation of the gyro-kinetic equations

The modern method of derivation of the gyro-kinetic equations [127] is based on the guiding-centre transform [128,129] and the gyro-centre transform [130,131], based on the Hamiltonian or Lagrangian formalism with the Lie perturbation theory [132,133]. It requires considering three coordinate systems for the 6 dimensional phase space:

- the particle coordinates of position and velocities (**x**,**v**);
- the guiding-centre coordinates ($\overline{\mathbf{X}}$, $v_{||}$, $\bar{\mu}$, $\bar{\alpha}$): particles are represented by their guiding centres with respect to the equilibrium fields and a gyro-phase angle α;
- the gyro-centre coordinates (**X**, $v_{||}$, μ, α): particles are represented by their gyro-centres with respect to the total fields (equilibrium + perturbed) and a gyro-phase angle α.

Using the above mentioned transformations, the standard Lagrangian for a charged particle in a magnetic field

$$\gamma = (e\mathbf{A} + m\mathbf{v}) \cdot d\mathbf{x} - H dt, \qquad H = \frac{1}{2} m v^2 + e\phi, \tag{6.12}$$

(**A** is the vector potential) is transformed into the gyro-centre Lagrangian in the rotating frame, characterized by the frame rotation velocity $\mathbf{u_0}$, [134]

$$\Gamma = \left[Ze\mathbf{A} + m\left(v_{||}\hat{\mathbf{b}} + \mathbf{u_0}\right)\right] \cdot d\mathbf{X} + \mu d\alpha - H dt, \tag{6.13}$$

where the Hamiltonian $H=H_0+H_1+H_2+O(\rho_*^3)$ is given to first order

$$H_0 = Ze < \Phi > + \frac{1}{2} m v_{||}{}^2 + \mu B - \frac{1}{2} m \mathbf{u_0} \cdot \mathbf{u_0}, \qquad H_1 = Ze < \phi >. \tag{6.14}$$

Here < > is the average over the gyro-orbit

$$< h(\mathbf{x}) > = < h(\mathbf{X} + \boldsymbol{\rho}) > = \frac{1}{2\pi} \int_0^{2\pi} h(\mathbf{X} + \boldsymbol{\rho}) d\alpha. \tag{6.15}$$

ρ=ρ(**x**,μ) is the gyro-radius and depends on the magnetic moment of the particle. The Hamiltonian is used to first order for the evaluation of the motion equations, to the second order in the derivation of the field equations. After this initial truncation of the Lagrangian no approximations should be made in order to guarantee energy consistency for the equation set [135,136]. Starting from the generalized Hamilton's equation for any function h of the phase space

$$\frac{dh}{dt} = \{h, H\} + \frac{\partial h}{\partial t} \tag{6.16}$$

({} is the generalized guiding centre Poisson bracket [137,138]) the equations of gyro-centre motion in the rotating frame can be derived [134], choosing h=(**X**, $v_{||}$, μ, α) to be each of the coordinates in turn ($\partial h/\partial t = 0$),

$$\frac{d\mathbf{X}}{dt} = \frac{\hat{\mathbf{b}}}{Ze B_{||}^*} \times \nabla H + \frac{\mathbf{B}^*}{m B_{||}^*} \frac{\partial H}{\partial v_{||}}; \tag{6.17}$$

$$\frac{dv_{||}}{dt} = -\frac{1}{mv_{||}}\frac{d\mathbf{X}}{dt}\cdot\nabla H; \tag{6.18}$$

$$\frac{d\mu}{dt} = 0; \tag{6.19}$$

$$\frac{d\alpha}{dt} = \{\alpha, H\}, \tag{6.20}$$

where * indicates that the quantities are evaluated in the co-moving frame. The invariance of μ is a requirement of the gyro-kinetic theory. Inserting the expression for the Hamiltonian (6.13) in motion equations we obtain for the **X** coordinate

$$\frac{d\mathbf{X}}{dt} = v_{||}\hat{\mathbf{b}} + \mathbf{v}_D + \mathbf{v}_E, \tag{6.21}$$

where

$$\mathbf{v}_D = \frac{1}{Ze}\frac{mv_{||}^2}{B_{||}^*}\hat{\mathbf{b}}\times\left(\hat{\mathbf{b}}\cdot\nabla\right)\hat{\mathbf{b}} + \frac{\mu}{Ze}\frac{\hat{\mathbf{b}}\times\nabla B}{B_{||}^*} + \frac{2}{Ze}\frac{mv_{||}}{B_{||}^*}\Omega_\perp - \frac{1}{Ze}\frac{m\Omega^2 R}{B_{||}^*}\hat{\mathbf{b}}\times\nabla R + \frac{\hat{\mathbf{b}}\times\nabla\langle\Phi\rangle}{B_{||}^*} \tag{6.22}$$

and

$$\mathbf{v}_E = \frac{\hat{\mathbf{b}}\times\nabla\langle\phi\rangle}{B_{||}^*}. \tag{6.23}$$

$\boldsymbol{\Omega}$ is the toroidal angular velocity, $\mathbf{u_0} = \boldsymbol{\Omega}\times\mathbf{x}$. The drifts appearing in $\mathbf{v}_D$ are the curvature and the ∇B, two drifts arising from the inertial forces of the frame (Coriolis and centrifugal) and the **E**x**B** drift from the equilibrium potential Φ.

For the $v_{||}$ coordinate we have

$$mv_{||}\frac{dv_{||}}{dt} = -\frac{d\mathbf{X}}{dt}\cdot[Ze\nabla\langle\phi+\Phi\rangle + \mu\nabla B - m\Omega^2 R\nabla R]. \tag{6.24}$$

Applying the Hamilton equation to the guiding centre distribution f_{tot} leads to the gyro-kinetic equation

$$\frac{\partial f_{tot}}{\partial t} + \frac{d\mathbf{X}}{dt}\frac{\partial f_{tot}}{\partial \mathbf{X}} + \frac{dv_{||}}{dt}\frac{\partial f_{tot}}{\partial v_{||}} = 0, \tag{6.25}$$

where the motion equations (6.16-6.19) have been used. In addition the construction of the gyro-centre coordinates is such that $\partial f_{tot}/\partial\alpha = 0$ by definition.

Using the δf formalism and expanding the gyro-kinetic equation to order $O(\rho_*)$, the following gyro-kinetic equation for the perturbed distribution function for the case of electro-static perturbations is obtained

$$\frac{\partial f}{\partial t} + \frac{d\mathbf{X}}{dt}\cdot\nabla f - \frac{\hat{\mathbf{b}}}{m}\cdot(\mu\nabla B + \nabla\mathcal{E})\frac{\partial f}{\partial v_{||}} = S, \tag{6.26}$$

where $\mathcal{E} = Ze\Phi - \frac{1}{2}m\Omega^2(R^2 - R_0^2)$ is the so called centrifugal energy. It includes the effect of the centrifugal force and of the background potential (R_0 is a constant coming from the solution of the equilibrium equation, that is the gyro-kinetic equation to the lowest order [139]). The source term S is determined by the background distribution function and it is given by

$$S = -\mathbf{v}_E\cdot\left[\frac{\nabla n_{R0}}{n_{R0}} - \frac{m\Omega^2}{T}R_0\frac{\partial R_0}{\partial\psi}\bigg|_\theta\nabla\psi + \left(\frac{v_\parallel^2}{v_{th}^2} + \frac{\mu B+\mathcal{E}}{T} - \frac{3}{2}\right)\frac{\nabla T}{T} + \frac{mv_\parallel RB_t}{BT}\nabla\omega_\varphi\right]F_M +$$

$$-\frac{Ze}{T}\frac{d\mathbf{X}}{dt}\cdot\nabla\langle\phi\rangle F_M. \tag{6.27}$$

The background distribution function is assumed to be a Maxwellian with density, temperature and mean parallel velocity being functions of the radial coordinate only

$$F_M = \frac{n_{R0}}{(2\pi T/m)^{3/2}} e^{-\frac{m\left(v_{||}-u_{||}\right)^2/2+\mu B+\mathcal{E}}{T}}. \tag{6.28}$$

n_{R0} is the density obtained as solution of the equilibrium equation at $R=R_0$. The equation can be expressed as

$$\frac{\partial f}{\partial t} = -v_{||}\hat{\mathbf{b}}\cdot\nabla f - \mathbf{v}_D\cdot\nabla f - \mathbf{v}_E\cdot\nabla f + \frac{\hat{\mathbf{b}}}{m}\cdot(\mu\nabla B+\nabla\mathcal{E})\frac{\partial f}{\partial v_{||}} - \mathbf{v}_E\cdot\nabla F_M - \mathbf{v}_D\cdot\nabla F_M +$$

$$-\frac{Ze}{T}v_{||}\hat{\mathbf{b}}\cdot\nabla\langle\phi\rangle F_M - \frac{Ze}{T}\mathbf{v}_D\cdot\nabla\langle\phi\rangle F_M \tag{6.29}$$

The equations above apply to each of the species individually. The only non-linearity in the equations is given by the third term $\mathbf{v}_E\cdot\nabla f$, that is proportional to ρ_*^2. This term is neglected when linear stability is investigated. For the other terms on the right side of eq. (6.29), the first describes the free streaming motion of particle along the field line, the second term includes curvature and inertial drifts in the perturbed distribution which cause propagation of a drift wave. The fourth term describes the magnetic trapping as particles move through the magnetic field gradient, the fifth term provides the energy source from the background gradients that drive the instabilities. The sixth term, when combined with the collisions, can generate the neoclassical fluxes. The seventh term describes the collisionless parallel Landau damping of the perturbations against the background Maxwellian, and the eighth term describes the equivalent damping for the perpendicular drifts.

The co-moving system employed in GKW corresponds to a frame that rotates as a rigid body with constant frequency. The radial gradient in the toroidal rotation is treated through a radial gradient in the averaged parallel velocity of the background. The radial gradient of the perpendicular velocity was ignored at the time in which this thesis work has been done. However, as it is described in Chapter 2, this gradient is known to play an important role in the stabilization of the turbulence. The **E**x**B** shearing is always present for a purely rotating toroidal plasma and can also be related to a sheared poloidal rotation. In GKW the background **E**x**B** rotation is now taken into account adding an additional convective term for the perturbed distribution in the gyro-kinetic equation (6.29).

6.1.4 Collisions

The gyro-kinetic equation (6.29) has been obtained in the collisionless case. In GKW the collisions enter the evolution equation as an additional term

$$\frac{\partial \hat{f}_\alpha}{\partial t} = C\left(\hat{f}_\alpha\right) \tag{6.30}$$

Here the distribution function of the α species is expressed by the Fourier representation. Since the distribution function is small, GKW uses a linearised collision operator with the Maxwellian as background. Finite Larmor radius effects are neglected. Expressions for the collision operator published in literature are usually expressed in the (v,θ) coordinate system, where v is the velocity and θ is the pitch angle. The operator can be written as [140]

$$C(\hat{f}_\alpha) = \sum_\beta \left\{ \frac{1}{v^2} \frac{\partial}{\partial v} \left[v^2 \left(D_{vv}^{\alpha/\beta} \frac{\partial \hat{f}_\alpha}{\partial v} - F_v^{\alpha/\beta} \hat{f}_\alpha \right) \right] + \frac{1}{v \sin\theta} \frac{\partial}{\partial \theta} \left[\sin\theta D_{\theta\theta}^{\alpha/\beta} \frac{1}{v} \frac{\partial \hat{f}_\alpha}{\partial \theta} \right] \right\}, \tag{6.31}$$

where the sum is over all species β. $D_{\theta\theta}$ represents the pitch angle scattering, D_{vv} is the energy scattering and F_v is the slowing down force. The coefficients, obtained from the literature [140], can be expressed in normalized form

$$D_{\theta\theta}^{\alpha/\beta} = \sum_\beta \frac{\Gamma^{\alpha/\beta}}{4 v_\alpha} \left[\left(2 - \frac{1}{v_\beta^2} \right) \mathrm{erf}(v_\beta) + \frac{1}{v_\beta} \mathrm{erf}'(v_\beta) \right], \tag{6.32}$$

$$D_{vv}^{\alpha/\beta} = \sum_\beta \frac{\Gamma^{\alpha/\beta}}{2 v_\alpha} \left[\frac{1}{v_\beta^2} \mathrm{erf}(v_\beta) - \frac{1}{v_\beta} \mathrm{erf}'(v_\beta) \right], \tag{6.33}$$

$$F_v^{\alpha/\beta} = -\sum_\beta \frac{\Gamma^{\alpha/\beta}}{v_\alpha^2} \frac{m_{R\alpha}}{m_{R\beta}} \left[\mathrm{erf}(v_\beta) - v_\beta \mathrm{erf}'(v_\beta) \right], \tag{6.34}$$

where erf is the standard definition of the error function. Velocities and masses of these expressions are normalized. $\Gamma^{a/b}$ is a constant that depends on the Coulomb logarithm.

The linearised form of this Fokker-Plank operator conserves particle number but does not conserve momentum or energy. The conservation of parallel momentum can be reintroduced using a simplified model reported in [122]. The lack of the energy conservation is considered less crucial compared with momentum conservation since the present form of the collision operator drives the distribution towards a Maxwellian with specified temperature. Since in the local problem the temperature is specified as input parameter and no evolution in temperature is retained, a collision operator that maintains this temperature can be considered acceptable.

6.1.5 Maxwell equations

The gyro-kinetic equation must be combined with fields equations in order to form a closed system of equations. In deriving the gyro-kinetic equation (6.29) magnetic field fluctuations were neglected, so only an equation for the electrostatic field is required to close the system. It is the so called gyro-kinetic Poisson equation, that is replaced by the following constraint of quasi-neutrality

$$\sum_s Zen_s(\mathbf{x}) = 0, \tag{6.35}$$

where the sum is over all species. In gyro-centre phase space it is represented as

$$\bar{\rho}(\mathbf{X}) + \rho_{pol}(\mathbf{X}) = 0, \tag{6.36}$$

where $\bar{\rho}$ is the gyro-centre charge density and ρ_{pol} is the gyro-centre polarization density. ρ_{pol} describes the difference between the actual charge density and the charge density of

gyro-centres at a given point. A model of polarization consistent with the gyro-kinetic equation must be adopted. Obtaining the quasi-neutrality equation through the same derivation used to calculate the motion equations, the energy consistency can be guaranteed by including the next higher order energies in the field terms [141]. The complete derivation can be found in the literature [141]. The field equation can be written as

$$\sum_s \int d^3\mathbf{v}\left[Z_s e G f(\mathbf{x}) + F_M \frac{Z_s^2 e^2}{T_s}(1-G^2)\phi(\mathbf{x})\right] = 0, \tag{6.37}$$

where the first term represents the gyro-centre charge density integrated over all gyro-centres passing through **x**, whilst the second term represents the linearised gyro-centre polarization density for all the gyro-orbits passing through **x**. G is the gyro-average operator.

6.1.6 Outputs

GKW calculates the fluxes as guiding centre fluxes, given by the equation

$$\Gamma_i^{\psi} = \int d^3\mathbf{v}\, \mathbf{v}_E \cdot \nabla\psi \alpha_i f, \tag{6.38}$$

where i=(1,2,3) and α_i=(1,mv²/2,$v_{||}$). i=1 is the particle flux, i=2 is the heat flux, i=3 is the parallel momentum flux. For linear runs the dominant growth rate is calculated as

$$\gamma^{max}(t) = \ln\left[\frac{\sqrt{\sum_m |\hat{\phi}(t)|^2}}{\sqrt{\sum_m |\hat{\phi}(t-\Delta t)|^2}}\right] \Big/ \Delta t, \tag{6.39}$$

where $\hat{\phi}$ is the potential represented as a sum over Fourier modes. $\Sigma_m = \Sigma_{k_\varsigma}\Sigma_{k_\psi}\Sigma_\xi$ is a sum over all modes and along the full length ξ of the flux tube. In general all the perturbed quantities in the plane perpendicular to the magnetic field are represented by

$$g(\psi,\zeta,\xi) = \sum_{k_\zeta k_\psi} \hat{g}(k_\psi, k_\zeta, \xi) e^{ik_\zeta \frac{\zeta}{\rho_*} + ik_\psi \frac{\psi}{\rho_*}}. \tag{6.40}$$

The mode frequency is given by

$$\omega(t) = \left[\mathrm{Arg}\left(\sum_\xi \hat{\phi}(t)\right) - \mathrm{Arg}\left(\sum_\xi \hat{\phi}(t-\Delta t)\right)\right]/\Delta t. \tag{6.41}$$

6.2 Deriving the ion threshold

The linear part of the GKW code allows the calculation of the ITG linear threshold. As described in Chapter 2, ITG modes become unstable above the threshold value in the inverse gradient length of the ion temperature R/L_{Ti}. Then, finding the value of R/L_{Ti} for which the growth rate of the dominant instability is null and above which the instability takes place, gives an estimate for the linear ion threshold. First a scan in the wave vector k_ς is carried out in order to identify the mode characterized by the maximum growth rate, i. e. the last to be stabilized (k_ψ is taken equal to zero), fixing all other input parameters.

Using the k_ζ so obtained, scans in R/L_{Ti} are done fixing all the input parameters. The resultant growth rates are fitted as functions of R/L_{Ti}. The intercept of the fitting curve in correspondence of null growth rate is the linear estimate for the ion threshold. Following this procedure for different radial positions leads to the ion threshold profile.

6.2.1 Simulation set up

The parameters that characterize the reference H-mode of FAST described and simulated in paragraph 5.3 have been used as input data. In figure 6.1 the profiles used are represented. They have been obtained by simulations carried out through the JETTO code and using the transport model GLF23 that has the most solid physical basis as described in Chapter 5. They refer to the simulation with predictive T_i, T_e and n_e, reported in figure 5.4.

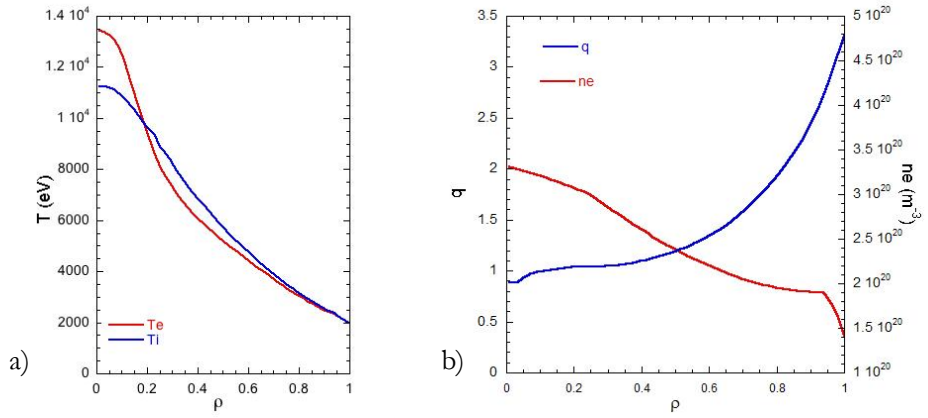

Fig. 6.1. Input data profiles obtained from JETTO simulations of reference H-mode for FAST using GLF23. (a) Temperature profiles, already shown in figure 5.4 together with the results obtained with other transport models. (b) q profile and density profile.

Collisions are taken into account using the collision operator described above. Simulations have been done considering both adiabatic electrons and kinetic electrons. In the first case only the equation for ions evolves and electrons are assumed to follow the Boltzmann distribution reported in Chapter 2 of this thesis (formula (2.19)). In the case of kinetic electrons both ion and electron equations evolve.

6.2.2 Simulation results

Scans have been carried out at the radial positions ρ=[0.2, 0.4, 0.6, 0.8]. In figure 6.2 two examples of the k_ζ scan for the radial positions ρ=0.4 (figure a) and ρ=0.6 (figure b) are shown. R/L_{Ti}=5.84 and R/L_{Ti}=6.74 are the values used for the illustrated scans, derived from the ion temperature profile obtained from the FAST simulation work and shown in figure 6.1a. The growth rate is maximum for $k_\theta\rho_{ref}$=0.6 at ρ=0.4 and for $k_\theta\rho_{ref}$=0.4 at

ρ=0.6. ρ_{ref} is the reference Larmor radius, $\rho_{ref}=m_{ref}v_{thref}/(eB_{ref})$, and reference physical parameters are chosen among the input data for normalizations of the code. Ions are considered as the reference species. k_θ is linked to k_ζ by the eq. (2.11) and $k_\theta\rho_{ref}$ is proportional to k_ζ through a metric element.

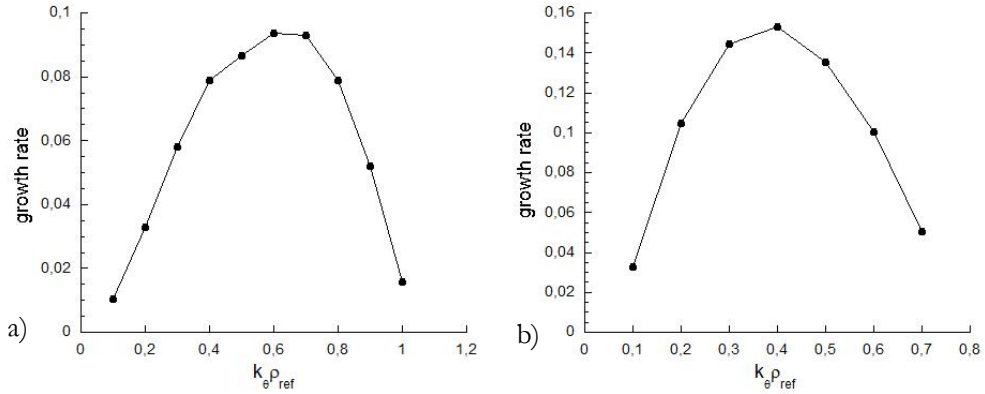

Fig. 6.2. Normalized growth rate as a function of $k_\theta\rho_{ref}$. The growth rate normalization is given by c_s/R. (a) refers to ρ=0.4, (b) to ρ=0.6.

Figure 6.3 shows the scans of R/L_{Ti} for different radial positions. The obtained points are better reconstructed by parabolic fittings, that are represented by the curves of the graph. Scans have been employed considering both adiabatic electrons and kinetic electrons.

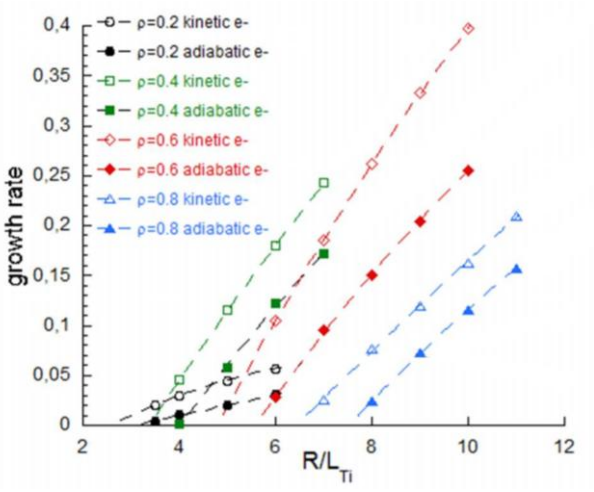

Fig. 6.3. Normalized growth rate as a function of R/L_{Ti} for different radial positions (marked with different colours) and considering adiabatic (full indicators) or kinetic (empty indicators) electrons. The growth rate normalization is given by c_s/R.

The resulting ion threshold profiles are reported in figure 6.4, where the cases with adiabatic and kinetic electrons are represented together with the ion threshold profile calculated through the F. Romanelli's formula (2.67), which has been used for FAST simulations reported in Chapter 5.

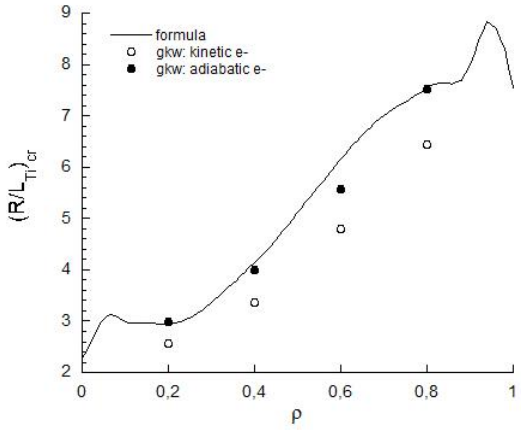

Fig. 6.4. Ion threshold profiles resulting from GKW simulations considering adiabatic (full points) or kinetic (empty points) electrons and compared with the ion threshold profile calculated through the Romanelli's formula (2.67) and represented by the line.

A good matching is found between the ion threshold profile calculated through the Romanelli's formula and the one obtained from GKW linear simulations using adiabatic electrons. However, in GKW simulations where the electron equation evolves, the ion threshold profile is found to reach lower values, of about 0.5-1 depending on the radial position, even if with a similar qualitative behavior. This indicates that the contribution due to the electron dynamics is not completely negligible for determining the ion threshold in these plasmas. For very accurate predictions of the reference H-mode scenario of FAST such effects should be taken into account. However, considering the several other sources of uncertainty that enter in predictive calculations of future machines, and the rather small size of the discrepancy, we can conclude that these gyro-kinetics simulations overall support the validity of the FAST simulations using the CGM model and Romanelli's threshold presented in Chapter 5. One more consideration that is left for future work is that finite

β effects may not be negligible for FAST in the central region of the plasma, so for more accurate predictions they should be taken into account, whilst the present simulations were made in the pure electrostatic approximation.

Chapter 7

Conclusions and perspectives

This thesis work has tackled the investigation of ion heat transport under 3 perspectives: the experimental investigation, the numerical modelling and the first principle theory. This variety of approaches has the purpose of achieving a close integration between experiment and theory, which has been shown vital in making steps forward in the path towards controlled nuclear fusion power.

The ion heat transport can be described by two essential parameters. The ion threshold, that is a critical value of the inverse characteristic length of ion temperature variation above which the transport is theoretically foreseen and experimentally observed to increase strongly becoming turbulent. Above threshold the ion temperature profiles tend to remain tied to the threshold, independently on the amount of heating power applied. The stiffness level is the parameter which quantifies this behavior.

Within the field of core ion heat transport studies, the 3 main questions that this thesis work has addressed are:

- How do the ion stiffness and threshold depend on plasma parameters?
- Which is the impact of the ion stiffness level on the global performances?
- How can we predict performances of future machines?

The thesis work has built upon previous work in the field, in particular recent experimental results in JET on the role of rotation on ion heat transport and the vast amount of theory investigation of the ITG instability that has led to the development of transport models and turbulence codes. Such pre-existing basis of the thesis work has been summarized in Chapter 2.

The actual thesis work has started with an experimental analysis of JET discharges made with the purpose of establishing if the previously found effect of rotation on ion stiffness is due to the rotation value or to its gradient, which in previous experiments were always coupled. Decoupling the two has required external means of rotation braking, such as enhanced B_T ripple or 3D magnetic fields due to error field correction coils, and also shots from a reverse B_T campaign to exploit the different torque deposition of counter-I_p NBI injection. This analysis, described in Chapter 3, has shown that it is the rotation gradient and not the rotation value that acts reducing the ion stiffness level. It has also shown that such effect is present no matter the sign of the rotation gradient, i.e. also for hollow besides peaked rotation profiles. The importance of this result for ITER scenario performance is clear: on ITER it may be difficult due to high inertia and to a very poor production of momentum by high energy NBI to reach high values of rotation, but it

may be easier to impose a sufficient rotation gradient, by counting on a NBI driven or intrinsic edge rotation and the existence of an inward momentum pinch, which for ITER parameters should be sizeable. The results of Chapter 3 indicate that this should be enough to get some ion stiffness mitigation, especially in Advanced scenarios where a region of low magnetic shear is present, and thereby the core ion confinement is enhanced, which is an essential ingredient of such scenarios.

The numerical analysis of the impact that ion threshold, stiffness and edge pedestal have on global parameters, such as global energy confinement and fusion power, has been described in Chapter 4. This was motivated by the questions often raised whether the parameters that characterize core heat transport are of any relevance for the scenario performance, which in H-modes seems to be dominated by pedestal height only. The present work has shown that although as well known the impact of pedestal on global confinement is high, due to the fact that volume integrals are dominated by the edge regions, still an optimization of core transport, acting on threshold and stiffness, can yield a relevant improvement on global confinement and even more on fusion power, which is heavily weighted on the core parameters and which is finally what one wants to maximize in a fusion reactor. In particular the ion stiffness, which is a parameter not much taken into account until now, and assumed or predicted very high in most existing models, turns out to be an extra tool on which we can act and whose reduction can be of significant help in improving performance. It could even play a key role in Advanced Scenarios, in which the pedestal at least in present machines plays a much smaller role. From the JET work it emerges that ion stiffness can be reduced to very low values with concomitant q profile shaping, whilst increases in threshold are rather limited by the accessible ranges of plasma parameters. Stiffness turns out then as an additional important knob, rather disregarded until now, on which to try and act whilst developing ITER relevant scenarios. It must be noted in addition that such improvement of core transport can be in any case very strategic when operation with high pedestal cannot be carried out because of excessive wall load issues. In other words, one could imagine alternative scenarios of H-mode type with reduced pedestal and more peaked temperature and density profiles, with equivalent or even better fusion performance than those envisaged until now, with limited profile peaking due to high stiffness and high pedestal. These considerations particularly apply to Hybrid-type scenarios, which feature a broad core region of flat q profile.

The experimental and modelling results of Chapters 3 and 4 and the conviction that numerical predictions of future machines have to be strongly linked with results in present machines, even if not yet fully explained by first principle models, have led to the work presented in Chapter 5, where predictions for core transport in the FAST tokamak have been worked out using an appropriate mixture of first-principle models and semi-empirical, experiment driven considerations. In particular such modelling has included the effects of rotation on transport, which is itself not commonly done for future device predictions, but in particular has included through semi-empirical considerations the effects of rotation and flat q profile on ion stiffness, which is a very new result not yet

properly dealt with in available first-principle models. This way of carrying out the simulations for the various scenarios, from H-modes to Advanced Tokamak with ITB formation, is meant to achieve more realistic predictions than using purely first principle models which still lack full validation and, even worse, have been found in some situations to be unable to reproduce the experimental findings. By maintaining a close insight into the experimentally observed behaviour of JET, C-Mod and other devices, it is also possible to discriminate in which situations the existing first principle models can be trusted for predicting the FAST scenarios, and in which it is better to rely on empirically driven models. As a future development of this FAST simulation work, a similar approach could be applied to predictions of ITER scenarios, with the advantage that the JET results have triggered further theory work on the issue of stiffness and rotation, and recently some first principle models have become available, which feature the experimentally observed ion stiffness mitigation in presence of rotation and flat q profile, namely a revised version of the Weiland model and the TGLF model. These should now be used for ITER predictions in place of the CGM model with adjustable stiffness that has been used in Chapter 5 for FAST. We have to be aware however that the calculation of the intrinsic rotation profile in ITER may be more cumbersome than in FAST, due to absence of a reliable extrapolation from present experimental databases to the ITER range of parameters (whilst FAST is rather near to the C-MOD device), with further complications arising from the presence of non-axisymmetric fields such as generated by ELM mitigation coils, Test Blanket Modules, high level of B_T ripple.

Finally, since the CGM model has been used for FAST predictions using as threshold the analytical expression derived by F.Romanelli et al., it was mandatory to check its validity also in the region of operation of FAST, which is a high B_T machine, therefore operating in a rather peculiar domain of parameters with respect to standard B_T tokamaks for which the formula may have been tested against numerical simulations. An effort was then made to get acquainted with the GKW gyro-kinetic code in order to run linear simulations using the FAST scenario parameters, scanning the R/L_{Ti} value to achieve the estimate of the linear threshold by extrapolation to the condition of zero growth rate. This work is described in Chapter 6. Such GKW result was then compared with the formula prediction using the same parameters. The agreement was found rather good, thus supporting the results of the simulations based on the CGM model and described in Chapter 5.

If a main message has to be extracted from this thesis as a suggestion for future work, this is the need of accounting for the effect of rotation on ion heat transport, both in terms of threshold and stiffness, when interpreting or predicting tokamak scenario performance. It is clear that on one hand the recent JET results have to be confirmed on other machines, and possibly an experiment driven empirical expression for the ion stiffness dependence on rotational and magnetic shear could be derived, on the other hand such results have to find a theory based explanation, which is still an open issue, since there is not yet agreement between non-linear gyro-kinetic simulations and data.

However it is also clear that rotation effects can no longer be neglected when dealing with ion heat transport.

Acknowledgments

I would like to thank my tutor Prof. Roberto Pozzoli and my co-tutor Dr. Paola Mantica, who have closely followed my work during these three years. My gratitude to Dr. Paola Mantica is for having introduced me into the complex world of the physics of plasma transport, giving directions to my work and helping me to find out the essential questions at the basis of my thesis, as well as for having given me the possibility to interact with different teams in an international context. I am grateful to Prof. Roberto Pozzoli for many advices and suggestions, for his availability for discussing plasma physics questions and for having helped me with the organization of my work.

This work was made possible thanks to the Institute of Plasma Physics (IFP) of CNR in Milan, in which the thesis work was carried out. IFP-CNR, which is an Euratom research unit, has given me the opportunity of interacting with Italian and International researchers, and has provided spaces and means to work and access to Euratom financial resources. Thanks to the IFP scientific team for the support in the fusion plasma physics field and for the help in sharing and facing the working everyday life.

I would also like to thank the Italian Embassy in London that has supported with a student internship my first 6 months of work at the EFDA-JET Culham Research Centre, Oxfordshire (UK).

My thanks to Dr. Tuomas Tala and Dr. Volker Naulin for having followed me during my experience at the EFDA-JET laboratory, transmitting me their experience and knowledge, and to the JET researchers and collaborators for the scientific and practical support, in particular Dr. Gerard Corrigan for his invaluable help in dealing with numerical issues of the JET transport codes.

Thanks to the FAST team of the Frascati ENEA Energy Research Centre for having given to me the possibility to collaborate to the predictive modelling for the new proposed machine FAST, a very instructive work for me.

Thanks to Prof. Arthur Peeters for having introduced me into the field of the gyro-kinetics simulations, teaching me the physical basis and making me use his gyro-kinetic code GKW. Thanks to his team for having welcomed me during the month spent at Warwick University, in Coventry (UK) and for having helped me to overcome the difficulties met with the code.

Thanks to Dr. Gerardo Giruzzi for being the referee of the thesis and for his pertinent remarks and corrections.

Finally, thanks to my family for being always close to me, representing for me a solid reference point, and to all the people that have accompanied my path during these three intense years, in particular the Master student Pierluigi Migliano with whom I have shared the effort of using GKW in Milano.

List of Figures

List of Tables

Bibliography

[1] J. D. Lawson, Proceedings of the Physical Society B, Volume 70 (1957), p. 6

[2] http://www.efda.org/eu_fusion_programme/r-plasma_physics.htm

[3] M. D. Kruskal and M. Schwarzchild, *Some instabilities of a completely ionized plasma,* Proc. R. Soc. London, Ser. A, **223**, 348 (1954).

[4] S. I. Braginskii, Transport Process in a Plasma, Review of Plasma Physics, M. A. Leontovich (ed.), Consultants Bureau, Vol. 1, pp. 205-311 (1965)

[5] S. Chapman, T. J. Cowling, *The mathematical theory of non-uniform Gases Cambridge* Univ. Press (1952)

[6] M. N. Rosenbluth, R. D. Hazeltine, F. L. Hinton, Phys. Fluids **15** 116 (1972)

[7] J. Wesson, *Tokamaks*, Clarendon Press, Oxford, (1987)

[8] A. A. Ware, Phys. Review Letters **25** 12 (1970)

[9] R. J. Bickerton, J. W. Connor, J. B. Taylor, Nature Phys. Sci. **229** 110 (1971)

[10] L. R Grisham et al., Phys. Review Letters **67** 66 (1991)

[11] F. Wagner et al., Phys. Review Letters **49** 1408 (1982)

[12] O. Gruber et al., Phys. Review Letters **83** 1787 (1999)

[13] T. Luce et al., Nuclear Fusion **41** 1585 (2001)

[14] C. Gormenzano et al., Plasma Phys. and Control. Fusion **46** B435 (2004)

[15] J. W. Connor et al., Nuclear Fusion **44** R1 (2004)

[16] V. V. Parail et al., Plasma Phys. and Control. Fusion **44** A63 (2002)

[17] P. H. Diamond et al., Plasma Phys. and Control. Fusion **47** R35 (2005)

[18] N. J. Lopes Cardozo et al., Plasma Phys. and Control. Fusion **37** 799 (1995)

[19] X. Garbet et al., Plasma Phys. and Control. Fusion **43** A251 (2001)

[20] X. Garbet et al., Plasma Phys. and Control. Fusion **46** B557 (2004)

[21] N. Mattor et al., Phys. Fluids **31** 1180 (1988)

[22] F. Romanelli et al., Phys. Fluids B **1** 1018 (1989)

[23] J. W. Connor and H. R. Wilson, Plasma Phys. Controlled Fusion **36** 719 (1994)

[24] M. Kotschenreuther et al., Phys. Plasmas **2** 2381 (1995)

[25] E. J. Doyle et al 2000 Fusion Energy 2000: Proc. 18th Int. Conf. (Sorrento, 2000) (Vienna: IAEA) CD-ROM file EX6/2 and http://www.iaea.org/programmes/ripc/physics/fec2000/html/fec2000.htm

[26] F. Ryter et al., Plasma Phys. and Control. Fusion **48** B453 (2006)

[27] P. Mantica and F. Ryter, Comptes Rendus Physique **7** 634 (2006)

[28] P. Mantica et al., Phys. Review Letters **102** 175002 (2009)

[29] P. Mantica et al., Phys. Review Letters **107** 135004 (2011)

[30] P. Mantica et al., Plasma Phys. and Control. Fusion **53** 124033 (2011)

[31] M. Greenwald et al., Plasma Phys. and Control. Fusion **44** R27 (2002)

[32] J. Stober et al., Nuclear Fusion **41** 1535 (2001)

[33] C. Angioni et al., Plasma Phys. and Control. Fusion **51** 124017 (2009)

[34] D. Suckewer et al., Nuclear Fusion **21** 1301 (1981)

[35] J. E. Rice et al., Nuclear Fusion **47** 1618 (2007)

[36] P.C. de Vries et al., Plasma Phys. and Control. Fusion **48** 1693 (2006)

[37] T. Tala et al., Nuclear Fusion **47** 2012 (2007)

[38] T. Tala et al., Plasma Phys. and Control. Fusion **49** B291 (2007)

[39] A. G. Peeters et al., Nuclear Fusion **51** 094027 (2011)

[40] T.Tala et al, Phys. Review Letters **102** 075001 (2009)

[41] P. Mantica et al., Phys. Plasmas **17** 092505 (2010)

[42] J. Weiland, *Collective Modes in Inhomogeneous Plasmas - Kinetic and Advanced Fluid Theory*, Institute of Physics Publishing (1999)

[43] H. Nordman and J. Weiland, Nuclear Fusion **29** 251 (1989)

[44] H. Nordman, J. Weiland and A. Jarmen, Nuclear Fusion **6** 983 (1990)

[45] R. D. Hazeltine and J. D. Meiss, *Plasma Confinement*, Addison-Wesley Publishing Company (2003)

[46] G. Tardini, Validation of theory based transport models in tokamak plasmas, PhD thesis (2003)

[47] S. C. Guo and F. Romanelli, Phys. Fluids B **5** 520 (1992)

[48] R. E. Waltz et al., Phys. Plasmas **4** 2482 (1997)

[49] J. E. Kinsey, G. M. Staebler and R. E. Waltz, Phys. Plasmas **12** 052503 (2005)

[50] R. E. Waltz, G. D. Kerbel and J. Milovich, Phys. Plasmas **1** 2229 (1994)

[51] M. Erba et al., Plasma Phys. Control. Fusion **39** 261 (1997)

[52] F. Imbeaux, F. Ryter and X. Garbet, Plasma Phys. Control. Fusion **43** 1503 (2001)

[53] X. Garbet et al., Plasma Phys. Control. Fusion **46** 1351 (2004)

[54] P. Mantica et al., Fusion Science and Technology **53** 1152 (2008)

[55] F. Ryter et al., Plasma Phys. Control. Fusion **48** B453 (2006)

[56] F. Ryter F et al., Phys. Rev. Lett. **95** 085001 (2005)

[57] F. Ryter et al., Nuclear Fusion **51** 113016 (2011)

[58] H. Biglari, P. H. Diamond and P. W. Terry, Phys. Fluids **2** 1 (1990)

[59] R. E. Waltz et al., Phys. Plasmas **2** 2408 (1995)

[60] R. E. Waltz, R. L. Dewar, X. Garbet, Phys. Plasmas **5** 1784 (1998)

[61] K. Itoh et al., *Transport & Structural Formation in Plasmas*, IoP (1999)

[62] D. Palumbo et al., Fusion Science and Technology **53** 861 (2008)

[63] B. Tubbing et al., Proc. 22th EPS Conf. on Plasma Phys. Controlled Fusion (Montpellier, France, 1995) vol 19C p IV-001 (1995)

[64] P. C. De Vries et al., Nuclear Fusion **48** 035007 (2008)

[65] Saibene G, et al., Proceedings of the 22nd Int. Conf. on Fusion Energy 2008 (Geneva, Switzerland, 2008) (Vienna: IAEA) CD-ROM file EX/2-1 http://www-naweb.iaea.org/napc/physics/FEC/FEC2008/papers/ex_2-1.pdf (2008)

[66] P. C. de Vries et al., Plasma Phys. Controlled Fusion **52** 065004 (2010)

[67] I. Barlow et al., Fus. Eng. and Design **58-59** 189 (2001)

[68] K. C. Shaing KC, Phys. of Plasmas **10** 1443 (2003)

[69] Y. Liang et al., Phys. Rev. Lett. **98** 265004 (2007)

[70] Y. Sun et al. Plasma Phys. Controlled Fusion **52** 105007 (2010)

[71] Y. Liang et al., Nuclear Fusion **50** 025013 (2010)

[72] L. G. Eriksson, T. Hellsten and U. Willen, Nuclear Fusion **33** 1037 (1993)

[73] C. D. Challis et al., Nuclear Fusion **29** 563 (1989)

[74] J. A. Heikkinen and S. K. Sipilä, Phys. Plasmas **2** 3724 (1995)

[75] A. Salmi et al., Plasma Phys. Control. Fusion **53** 085005 (2011)

[76] A. Salmi et al., Contrib. Plasma Phys. **48** 77 (2008)

[77] P. C. de Vries et al., Nuclear Fusion **48** 065006 (2008)

[78] Y. Lin et al., Phys. Rev. Lett. **101** 235002 (2008)

[79] L. G. Eriksson et al., Plasma Phys. Control. Fusion **51** 044008 (2009)

[80] Y. Lin et al., " ICRF mode conversion flow drive in (^{3}He)D plasmas on JET", accepted by Plasma Phys. Control. Fusion

[81] CenacchiG and Taroni A *JETTO: A free boundary plasma transport code (basic version) Rapporto ENEA RT/TIB (5)* (1988)

[82] S. P. Hirshman et al., PPPL-1326 Report (1977)

[83] L. Lao et al., Nuclear Fusion **25** 1611 (1985)

[84] A. R. Esterkin and A. D. Piliya, Nuclear Fusion **36** 1501 (1996)

[85] ITER Physics Basis Document, Nuclear Fusion **39** 2175 (1999).

[86] E. Joffrin et al., Proc. 23rd IAEA Fusion Energy Conference on Plasma Physics, Dajeon, Republic of Korea (2010)

[87] W. A. Houlberg et al., Phys. Plasmas **4** 3231 (1997)

[88] M. Shimada et al., Progress in the ITER Physics Basis Chapter 1: Overview and summary, Nuclear Fusion **44** S1 (2007)

[89] D. V. Bartlett. et al., Fusion Science and Technology **57** 27 (2010)

[90] E. Kinsey et al., Nuclear Fusion **43** 1845 (2003)

[91] E.J. Doyle et al., Progress in the ITER Physics Basis Chapter 2: Plasma Confinement and transport, Nuclear Fusion **44** S18 (2007)

[92] T. Tala et al., Plasma Phys. Control. Fusion **43** 507 (2001)

[93] A. Cardinali et al., Nuclear Fusion **49** 095020 (2009)

[94] A. Pizzuto et al., Nuclear Fusion **50** 095005 (2010)

[95] G. Calabrò et al., Nuclear Fusion **49** 055002 (2009)

[96] F. Alladio and F. Crisanti, Nuclear Fusion **26** 1143 (1986)

[97] G. Calabrò et al., Proc. 37th EPS Conf. on Controlled Fusion and Plasma Physics (Dublin, Ireland)P4.157 http://ocs.ciemat.es/EPS2010PAP/pdf/P4.157.pdf (2010)

[98] G. Maddaluno et al., Nuclear Fusion **49** 095011 (2009)

[99] M. Brambilla, Plasma Phys. Contr. Fusion **41** 1 (1999)

[100] M. Brambilla, Nucl. Fusion **34** 1121 (1994)

[101] D. Farina, "GRAY: a quasi-optical ray tracing code for electron cyclotron absorption and current drive in tokamaks", IFP-CNR Internal Report FP 05/1 and http://www.ifp.cnr.it/ publications/2005/FP05-01.pdf

[102] A. R. Esterkin and A. D. Piliya, Nuclear Fusion **36** 1501 (1996)

[103] M. Schneider et al., Plasma Phys. Control. Fusion **47** 2087 (2005)

[104] L. Frassinetti *et al.*, Proc. 37th EPS Conf. on Controlled Fusion and Plasma Physics (Dublin, Ireland)P1.1031 http://ocs.ciemat.es/EPS2010PAP/pdf/P1.1031.pdf (2010)

[105] M. N. A. Beurskens et al., Proc.52th APS Division of Plasma Phys. Conf. (Chicago, USA, 2010) http://meetings.aps.org/link/BAPS.2010.DPP.GI2.5 (2010)

[106] A. G. G. Peeters et al., Proc. 23rd Int. Conf. on Fusion Energy (Daejeon, China, 2010)(Vienna: IAEA) CD-ROMfile [OV/5-4]and http://www-naweb.iaea.org/napc/physics/FEC/FEC2010/html/index.htm (2010)

[107] T. Tala et al., Proc. 23rd Int. Conf. on Fusion Energy (Daejeon, China, 2010)(Vienna: IAEA) CD-ROMfile [EXC/3-1]and http://www-naweb.iaea.org/napc/physics/FEC/FEC2010/html/index.htm (2010)

[108] W. M. Solomon et al., Nuclear Fusion **49** 085005 (2009)

[109] A. G. Peeters et al., Phys. Rev. Lett. **98** 265003 (2007)

[110] G. Tardini et al., Nuclear Fusion **49** 085010 (2009)

[111] P. DeVries et al., Nuclear Fusion **49** 075007 (2009)

[112] P. A. Politzer et al., Nuclear Fusion **48** 075001 (2008)

[113] M. F. F. Nave et al., Proc. 37th EPS Conf. on Controlled Fusion and Plasma Physics (Dublin, Ireland) O4.122 http://ocs.ciemat.es/EPS2010PAP/pdf/O4.122.pdf (2010)

[114] M. Baruzzo et al., Proc. 37th EPS Conf. on Controlled Fusion and Plasma Physics (Dublin, Ireland) P5.142 http://ocs.ciemat.es/EPS2010PAP/pdf/P5.142.pdf (2010)

[115] P. C. De Vries et al., Nuclear Fusion **49** 075007 (2009)

[116] P. A. Politzer et al., Nuclear Fusion **48** 075001 (2008)

[117] F. Turco et al., Plasma Phys. Control. Fusion **51** 065021 (2009)

[118] J. Rice et al., Nuclear Fusion **43** 781 (2003)

[119] M. F. F. Nave et al., Phys. Rev. Lett. **105** 105005 (2010)

[120] Y. Lin et al., Proc. 37th EPS Conf. on Controlled Fusion and Plasma Physics (Dublin, Ireland) P5.164 http://ocs.ciemat.es/EPS2010PAP/pdf/P5.164.pdf (2010)

[121] A. Cardinali et al., Proc. 23rd Int. Conf. on Fusion Energy (Daejeon, China, 2010) (Vienna: IAEA) CD-ROM file [THW/P7-04] and http://www-naweb.iaea.org/napc/physics/FEC/FEC2010/html/index.htm (2010)

[122] A. G. Peeters et al., Computer Phys. Communications **180** 2650 (2009)

[123] A. G. Peeters et al., Phys. Plasmas **11** 3748 (2004)

[124] S. Ichimaru, Statistical Plasma Phys. vol I: Basic Principles (Redwood City, CA: Addison-Wesley) (1992)

[125] S. Hamada, Nucl. Fusion **2** 23 (1962)

[126] J. W. Connor et al., Phys. Rev. Lett. **40** 396 (1978)

[127] A. J. Brizard et al., Rev. Mod. Phys. **79** 421 (2007)

[128] R. G. Littlejohn, J. Math. Phys. **20** 2445 (1979)

[129] R. G. Littlejohn, J. Plasma Phys. **29** 111 (1983)

[130] D. H. E. Dubin et al., Phys. Fluids **26** 3524 (1983)

[131] A. J. Brizard, J. Plasma Phys. **41** 541 (1989)

[132] J. R. Cary, Phys. Rep. **79** 129 (1981)

[133] J. R. Cary et al., Ann. Phys. **151** 1 (1983)

[134] A. G. Peeters et al., Phys. Plasmas **16** 042310 (2009)

[135] H. Sugama, Phys. Plasmas **7** 466 (2000)

[136] B. Scott et al., Phys. Plasmas **17** 112302 (2010)

[137] A. J. Brizard, Phys. Plasmas **2** 459 (1995)

[138] R. G. Littlejohn, Phys. Fluids **24** 1730 (1981)

[139] F. J. Casson, Turbulent transport in rotating tokamak plasmas, PhD thesis (2011)

[140] C. F. F. Karney, Comput. Phys. Rep. **4** 183 (1986)

[141] A. J. Brizard and T. S. Hahm, Reviews of Modern Physics **79** 421 (2007)